An Experimental Study of Flow and Heat Transfer in Offset Strip and Louvered-Fin Heat Exchangers

N. C. DeJong and A. M. Jacobi

ACRC TR-91 December 1995

For additional information:

Air Conditioning and Refrigeration Center
University of Illinois
Mechanical & Industrial Engineering Dept.
1206 West Green Street
Urbana, IL 61801

(217) 333-3115

Prepared as part of ACRC Project 38
An Experimental and Numerical Study of Flow and Heat Transfer in Louvered-Fin Heat Exchangers
S. Balachandar and A. M. Jacobi, Principal Investigators

The Air Conditioning and Refrigeration Center was founded in 1988 with a grant from the estate of Richard W. Kritzer, the founder of Peerless of America Inc. A State of Illinois Technology Challenge Grant helped build the laboratory facilities. The ACRC receives continuing support from the Richard W. Kritzer Endowment and the National Science Foundation. The following organizations have also become sponsors of the Center.

Amana Refrigeration, Inc.
Brazeway, Inc.
Carrier Corporation
Caterpillar, Inc.
Dayton Thermal Products
Delphi Harrison Thermal Systems
Eaton Corporation
Electric Power Research Institute
Ford Motor Company
Frigidaire Company
General Electric Company
Lennox International, Inc.
Modine Manufacturing Co.
Peerless of America, Inc.
U. S. Army CERL
U. S. Environmental Protection Agency
Whirlpool Corporation

For additional information:

Air Conditioning & Refrigeration Center
Mechanical & Industrial Engineering Dept.
University of Illinois
1206 West Green Street
Urbana IL 61801

217 333 3115

ABSTRACT

The efficiency of heat exchangers is important in the HVAC/R industry. Driven by high energy standards and increasing competition, manufacturers are seeking to decrease air-side resistance in heat exchangers by increasing the heat transfer coefficient. Offset strip and louvered fins increase the heat transfer coefficient through two methods -- boundary layer restarting and the initiation of self-sustained oscillations. The purpose of this thesis is to develop a better understanding of flow and heat transfer in offset strip and louvered fins so that design guidelines may be developed. Five geometries are analyzed in this study -- two offset strip and three louvered with a 25° angle of incidence -- over a Reynolds number range of 100 to 12000. Heat transfer is inferred from mass transfer data acquired using the naphthalene sublimation method, and pressure drop across each array is determined using conventional methods. Flow visualization studies are performed to develop a more complete understanding of the actual flow mechanisms. The results show that vortex shedding in the periodic regime increases heat transfer significantly. Measurements of local mass transfer along a fin show that local heat transfer behavior on a fin is different for offset strip and louvered fins, and these results are used to develop design guidelines Because of the flow structures at work, short louvered fins may be especially advantageous. Studies of overall behavior show that at a given Reynolds number, louvered fins require less area for a given heat duty than do offset strip fins. However, pumping power is significantly higher for louvered fins. Therefore, if heat exchanger efficiency is more important than heat exchanger size, offset strip fins may be just as desirable if not more desirable than louvered fins for certain exchanger geometries and operating conditions.

TABLE OF CONTENTS

LIST OF FIGURES

NOMENCLATURE

Roman Symbols:

A	total heat transfer surface area
A_c	minimum free flow area of heat exchanger core
A_f	naphthalene surface area
A_r	rth coefficient of the discrete fourier transform
C	discharge coefficient
C_A	concentration of A
C_B	concentration of B
D	pipe diameter
D_{AB}	mass diffusion coefficient of A in B
D_{na}	mass diffusion coefficient of naphthalene in air
d_h	hydraulic diameter
f	friction factor or function
F	focal length
h	local heat or mass transfer coefficient
$\bar{h}$	average heat or mass transfer coefficient
j	modified Colburn j factor (see equation 3.4)
L	plate length
L_{core}	length of heat exchanger core
m	mass
$\dot{m}$	mass flow rate
M	molecular weight
n	vortex shedding frequency or exponent
N	number of data points

Nu	local Nusselt number
$\overline{Nu}$	average Nusselt number
p	fin pitch
P	pressure
P_{corr}	barometric pressure corrected for gravity and temperature
P_f	fin pitch
P_{gcf}	gravity correction factor for barometric pressure
P_l	louver pitch
P_n	naphthalene vapor pressure
PP	pumping power
P_{tcf}	temperature correction factor for barometric pressure
Pr	Prandtl number
q''	heat flux
R_g	air-side thermal resistance
R_u	universal gas constant
Re	Reynolds number, based on hydraulic diameter unless otherwise noted
S_T	standard deviation of temperature readings
Sc	Schmidt number
SCF	stem correction factor (see Appendix C)
Sh	local Sherwood number based on hydraulic diameter
$\overline{Sh}$	average Sherwood number based on hydraulic diameter
Sr	Strouhal number (see equation 3.10)
ST	thermometer stem temperature
t	time or plate thickness
T	temperature
u	x component of velocity
U	magnitude of air or water velocity

v	y component of velocity
W	uncertainty
x	distance
x^*	dimensionless distance (horizontal distance along test section/test section width--see section 2.1)
X_k	kth sample of the discrete fourier transform data

Greek Symbols:

α	thermal diffusivity
β	ratio of orifice plate bore diameter to pipe diameter
δ_{sb}	local sublimation depth
Δ	a change in some quantity
ε	expansion factor or effectiveness
μ	dynamic viscosity
η_f	fin efficiency
η_o	overall surface efficiency $\left(\eta_o = 1 - \frac{A_{fin}}{A}\left(1 - \eta_f\right)\right)$
θ	angle of incidence of fins to air flow
ρ	density
ν	kinematic viscosity
v_b	transverse velocity due to viscous effects (see Appendix A)

Subscripts:

A	species A
a	property of air
B	species B
b	bulk (mixing-cup)
c	property evaluated at the core (minimum free-flow area) of the heat exchanger

fin	related to the fins, not the tubes
i	photodetector coordinate (see Fig. 2.7) or inlet
int	obtained by integration of local data
L	plate length
lp	louver pitch
m	mass transfer
mean	averaged over a cross section
n, s	solid naphthalene
n, v	naphthalene vapor
o	object coordinate (see Fig. 2.7)
opt	optimum
p	fin pitch
ref	reference quantity
s	light source coordinate (see Fig. 2.7)
t	fin thickness
w	property evaluated at the wall
x	property evaluated at position x
∞	property evaluated in the freestream

CHAPTER 1 - INTRODUCTION

1.1 Background

The efficient use of material and energy has a high engineering priority because our natural resources are limited and because pollution due to fossil fuels can have alarming effects on the environment. The heating, ventilating, air-conditioning, and refrigeration (HVAC/R) industry has been directly affected by this growing environmental awareness, and the heat exchanger is an important component in that industry. Driven by performance demands and foreign competition, component and system manufacturers now require small, light weight, low cost, high efficiency heat exchangers.

In many HVAC/R applications, the performance of heat exchangers is restricted by the air-side thermal resistance. Admiraal and Bullard [1] found that for residential refrigerator heat exchangers the air-side resistance makes up 95% of the condenser resistance and 76% of the evaporator resistance in the two-phase region. The air-side resistance can be represented by

$$R_a = \frac{1}{\bar{h}\eta_o A} \qquad [1.1]$$

This equation shows that the air-side resistance can be decreased by increasing the area, surface efficiency, or heat transfer coefficient. Since space and material cost are both of high priority, most manufacturers are unwilling to increase the fin area. In compact heat exchangers with small channels, the heat transfer coefficient is small. One of the most promising ways to decrease the air-side resistance is to increase the heat transfer coefficient.

One of the most widely exploited air-side advancements is the louvered-fin surface. A typical surface is shown in Figure 1. The interrupted fin surface causes the boundary layer to restart on each new louver. Since the average boundary-layer thickness is smaller for short plates than for long plates, the average heat transfer coefficient is much higher for an interrupted surface than for a continuous surface. Figure 2 shows the theoretical local heat transfer

coefficients for air blowing at 1.0 m/s (3.3 ft/s) over a 20 cm (7.9 in) flat plate compared to eight 2.5 cm (0.98 in) plates.

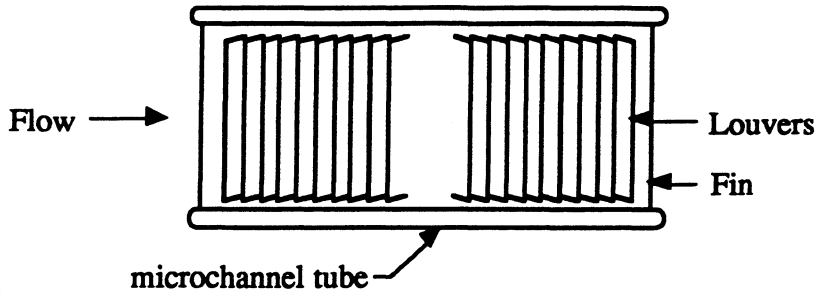

Fig. 1.1 - Typical louvered-fin and microchannel tube geometry

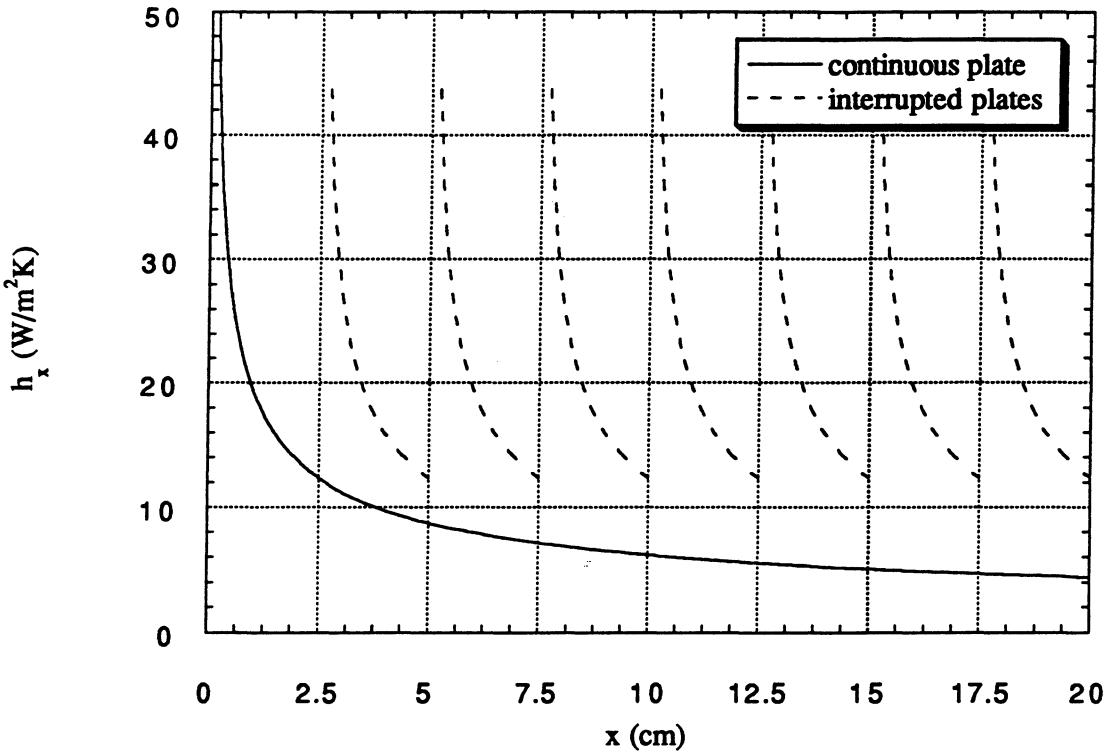

Fig. 1.2 - Local heat transfer coefficient versus distance along the fin for one continuous plate and eight interrupted plates for theoretical laminar flow

Recent work suggests that louvers enhance heat transfer through another mechanism as well -- namely, the initiation of self-sustained oscillations. Above a certain critical Reynolds number, the louvers begin to shed vortices. These vortices form self-sustained periodic flow oscillations

that can increase heat transfer significantly. This project is focused on developing a better understanding of these flow and heat transfer enhancement mechanisms in offset strip (parallel louvered) fins and louvered fins so that design guidelines may be formulated.

1.2 Literature Review

An abundance of work has been performed on offset strip and louvered-fin heat exchangers. The literature review presented below is organized into two sections. The first deals with offset strip fins--fins with a zero degree angle of attack to the flow -- while the second deals with louvered fins--fins with a non-zero degree angle of attack to the flow. The first section will cover research dealing with collinear plates, general correlations, and detailed descriptions of the flow and heat transfer characteristics.

1.2.1 Offset Strip Fins

One of the first studies of offset strip fins was performed in 1942 by Norris and Spofford [2], who, by testing three types of offset fins, showed that offset strip fin performance data can be correlated with a Reynolds number based on strip perimeter. In 1978, Cur and Sparrow [3] performed some early work dealing with the optimization of the offset strip geometry. Using the naphthalene sublimation method and a Baratron capacitance-type pressure meter, they analyzed the effect of fin thickness and interplate spacing for a pair of collinear interrupted plates aligned with the flow. They concluded that an increase in Nusselt number accompanying an increase in plate thickness is more than offset by the increase in the pressure drop. They also concluded that the conventional plate spacing, in which the gap between plates is equal to the plate length, is not always optimal.

More exhaustive studies of the flow and heat transfer behavior in interrupted plate geometries were performed by Amon and Mikic in 1989 [4] and Amon *et al.* in 1991 [5]. Amon and Mikic used the spectral element method to numerically model flow through grooved channels and flow through communicating channels--a channel with one column of collinear plates. They

discovered that above a critical Reynolds number, self-sustained laminar oscillations occur in the flow at a frequency near the least stable Tollmien-Schlichting frequency. As a result of these oscillations and the restarting of the boundary layer with each successive plate, heat transfer in this interrupted plate geometry can be up to 300% higher than in a flat plate geometry with the same pumping power. Pumping power is proportional to the square of the Reynolds number for a given Nusselt number in this geometry. At very low Reynolds numbers, they found two symmetrical standing eddies to be present behind the plates. At slightly higher velocities, these eddies break into an oscillating vortex sheet. At higher Reynolds numbers yet, they found that vortices are ejected alternately above and below the plates. These ordered oscillations result in less viscous dissipation than a chaotic turbulent flow. In addition to using the spectral-element Fourier method, Amon and coworkers visualized the flow in a communicating channel geometry using real-time holographic interferometry. They discovered that in certain Reynolds number ranges, two unstable Tollmien-Schlichting modes are present in the flow rather than just the least stable one. They concluded that the self-sustained oscillations and ejection of vortices increase heat transfer by increasing mixing and affecting the flow at the impinging edge of the plate. The vortices delay the formation of the thermal boundary layer, thus decreasing its overall thickness.

Many correlations for the overall heat transfer and pressure drop in offset-strip fins have been developed. In 1968, London and Shah [6] developed graphs of j and f for eight offset strip geometries. They concluded that an optimum heat exchanger will have small offset spacing (fin length/d_h) and fin thickness and a large aspect ratio (large number of fins per inch). In 1975, Wieting [7] developed empirical correlations for heat transfer and friction factors based on data from London and Shah and others for 22 offset fin configurations. From these correlations, it is apparent that fin thickness has little effect in the laminar regime while the ratio of flow passage width to height has little effect in the turbulent regime. In 1989, Sekulik [8] provided a summary of research on in-line parallel plate arrays. In 1990, Manglik and Bergles [9] published an exhaustive annotated bibliography of research on offset strip fins.

E.M. Sparrow has worked extensively on the in-line and staggered plate geometries. Sparrow, Baliga, and Patankar [10] used finite difference techniques to solve the mass, momentum, and energy conservation equations. Since they used a steady-state code, their results are only valid in the steady laminar flow regime. In addition, they used an idealized geometry by neglecting fin thickness in their model. From these calculations, they concluded that for a given pumping power and surface area, a staggered arrangement gives higher heat transfer than an in-line arrangement but also requires a higher mass flow. Pressure drop increases with increasing Reynolds number and decreasing plate length. In the fully developed regime they found the velocity and temperature profiles to fluctuate periodically with periodic changes in geometry. Sparrow and Liu [11] came to many of the same conclusions by evaluating the effectiveness of in-line, staggered, and continuous plate heat exchangers. They defined the effectiveness as $\varepsilon = (T_{bx} - T_i)/(T_w - T_i)$ where T_{bx} is the bulk temperature at position x, T_i is the bulk temperature at the inlet, and T_w is the plate temperature. Sparrow and Hajiloo [12] used the naphthalene sublimation method to analyze staggered-plate geometries for Reynolds numbers based on hydraulic diameter from 1000 to 9000. They used only one naphthalene coated plate for each run. They found the thermally developing region to be only one row deep in the "periodic fully developed regime," which they defined as a fully developed regime with streamwise velocity variations due to periodic changes in geometry. Like Wieting, they found that plate thickness has little effect for Re<1200. The Nusselt number increases with Reynolds number but increases faster for thicker fins. For the thickest plates, the friction factor f is independent of Reynolds number. For thin plates, however, f decreases smoothly with an increase in Re.

Patankar and Prakash [13] numerically analyzed the effect of plate thickness on laminar flow and heat transfer in a staggered plate arrangement. They found the flow to be fully developed in most cases after five rows and at most ten. At low Reynolds numbers, flow impinges on the leading edge and forms a recirculation zone behind the trailing edge. At higher Reynolds numbers, the recirculating flow fills the entire streamwise gap between plates. If the Reynolds

number is increased even more, the recirculation zone is shifted downstream. In general, an increase in plate thickness is undesirable. It leads to higher pressure drop but little improvement in heat transfer due to the effects of flow separation. It must be noted that they assumed laminar, steady-state flow. Although this assumption is valid at low Reynolds numbers, the upper end of the Reynolds number range that they studied was well within the periodic vortex shedding regime. Vortex shedding increases both heat transfer and pressure drop; their simulation was not able to take these effects into account.

In 1982, Mochizuki and Yagi [14] used dye and hydrogen bubbles to visualize flow through offset strip fins in a water tunnel. In addition, they used a hot-wire anemometer to measure the vortex shedding frequency. Vortex shedding excites acoustic modes, resulting in noise with a frequency similar to the natural vortex shedding frequency. The authors performed their tests for a variety of conditions ranging from a single plate to twenty rows, or stages. For a single plate, at Re_t=250, the Strouhal number makes a stepwise decrease and then remains constant for further increases in Re_t. At this point, vortex shedding moves from the trailing edge of the plate to the leading edge. They reported that when more rows are added, the shedding frequency before the Strouhal number transition is lower than for a single plate. If two rows are present, two Strouhal numbers are also present because the two rows result in different wakes. With three to eight rows, one Strouhal number is present at low Reynolds numbers, but multiple Strouhal numbers are present at higher Reynolds numbers since vortices are shed from every row. For nine to twenty rows, they found the Strouhal number to be constant at 0.13. They observed that as the Reynolds number is increased, the onset of vortex shedding moves upstream in the array. Three regimes were present in the flow--steady laminar, oscillating, and turbulent flow. When the Reynolds number is small, a small increase in the Reynolds number can cause vortex shedding to begin much farther upstream, but when the Reynolds number is large, only minor changes occur. In 1988, Mochizuki, Yagi, and Yang [15] also analyzed turbulence intensity for this geometry. They found that turbulence intensity behavior follows the flow regime behavior. They concluded

that the offset strip geometry has a higher turbulence intensity than either a plate fin or an in-line interrupted fin geometry and thus would have higher heat transfer.

In 1983, Yang [16] replotted and analyzed the data of Kays and London [17] for louvered-, strip-, perforated-, wavy-, and pin-fin surfaces. From his analysis he concluded that three flow regimes exist--laminar, "second laminar", and turbulent. Heat transfer is enhanced significantly in the second laminar regime due to self-sustained oscillations. He developed theoretical correlations to predict the Reynolds number at which these flow regimes begin.

Mullisen and Loehrke [18] studied both in-line and staggered interrupted-plate arrays for a range of $100<Re<10000$. They used the Schlieren technique to visualize the flow and a transient heating technique to analyze heat transfer. In contrast to Yang, in the in-line arrangement they viewed three regimes which they named steady, general unsteady, and periodic unsteady. In the general unsteady regime, the wake has a wavy structure downstream of the fins. The amplitude of the unsteadiness grows as the flow continues downstream, sometimes forming flow structures that appear turbulent and fill the entire passageway. The periodic unsteady regime is characterized by vortex shedding from the trailing edge of the plates. In contrast to Mochizuki and Yagi, they concluded that for their geometry the flow regime does not depend on streamwise location. According to their studies, the wind tunnel test section geometry is important in establishing the resonant frequency, while the plate dimensions and flow velocity are important in establishing the shedding frequency. When these two frequencies are similar, noise and periodic flow result. Mullisen and Loehrke also plotted j and f for various plate thicknesses. They saw an increase in j and f at the transition to unsteady flow. They theorized that this augmentation was due to the increase in mixing and turbulence which disrupted the boundary layers of downstream plates. They found flow through the staggered arrangement to be more stable than through the in-line arrangement; furthermore, this flow resulted in higher values of j/f. Flow transitions occur at higher Reynolds numbers when streamwise spacing and plate thickness are decreased.

Joshi and Webb [19] used a combination of analytical and experimental techniques to analyze offset strip fins. They developed equations for the Nusselt number and friction factor by performing energy and momentum balances on individual cells. They used a numerical approach to find Nusselt numbers and friction factors in the laminar regime and a semi-empirical approach in the turbulent regime. They compared their predicted j values to those reported in the literature and took friction factor data for eight different offset strip geometries. The authors visualized the flow for three scaled-up geometries by injecting ink into water, and they divided the flow into four different regimes. In the first regime the wake behind the upstream fin is smooth and laminar. In the second, oscillations are visible only where the flow impinges on the downstream fin; in the third, oscillations are present in the entire region between the fins, and in the fourth, vortices are shed. From their analytical and experimental work, Joshi and Webb were able to develop correlations to predict the transition from laminar to turbulent flow and to predict f and j for these two regimes.

In 1988, Kurosaki *et al.* [20] studied various configurations of parallel louvered fins. They used a bakelite plate covered with thin nichrome foil heaters and thermocouples to measure heat transfer, and they visualized isotherms using holographic interferometry. They concluded that for this geometry the wakes of upstream louvers degrade heat transfer from downstream louvers far more than do the boundary layers of adjacent louvers. For staggered fins, heat transfer from an individual fin is affected by both the number of louvers upstream and the spacing between those louvers. The authors suggested a modified arrangement in which louvers are offset such that they are out of the wakes of the louvers immediately upstream.

In a study by Xi *et al.* [21] in 1991, ink was injected into a water tunnel to visualize flow in an offset strip fin arrangement for $Re_t \leq 300$. They used a probe consisting of a hot- and cold-wire anemometer to measure velocity and temperature fluctuations. They, too, found that as the Reynolds number increases the flow proceeds from laminar flow to a flow in which the wakes exhibit either roughly sinusoidal fluid motion or the formation of a street of discrete vortices. When discrete vortices are forming in the fin wakes, the resulting additional momentum and heat

transfer causes the j curve to deviate from the flat plate solution. As the fin pitch decreases, the flow makes the transitions between these flow regimes at lower Reynolds numbers.

In 1995, Manglik and Bergles [22] reanalyzed data in the literature relating to offset strip fins. They concluded that three flow regimes exist--laminar, second laminar (transitional or vortex-shedding or oscillating flow) and turbulent. Their analysis showed that a smaller aspect ratio, thicker fins, and a shorter offset length will increase f and j. They developed correlations for j and f that apply over all three regimes and correlate the data within +/- 20%.

1.2.2 Louvered Fins

Over the past ten years, extensive research has been focused on louvered fins -- fins with a non-zero degree angle of incidence to the flow. In 1983, Davenport [23] took data for 32 different louvered-fin geometries over an air velocity range of 0.5-17 m/s. Comparing his data to those of Wieting, he found that for $Re_{lp}>2000$, the j values are similar to those of the offset strip geometry, while for $Re_{lp}<1000$ the j values for the offset strip geometry are 10% higher. At low Reynolds numbers, Davenport noted a decrease in the j factor. He attributed this falloff to boundary layer thickening which impedes flow between louvers. For the entire range he found f for the offset strip geometries to be 30-40% higher than for the louvered-fin geometries. He hypothesized that this increase was due to the fact that strip fins may be more prone to burrs, and offset strip fins usually are thicker than louvered fins.

In 1986, Lee [24] used the naphthalene sublimation method to analyze in-line plates with angles of incidence of 20°, 25°, 30°, and 35° for $350<Re<5000$. His geometry included eight rows of plates, three plates per row. Naphthalene was used only on the center column. Lee hypothesized that a non-zero-degree angle of incidence increases heat transfer by increasing turbulence and vorticity. He concluded that an optimum plate angle does exist for a given Reynolds number and geometry, and with fixed pumping power, the Nusselt number of angled fins can be nearly two times the Nusselt number of continuous plate fins.

In 1989, Aoki, Shinagawa, and Suga [25] studied local heat transfer from fins in a geometry similar to the one shown in Figure 1.3. The louvers consisted of a thin base metal, electrical insulator, and an evaporated nickel film. The film acted as both a heating film and resistance thermometer. Heat transfer coefficients were acquired by measuring the power input to the film and the louver and air temperatures. They found the heat transfer coefficients for fins downstream of the intermediate deflection louver to be slightly less than those for fins upstream. They concluded that heat transfer is influenced by factors such as fin pitch, louver pitch, and louver angle. In a later article, Suga and Aoki [26] used a finite difference code which utilized overlaid grids to numerically study this geometry. They found that the key for optimizing louvered fins is to control the thermal wakes. The optimum geometry, they found, is independent of Reynolds number for $Re_p \leq 450$. They developed the following equation which approximates the optimum geometry:

$$\left(\frac{P_f}{P_l}\right)_{opt} = 1.5 \tan\theta \qquad [1.2]$$

where P_f is the fin pitch and P_l is the louver pitch (distance between fins center-to-center in the streamwise direction). In the range $20° \leq \theta \leq 30°$, exchangers with smaller louver angles performed the best. However, since they assumed steady state flow, their results are only valid in the steady laminar flow regime. This assumption appears tenable since they studied Reynolds numbers based on fin pitch below 450. Any periodic flow effects that may exist in upper end of their range of study could not be studied using a code restricted to steady flow.

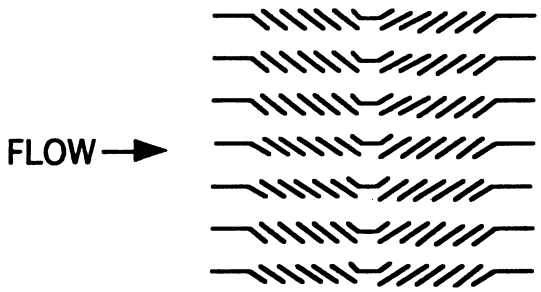

Fig. 1.3 - Top view of a cross section of the louver geometry used by Aoki, Shinagawa, and Suga [25]

In 1989, Zhang and Lang [27] performed a study of the effect of plate angle and length on heat transfer and pressure drop in a louvered fin array. Their array consisted of rows of in-line plates with five plates per row. They investigated three different plate lengths and five plate angles ranging from 10° to 35° for $500<Re_L<2300$. They found the Sherwood number to be constant following the fourth row of fins. For what they defined as the fully developed regime of turbulent airflow, they developed the following correlation for the Sherwood number:

$$\overline{Sh} = 0.569\left(\frac{\theta\pi}{180}\right)^{0.543}\left(\frac{L}{p}\right)^{0.7} Re_L^{0.7} \qquad [1.3]$$

$0.75 \le L/p \le 1.25$, $t/p = 1/20$, $10° \le \theta \le 35°$

For locomotive radiators, they found the best geometry to be with $\theta=25°$ and L=2-2.5 mm. For automotive radiators with a Re range of 690-1900, they reported that $\theta \approx 20°$ may be appropriate.

In 1990, Hiramatsu, Ishimaru, and Matsuzaki [28] looked at a geometry similar to that studied by Aoki, Shinagawa, and Suga. They numerically analyzed the geometry for $100 \le Re_{lp} \le 500$ (and $0° \le \theta \le 50°$. Like Suga and Aoki, they used a steady state code. They also performed flow visualization on a model ten times as large as an actual louvered-fin geometry by injecting ink into the flow. For this case, the louvers were at an angle of attack of 25°, and the Reynolds number ranged from 100 to 1000. They explained that for small Reynolds numbers and large fin pitches it is difficult for fluid to pass through the louvers. As a result, heat transfer is low.

Webb and Trauger [29] performed flow visualization using the dye injection technique on a similar geometry in 1991. They developed correlations for flow efficiency, which they defined as the distance the flow travels in the transverse direction divided by the distance it would have traveled had it traveled parallel to the louvers. Low flow efficiency may correspond to low j and j/f performance. They found the flow to be purely laminar for Reynolds numbers (based on louver pitch) less than 500-600. Smaller fin spacing leads to wake instability at higher Reynolds numbers. They also found flow separation and recirculation zones to be stronger in the entrance region than further in the array.

Huang and Tao [30] and Lue, Huang, and Tao [31] used the naphthalene sublimation method to analyze in-line plates with an angle of incidence of 25°. Like Zhang and Lang, they found the flow to be developed after the fourth row of plates. However, the length of the developing region increases with increasing Reynolds number and transverse pitch. They concluded that the flow becomes fully developed faster than the mass transfer does; both are fully developed by the fifth row of the array. In addition, if all of the plates in a given column (parallel to the flow) are coated with naphthalene, the developing region is shorter than if only one test fin were coated. They found that the effects of the afterduct behind the test section cause the Sherwood number in the last row to decrease slightly. They concluded that flow through arrays with alternating long and short plate lengths experience higher heat transfer for a fixed pumping power than if the plate lengths were uniform. They explained that at low Reynolds numbers the heat transfer for an array of non-uniform plates is higher than for an array of uniform plates because the average plate length is shorter. At higher Reynolds numbers the array of uniform plates provides higher heat transfer. However, the array of non-uniform plates requires a lower pumping power than does the array of uniform plates .

Finally, in 1995, Cowell, Heikal, and Achaichia [32] compared several compact louvered fin surfaces by analyzing previous publications. They presented a correlation for the Stanton number based on Reynolds number and surface geometry. Comparing louvered fins to offset strip fins, they found that for a given amount of heat transfer, louvered fins can have a larger hydraulic diameter. However, pumping power is also somewhat higher for the louvered fins. A designer may choose offset or louvered fins depending on the importance of size, weight, and pumping power for the application.

1.3 Objectives

The objective of this study is to develop a better understanding of flow and heat transfer through louvered and offset strip fins so that design guidelines may be developed. In order to achieve this objective, the following tasks will be accomplished: 1) The relative importance of

boundary-layer restarting and vortex shedding to heat transfer and pressure drop performance under different operating conditions will be determined. Several methods to detect the presence of vortex shedding in an array will be developed. 2) The local heat transfer behavior and its effect on fin design will be investigated. 3) The effect of heat exchanger geometry on flow unsteadiness and heat transfer will be analyzed. This study is the first phase of ongoing work in the area of louvered fin heat exchangers which will culminate in guidelines for design engineers.

This study was performed through the experimental determination of pressure drop and local and average heat transfer behavior for two offset strip and three louvered-fin arrays and through flow visualization of one of the offset strip arrays. Experiments were performed for a Reynolds number range of approximately $250 \leq Re \leq 6000$. For the louvered geometries, an angle of attack of 25° was used. This angle was used since it is within the range of louver angles commonly used in the applications of interest, and Zhang and Lang [27] found flow through fins with this angle to be one of the most efficient. Since heat and mass transfer are analogous, as demonstrated in Appendix A, heat transfer data can be acquired through mass transfer experiments. Mass transfer data, acquired using the naphthalene sublimation method, are presented in the form of Sherwood numbers and Colburn j factors, and pressure drop data are presented in the form of friction factors and pumping power. Flow visualization was performed using the ink injection technique.

CHAPTER 2 - EXPERIMENTAL APPARATUS

The experimental apparatus consisted of five main subsystems: 1) the wind tunnel and test section, 2) the wind tunnel instrumentation and data acquisition, 3) the laser profilometer, 4) a microphone and dynamic signal analyzer, and 5) the water tunnel.

2.1 Wind Tunnel and Test Section

The wind tunnel, shown schematically in Fig. 2.1, was operated as a single-pass, induction wind tunnel. It drew air from the room and discharged it outside the laboratory

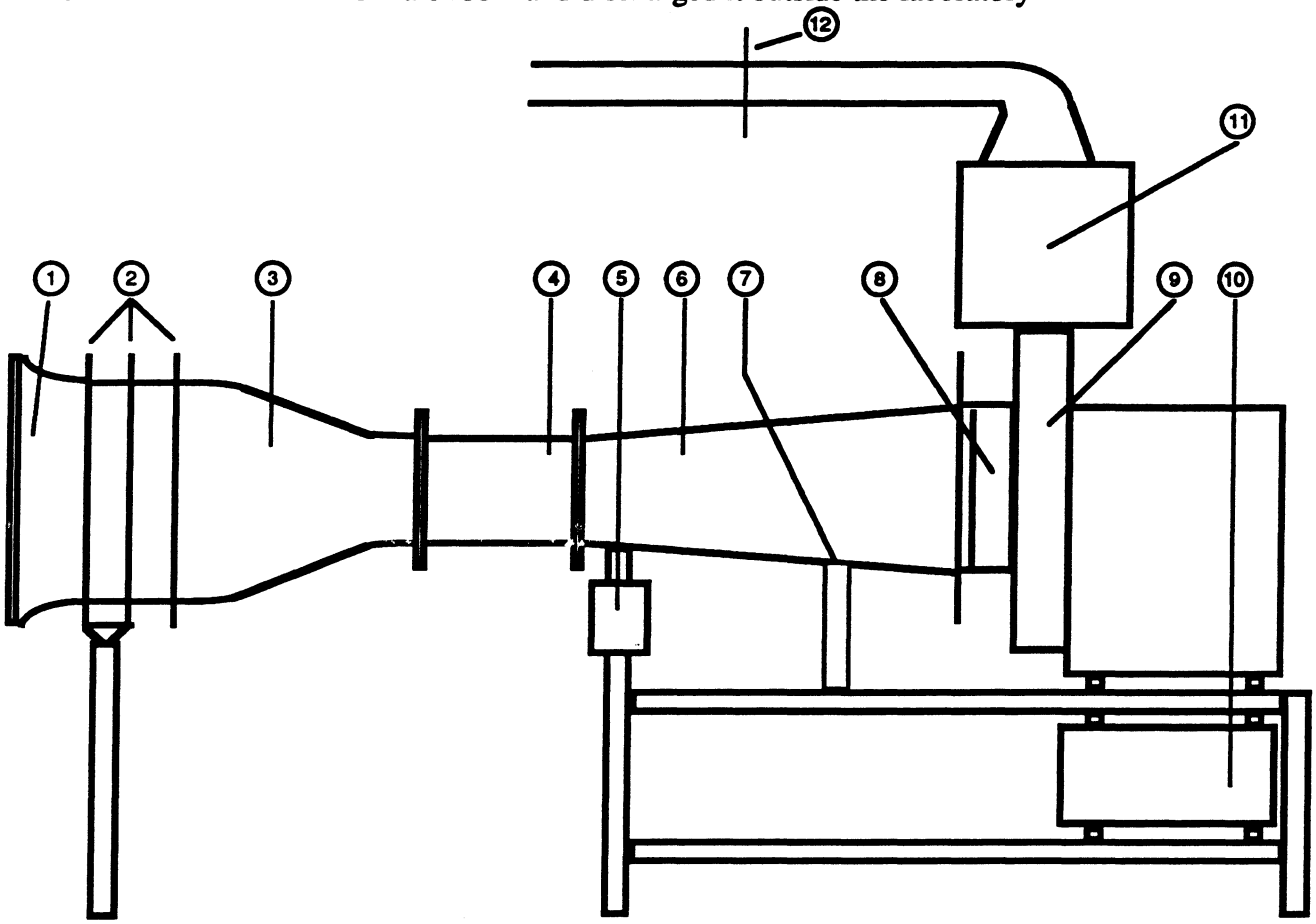

1. Elliptical Inlet
2. Flow Straighteners
3. 9:1 Contraction
4. Test Section
5. Control Key Pad
6. Diffuser
7. Isolation Mount
8. Flexible Coupling
9. Fan
10. Electrical Cabinet
11. Acoustic Duct
12. Orifice Plate

Fig. 2.1 - Schematic of wind tunnel used for mass transfer and pressure drop experiments

The wind tunnel entrance consisted of an elliptical inlet which included hexagonal-cell honeycomb and screens to condition the flow. The inlet and other ducts were constructed of reinforced fiberglass and coated with a smooth gel-coat surface. Downstream of the inlet, the flow passed through a 9:1 contraction and into the 15.24 cm x 15.24 cm (6"x6") square test section. For most experiments, honeycomb flow straighteners were present downstream of the test section as well. The reason for these straighteners is discussed in Section 4.1.4. The test section and downstream flow straighteners could be removed to accommodate other test sections. In the test section, the freestream velocity profile was uniform to within approximately 2% as shown in Fig. 2.2. These example data were recorded using a hot-wire anemometer centered vertically in the test section; x* was measured horizontally in the test section. Downstream of the test section, transition from a square to a round cross section was provided by a diffuser that carried the flow to a compact radial blade fan. The fan was powered by a 1.49 kW induction motor.

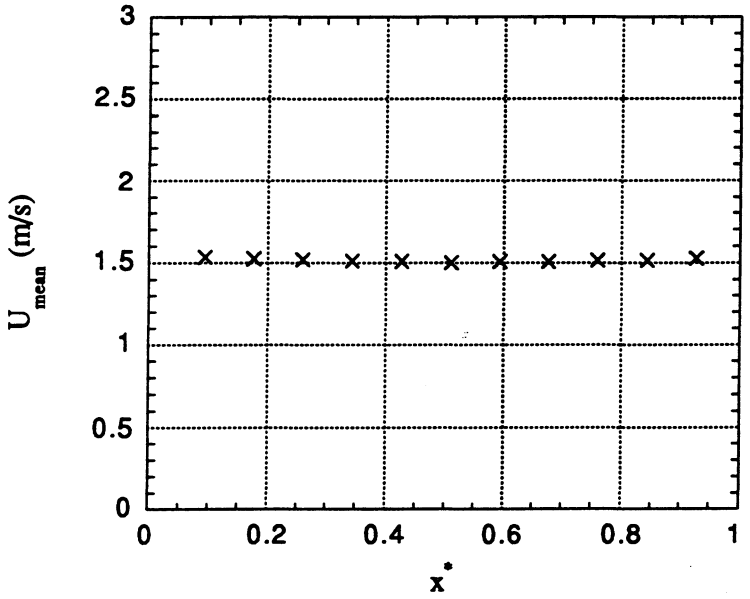

Fig. 2.2 - Freestream air velocity profile at test section inlet with no fins present in the test section

Freestream velocities in the test section could range from approximately 0.1 to 10 m/s. The flow was measured using one of three different orifice plates, depending on the flow rate, which were placed in a 10.16 cm (4 in.) duct. The orifice plates were 10.16 cm (4 in.) OD, ASME

standard plates. The bore diameter was 3.68 cm (1.45 in) for Orifice Plate 1, 5.59 cm (2.20 in) for Orifice Plate 2, and 7.62 cm (3.00 in) for Orifice Plate 3. Four pressure taps were placed one pipe diameter upstream and four presure taps were placed one half diameter downstream of the orifice plate in 90° intervals around the circumference. The pressure drop across an orifice plate was measured with a Dwyer precision electronic manometer with a range of 0-497 Pa ±0.12 Pa (0-2 in water ±0.0005 in). In accordance with the ASME standard [33], a flow conditioning section was placed seven pipe diameters upstream of the plate but more than six diameters downstream of the nearest pipe bend. Downstream of the plate was a length of pipe exceeding the required four pipe diameters specified in the standard. The flow discharged outside of the room to prevent naphthalene from contaminating the laboratory air. For additional details on flow measurement, see Appendix B.

Turbulence intensity in the wind tunnel test section increased with increasing flow velocity and decreasing orifice plate bore diameter, as shown in Fig. 2.3. Turbulence intensity was measured by placing a hot-wire anemometer in an empty test section. Turbulence intensity

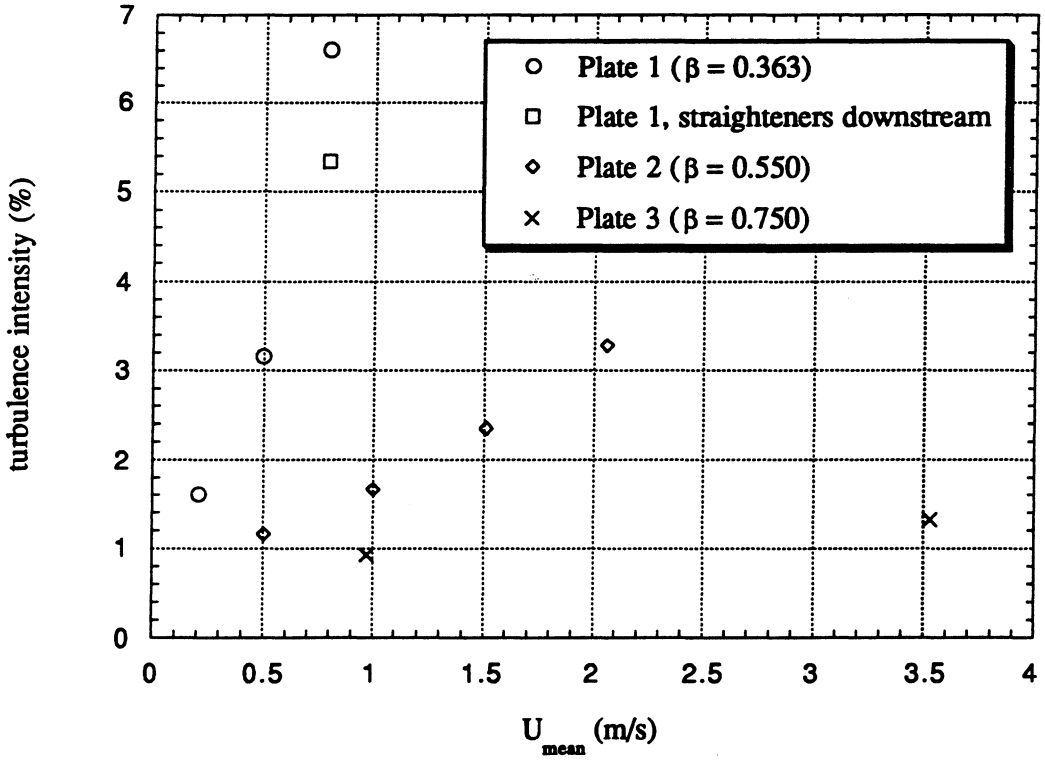

Fig. 2.3 - Turbulence intensity in open tunnel test section with flow velocities inferred using different orifice plates

decreased when flow straighteners were placed downstream of the test section. For most cases, data were taken at the low velocity range for each orifice plate in order to keep turbulence intensity below 3%. Except for the first geometry studied, turbulence intensity in the test section was always less than 2%.

A schematic of the test section is shown in Fig. 2.4. The test section was constructed using 1.27 cm (0.5 in) thick, GM grade acrylic. The test section was 30.5 cm (12.0 in) long, and its interior cross section was 15.24 cm (6 in) square. Holes allowing the insertion of RTDs were located upstream and downstream of the fins. Four static-pressure taps were also located 2.54 cm (1 in) upstream and downstream of the fins, one tap on each side of the test section. The four taps were connected using Tygon tubing. The test section accommodated up to 92 fins in eight rows. For each experiment, one to eleven naphthalene-coated test fins were placed in the middle columns of the test section; uncoated dummy fins made up the remaining fins in the test section. Dummy fins, shown schematically in Fig. 2.5, were placed semi-permanently in the test section

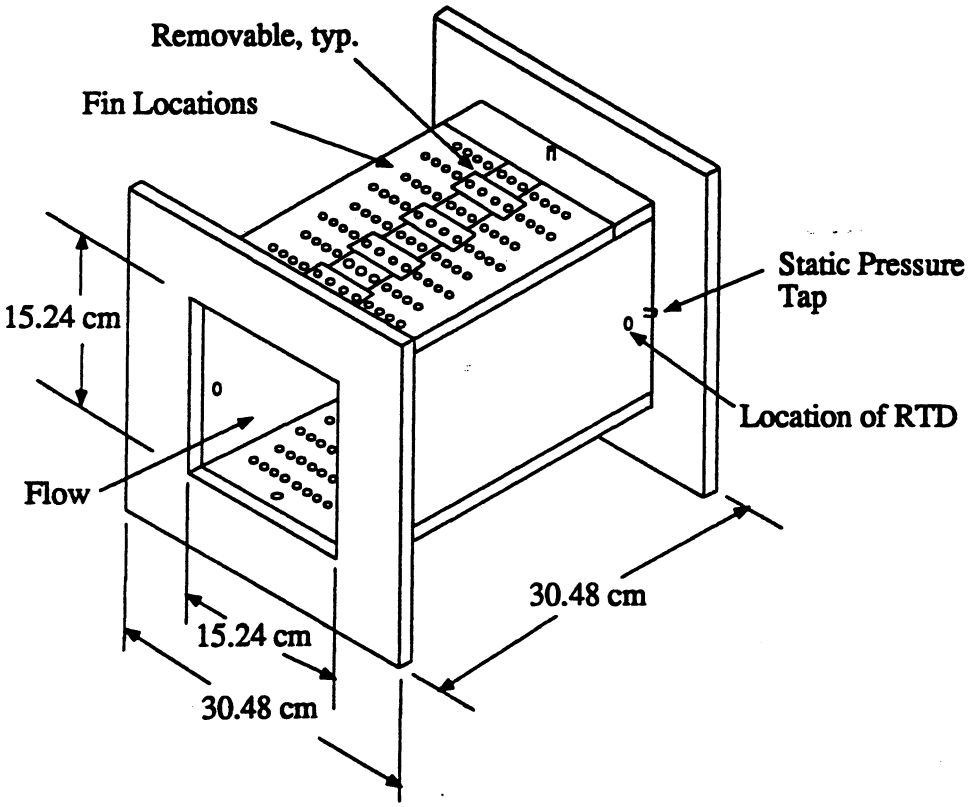

Fig. 2.4 - Schematic of wind tunnel test section used for naphthalene and pressure drop experiments

by removing the top. The ends of the fins fit into holes in the bottom of the test section. The tops of the fins fit into holes in the removable top. The angle of the fins was set using an acrylic sheet with angled slots cut into it. This sheet was screwed to the bottom of the test section, and the ends of the fins fit snugly into the slots. To change the angle of the fins, a different acrylic sheet with slots at a different angle was screwed to the section. Different fin configurations were possible by attaching tops and bottoms with holes placed at different locations. The eight center pieces of the top were easily removable to allow the quick insertion and removal of test fins. The naphthalene filled cavity of each test fin, shown in Fig. 2.5a, was 0.10 cm (0.040 in) deep and 2.44 cm (0.96 in) wide on the 2.54 cm (1 in) wide fin. The five different fin configurations used in this study are shown in Fig. 2.6.

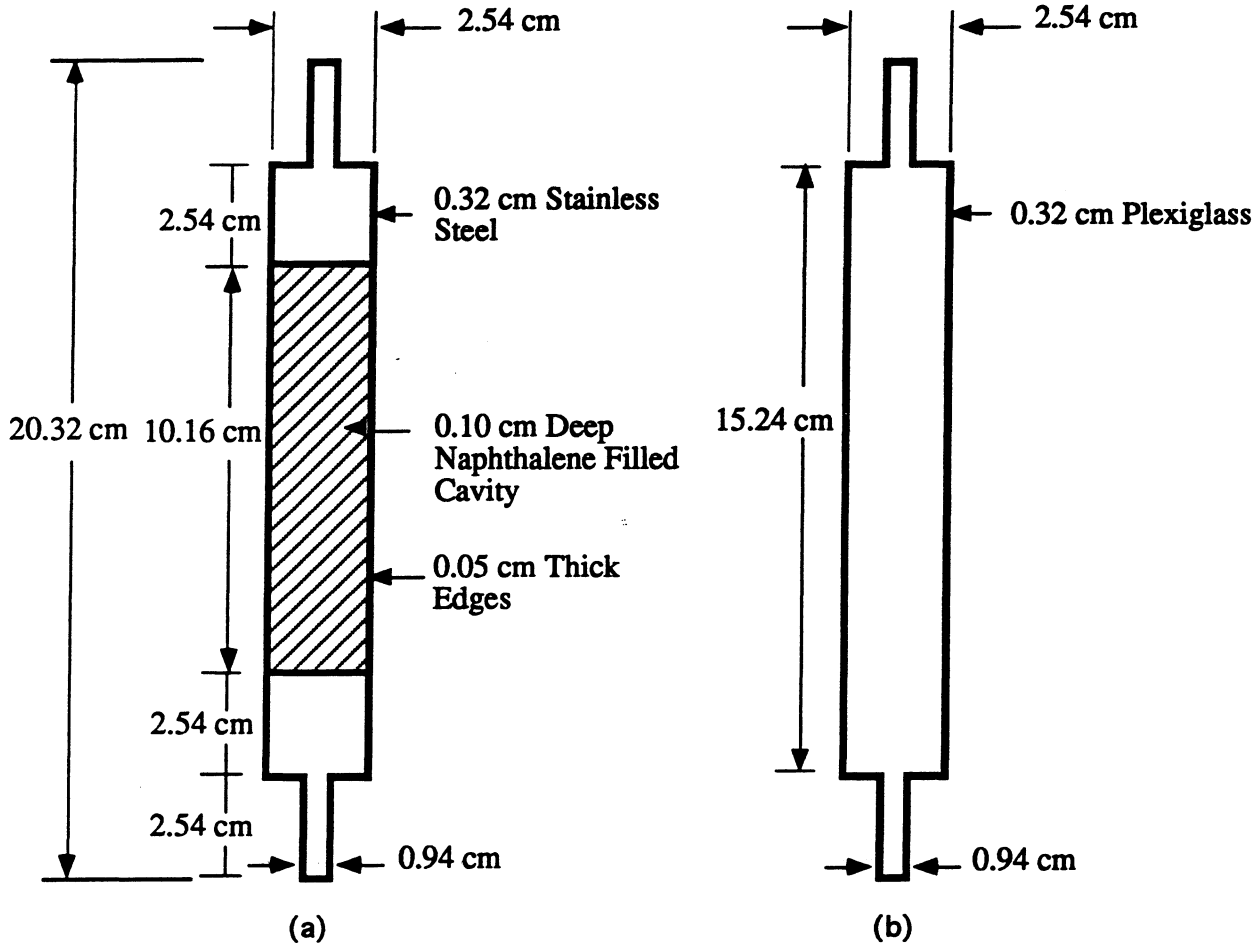

Fig. 2.5 - Schematic of (a) test fin (b) dummy fin used for naphthalene and pressure drop experiments

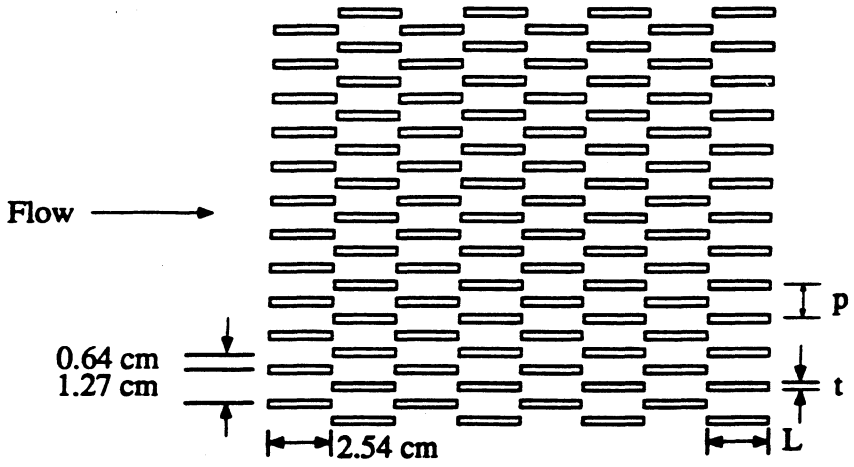

(a)

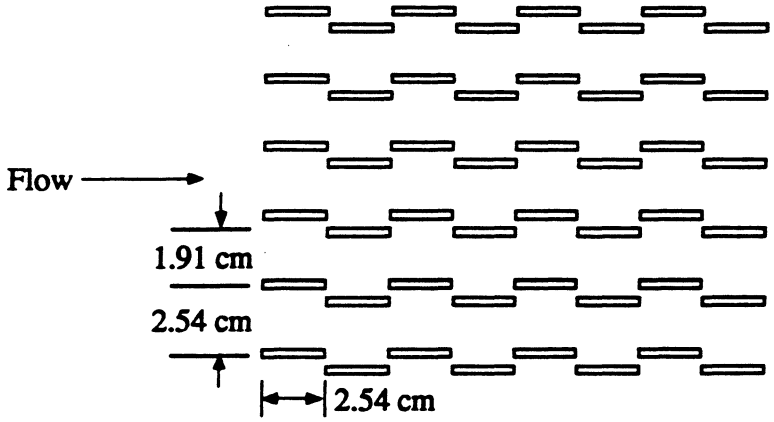

(b)

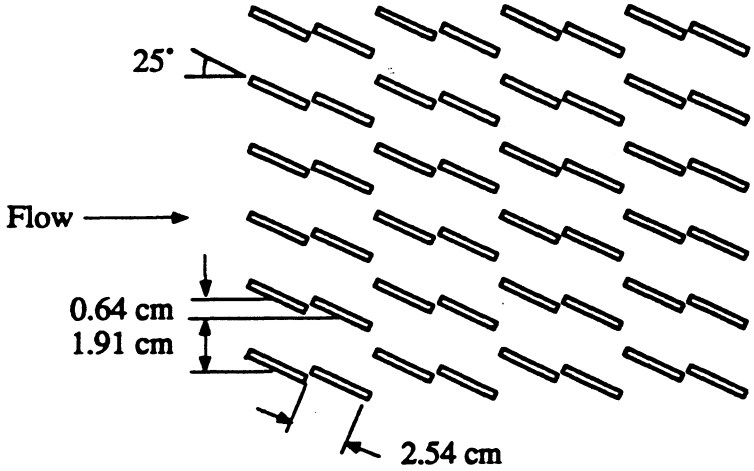

(c)

(Figure caption on next page.)

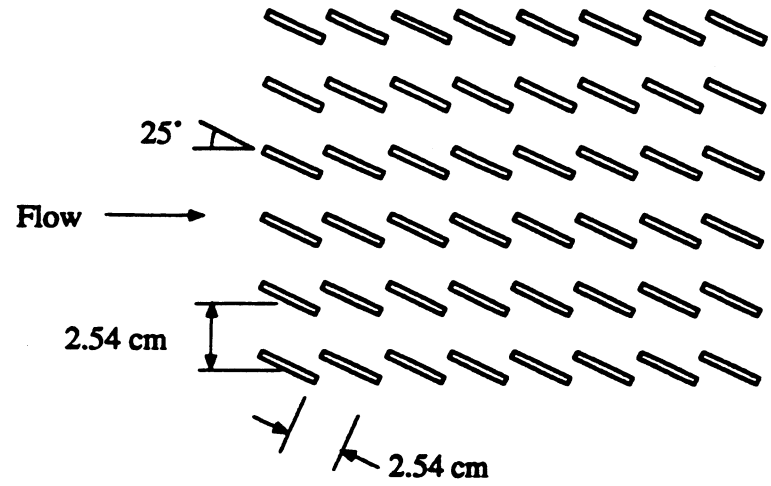

(d)

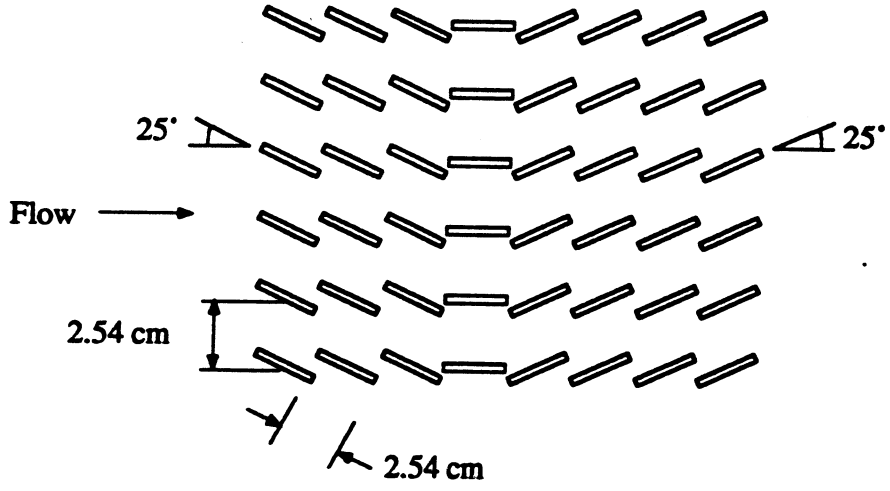

(e)

Fig. 2.6 - Schematics of five fin geometries studied experimentally (a) Offset strip, d_h = 16.9 mm; (b) Offset strip, d_h = 39.6 mm; (c) Staggered louvers, 25° angle of incidence, d_h = 39.6 mm; (d) In-line louvers, 25° angle of incidence, d_h = 39.6 mm; (e) In-line reversing louvers, 25° angle of incidence, d_h = 39.6 mm

2.2 Instrumentation and Data Acquisition

During each run, upstream and downstream temperatures, core pressure drop, relative humidity, barometric pressure, exposure time, and fin mass were recorded in addition to the pressure drop across the orifice plate discussed earlier. The upstream and downstream air temperatures were recorded using calibrated platinum RTDs. The uncertainty of the temperature

measurements was less than 0.1° C. For a detailed discussion of the calibration procedure and uncertainty analysis, see Appendices C and D. Temperature data were recorded every five seconds throughout each experiment using an A/D card with 12 bit resolution and the data acquisition software *Workbench*. The temperatures were time averaged throughout the run, and these values were used in the data reduction equations given in Appendix B. The pressure drop across the core was measured using a pressure transmitter with a range of 0-24.9 Pa (0-0.1 in water). The pressure drop readings were also displayed using *Workbench*. For pressure drops larger than 24.9 Pa (0.1 in water), the electric manometer was used. The relative humidity was determined using a humidity indicator and the barometric pressure using a mercury barometer. Test fins were weighed before and after tests using a Mettler 200 g balance with an accuracy of ±0.00005 g.

2.3 Laser Profilometer

Local sublimation depths on the naphthalene fins were determined using a laser triangulation system based on the concept shown in Fig. 2.7. Laser triangulation is an optical, non-contact method of determining surface contours. A laser beam focused on a surface is reflected and passes through a lens into a photodetector. Surfaces of different heights reflect the beam to different positions on the photodetector. For these experiments, a Cyber-Scan 206 profilometry system (Cyber Optics Corp) was used. The published accuracy of this system is ± 1% of the sensor's range -- 4 μm. However, repeated scans of the stainless steel base of the fins show the accuracy to be closer to ± 6 μm. A complete description of this system is given by Kearney [34].

2.4 Frequency Analysis

The frequency content of the test section flow was determined using a dynamic signal analyzer (Hewlet Packard model 3562A). A microphone was placed in the test section 2 cm downstream of the fins. This microphone was connected to an acoustical interface and routed to

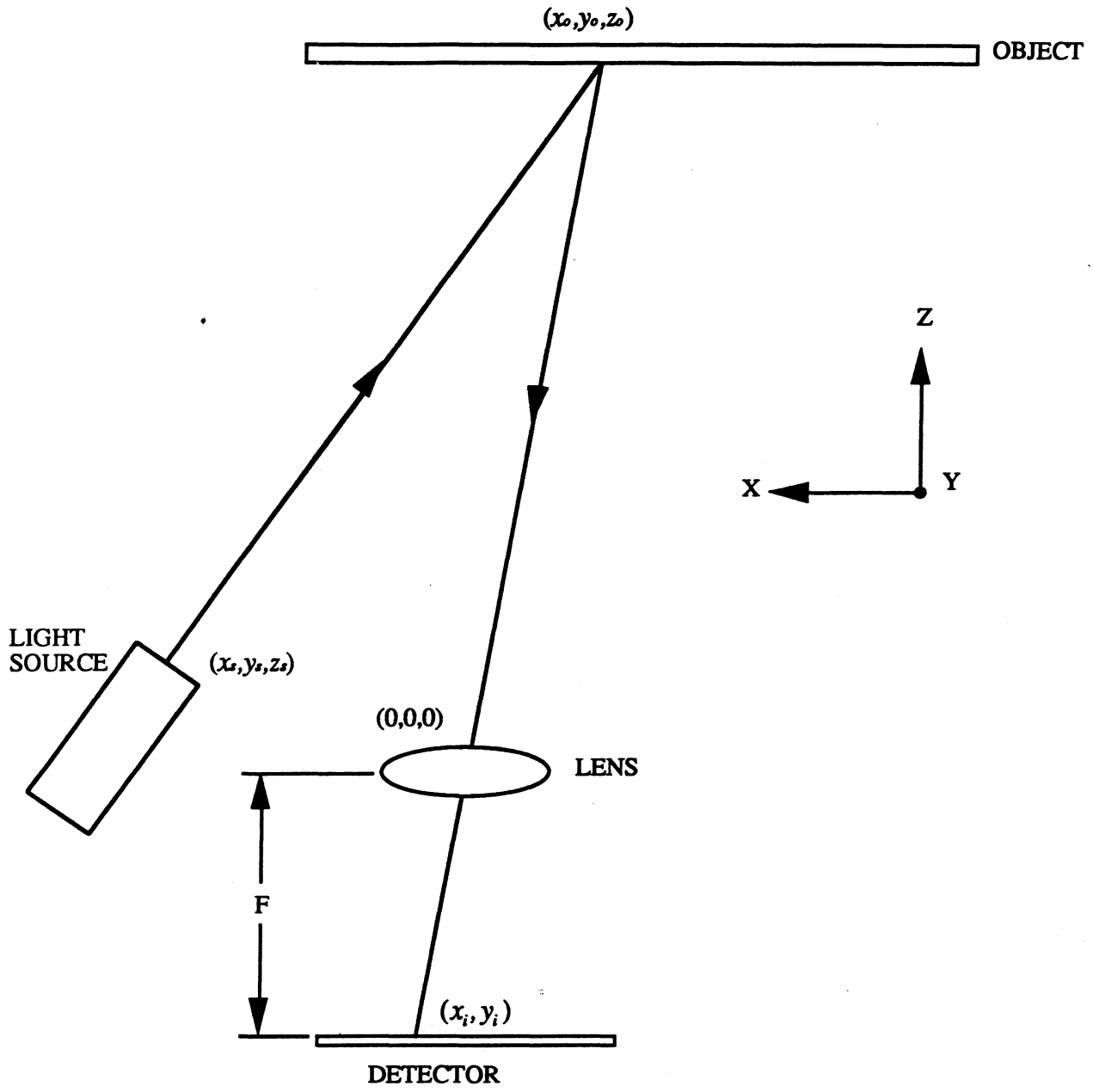

Fig. 2.7- Schematic of laser triangulation technique used to determine local sublimation depths on naphthalene fins [35]

the signal analyzer. The signal analyzer was configured to perform a Fast Fourier Transform (FFT). For a more detailed explanation of the FFT, see Appendix E. The resulting power spectrum displayed signal intensity (-100 to -40 dB) versus frequency (1-1000 Hz). For each power spectrum, ten sets of data consisting of 240 points each were collected and averaged.

2.5 Water Tunnel

The closed-loop water tunnel used for the flow visualization experiments is shown schematically in Fig. 2.8. The water was pumped through a plenum, a section of honeycomb, the contraction, and into the test section. The test section was the same as that used in the wind tunnel except that it was watertight, and there was an 8.9 cm (3.5 in) section upstream of the first row of fins and a 16.5 cm (6.5 in) section downstream of the last row. The total length of the section was 45.7 cm (18 in). A hole was cut in the top of the test section approximately 2.5 cm (1 in) upstream of the first fin. Dye was injected into the flow using a 1.3 mm (0.05 in) diameter needle with its end bent in the direction of the flow. The needle was connected to the dye reservoir using rubber tubing. The amount of dye injected, which was gravity-fed, was regulated by opening or closing a valve at the base of the dye reservoir. The dye consisted of blue, red, or green food coloring mixed with water. The bottom of the test section was viewed by placing a mirror under the test section, and additional contrast was gained by painting the bottoms of the fins black. Photographs of the mirror were recorded using a 35 mm camera.

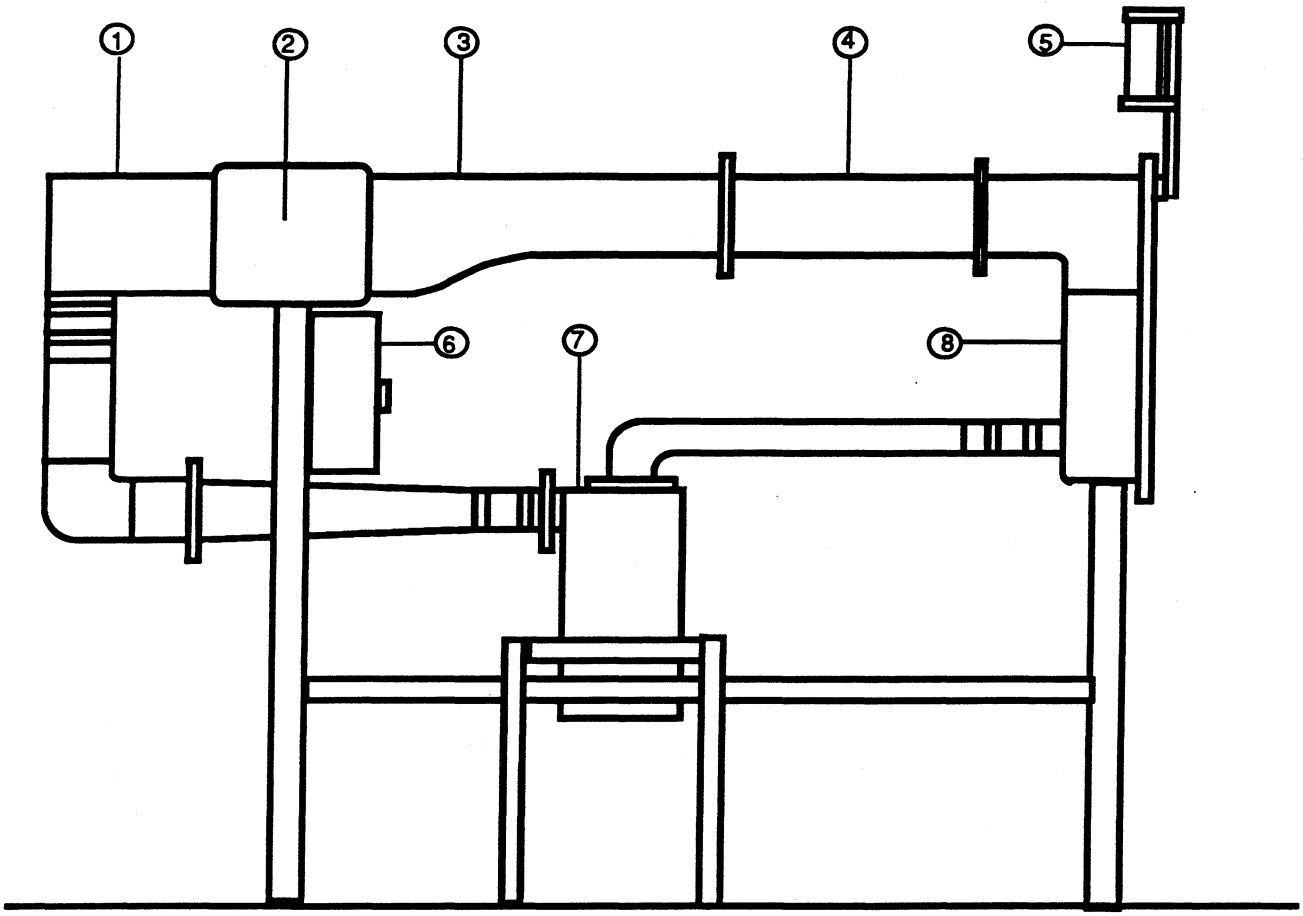

1. Plenum
2. Honeycomb
3. Contraction
4. Test Section
5. Dye Reservoir
6. Electrical Cabinet
7. Pump
8. Return Plenum

Fig. 2.8 - Schematic of water tunnel used for flow visualization experiments

CHAPTER 3 - PROCEDURE AND DATA INTERPRETATION

3.1 Preparation of Naphthalene Specimens

Test fins were constructed by pouring molten naphthalene into the cavity in the stainless steel fins shown in Fig. 2.5. For the offset strip geometries, usually eleven fins were cast. Eight of the fins were coated with naphthalene on one side, and three of the fins were coated on both sides. These fins were placed in the center of rows 1-7 of the test section to make a symmetric channel completely bounded by naphthalene coated fins. For the louvered geometries, usually either one fin with naphthalene on both sides or two fins in consecutive rows with naphthalene on only one side were used. These fins faced opposite directions to simulate one two-sided fin. When only one or two test fins were used, they were placed in the last rows of the test section where the flow was fully developed.

To make the fins, scintillation-grade naphthalene (99+% pure) was heated above its melting point of 80.2 °C in a beaker. The molten naphthalene was poured into the cavity until it rose above the edges of the fin. After solidification, the excess was removed using a three-fold process. First, most of the excess naphthalene was removed by repeatedly passing a razor over the naphthalene surface with the edges of the razor touching the edges of the cavity to ensure that the naphthalene surface would be the same height as the fin surface. Second, a smooth, even finish was obtained by polishing the surface with 150-grit sandpaper. Finally, the fins were inspected and any voids filled. Due to the fast cooling rate during this process, an amorphous naphthalene microstructure rather than a crystalline microstructure resulted. This amorphous microstructure was desirable since the laser profilometer was found to give more consistent surface scans with this surface structure.

3.2 Mass Averaged Experiments

Since heat and mass transfer are analogous (as discussed in Appendix A), mass transfer experiments were performed instead of heat transfer experiments. Mass averaged data were obtained by weighing the test fins before and after exposure in the wind tunnel. Before each run the test fins were weighed using the balance, which was allowed to warm up for at least an hour beforehand. The fins were then placed in the tunnel, and the tunnel was turned on. At the same time, a stop watch and the data acquisition system were started. RTD temperatures were recorded every 5 seconds throughout each experiment. Half way through the run, the barometric pressure, relative humidity, and pressure drop across the core and orifice plate were recorded. After the run was finished, the fins were removed and weighed again. The experiments ranged from 45 to 90 minutes in duration, depending on the Reynolds number. At high Reynolds numbers, fins were exposed for a shorter period of time to ensure that excessive sublimation did not distort the fin surface. At low Reynolds numbers, fins were exposed for a longer period of time to keep uncertainty in the mass measurements small.

The time taken to weigh the fins twice and insert and remove them was approximately three minutes. By weighing a fin, exposing it to the laboratory environment for several minutes, and re-weighing it, an approximate natural sublimation rate was determined. These tests proved that corrections for natural sublimation fall within the uncertainty of the average Sherwood number calculation for the experiments reported. Therefore, this correction was ignored for the mass averaged experiments.

The data were reduced using the following equations for the Reynolds number, average mass transfer coefficient, average Sherwood number, modified Colburn j factor, friction factor, and pumping power. The modified Colburn j factor was used instead of the conventional Colburn j factor since Sparrow and Hajiloo [12] suggested that the modified j factor is more accurate for intermediate values of the Schmidt number. The reader is directed to Appendix B for more information on data reduction.

$$Re = \frac{U_c d_h}{\nu} \qquad [3.1]$$

$$\bar{h}_m = \frac{\Delta m}{A_f \rho_{n,v} \Delta t} \qquad [3.2]$$

$$\overline{Sh} = \frac{d_h \overline{h_m}}{D_{na}} \qquad [3.3]$$

$$j = \frac{\overline{Sh}}{ReSc^{0.4}} \qquad [3.4]$$

$$f = \frac{2\Delta P}{\rho U_c^2}\left(\frac{d_H}{4L_{core}}\right) \qquad [3.5]$$

$$PP = U_c A_c \Delta P \qquad [3.6]$$

3.3 Local Mass Transfer Experiments

Except for the use of the laser profilometer, the local mass transfer experiments were similar to the mass averaged experiments. No more than one fin was scanned for each experiment. Prior to its first weighing, the test fin was scanned using the laser profilometer. The scan covered a 7.62 cm x 2.54 cm (3"x1") area in the center of the fin in a grid of 60 x 20 equally spaced points. After exposure in the tunnel, the fin was weighed and scanned again. To verify that the same area was scanned each time, the mounting fixture shown in Fig. 3.1 was constructed. Normally an object being scanned is placed on the specimen stage beneath the laser profilometer. The laser is stationary, and stepper motors position the stage underneath it. For these experiments, the fixture was placed on the stage with its edges flush with the edges of the stage. The tabs at the top and bottom of the fin kept the body of the fin from touching the bottom of the fixture. In this way, any particles that adhered to the back of the fin body or the fixture, such as dust, would not affect the orientation of the fin on the fixture. The fixture was placed on the specimen at least four hours before scanning, and the stepper motors which

controlled the movement of the stage were turned on. This long warm-up period was necessary to reduce errors due to thermal drift. As the motors warmed up, heat was transferred to the laser base, which was constructed partially of aluminum. If the base were not allowed to warm up before a test, it would expand between the first and second scans, causing significant errors.

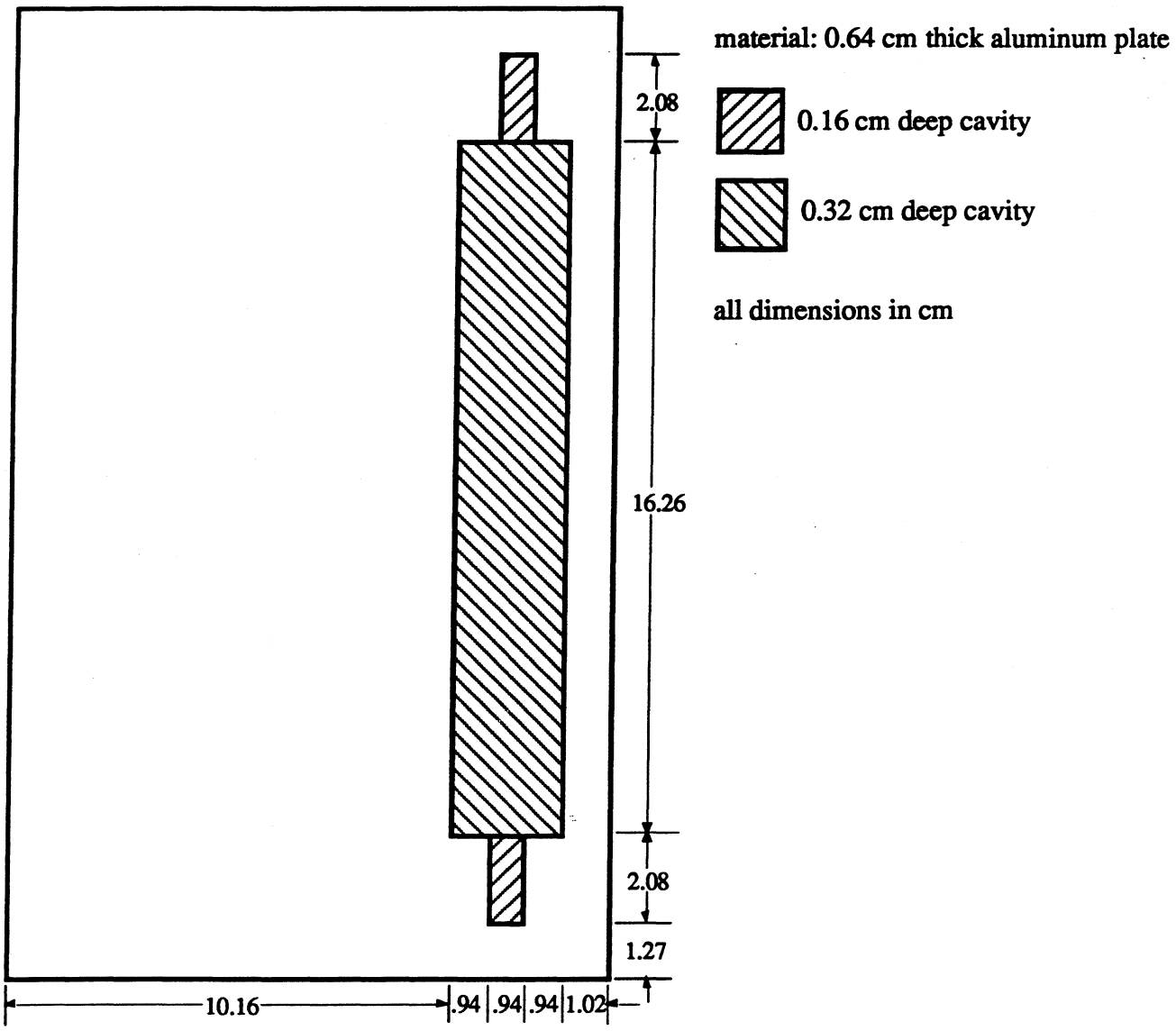

Fig. 3.1 - Mounting fixture for fin during surface profile measurements

Natural sublimation occurred during the eight minutes required to scan a fin. Since the vapor pressure of naphthalene is highly dependent on temperature, a high laboratory temperature could cause natural sublimation to be significant. Therefore, the amount of sublimation due to natural

convection was checked during each local mass transfer experiment. To compensate for that sublimation, two scans were conducted at the end of the test. By subtracting the values acquired during these two scans, the sublimation depth due to natural convection during a scan could be determined. This value could then be subtracted from the sublimation depths caused by forced convection; however, this process proved to be unnecessary. The natural sublimation depths were within the error of the laser profilometer, so they were neglected. The local mass transfer data were reduced using the following equations. Once again, the reader is directed to Appendix B for a more thorough treatment of the data reduction.

$$h_m = \frac{\rho_{n,s}\delta_{sb}}{\rho_{n,v}\Delta t} \qquad [3.7]$$

$$Sh = \frac{h_m d_h}{D_{na}} \qquad [3.8]$$

As a check, the local Sherwood numbers were integrated and compared to the mass-averaged Sherwood numbers using the following formula:

$$\overline{Sh}_{int} = \frac{1}{N}\sum Sh \qquad [3.9]$$

If $\overline{Sh}_{int}$ were not within 10 % of the mass-averaged Sherwood number, the local data were rejected.

3.4 Frequency Analysis

The frequencies present in the test section were analyzed under twelve different conditions. The microphone was fastened in a hole in the test section approximately 2 cm downstream of the last row of fins. To ensure that the microphone was not picking up vibrations from the test section walls, two identical tests were first performed -- one with the microphone fastened in the hole and one with the microphone suspended in the hole without touching the test section. Since the power spectra for these two cases were identical, the microphone was fastened in the hole for the remainder of the runs. A power spectrum of the background noise was

recorded. For the rest of the cases, the presence or absence of fins in the test section, flow straighteners downstream of the test section, an orifice plate, and the contraction was recorded (One test was performed with the contraction removed.). If an orifice plate was present, its bore diameter was recorded. For each case the blower frequency was recorded. For several of the blower frequencies, the blower blade passing frequency was determined. A piece of metallic tape was placed on one of the blower blades, and a strobe light was used to determine its passing frequency. Knowing that the blower had six blades, the overall blade passing frequency could be easily determined.

The FFTs were performed over a frequency range of 1-1000 Hz. It was hoped that the fins' vortex shedding frequency would be evident in the power spectra. In this analysis, the Strouhal number based on fin thickness was used:

$$Sr = \frac{nt}{U} \qquad [3.10]$$

Here n is the shedding frequency. To determine a target frequency range, the Strouhal number was estimated to be 0.21, the value for a sphere at moderate Reynolds numbers. Using this approximation, the shedding frequency was estimated to be between 50 and 100 Hz for each situation studied. Therefore, the frequency range for the FFT was chosen to be 1-1000 Hz. It was also noted that no significant behavior was observed above 1000 Hz.

3.5 Water Tunnel Experiments

The water tunnel was used to conduct flow visualization experiments. Ink was injected into the flow upstream of the first louver. The position at which ink was injected was carefully monitored since it determined what flow structures became visible. The water velocity was determined by measuring the amount of time necessary for the ink to pass through the 20.3 cm (8 in) test section. Photographs were taken of flow behavior around individual louvers and throughout the array. As the flow velocity was increased, the position of the row at which fins

first began to shed vortices was recorded. Since this number was not always clear, some judgment was exercised in obtaining these results.

CHAPTER 4 - RESULTS AND DISCUSSION

The results are presented in terms of six parameters--Reynolds numbers, local and average Sherwood numbers, modified Colburn j factors, friction factors, and pumping power. The baseline offset strip geometry with d_h=16.9 mm, is analyzed first; then it is compared to the other offset strip geometry. The comparison is extended to include the three louvered-fin geometries, and the flow and heat transfer mechanisms are discussed.

4.1 Offset Strip Geometry, d_h = 16.9 mm

4.1.1 Average Mass Transfer Experiments

The experimental data for first offset strip geometry are shown in Figs. 4.1, 4.2, and 4.3. The mass transfer data are for fins in the seventh row of the array. The mass transfer data are presented in terms of Sherwood numbers in Fig. 4.1 and in terms of modified Colburn j factors in Fig. 4.2. Friction factor data are presented in Fig. 4.3. The Reynolds-Colburn analogy shown in Fig. 4.3 is based on a 2.54 cm (1 in) plate (the plate length used in this study) in a uniform flow. The geometric parameters in this study were closer to a louvered than an offset strip geometry and therefore differed from the range of geometric parameters used to develop any offset strip correlations found. The correlations of Wieting [7], Joshi and Webb [19], Mochizuki, Yagi, and Yang [36], and Manglik and Bergles [9] in the figures were extrapolated beyond their range of applicability. They are presented only to validate the trends exhibited by the data and the order of magnitude of the results. Close agreement between these trends and the experimental data was not expected. Above a Reynolds number of about 1000, the experimental j factors fall above those predicted using correlations from the literature, but below Re=1000 the j factors are in close agreement with the earlier work. The experimentally measured friction factors are higher than predicted by earlier work over the entire Re range. It should be noted that uncertainties in pressure drop across the core range from 50% at very low Reynolds numbers to 0.2% at the highest Reynolds numbers, leading to an average uncertainty in f above a Reynolds number of

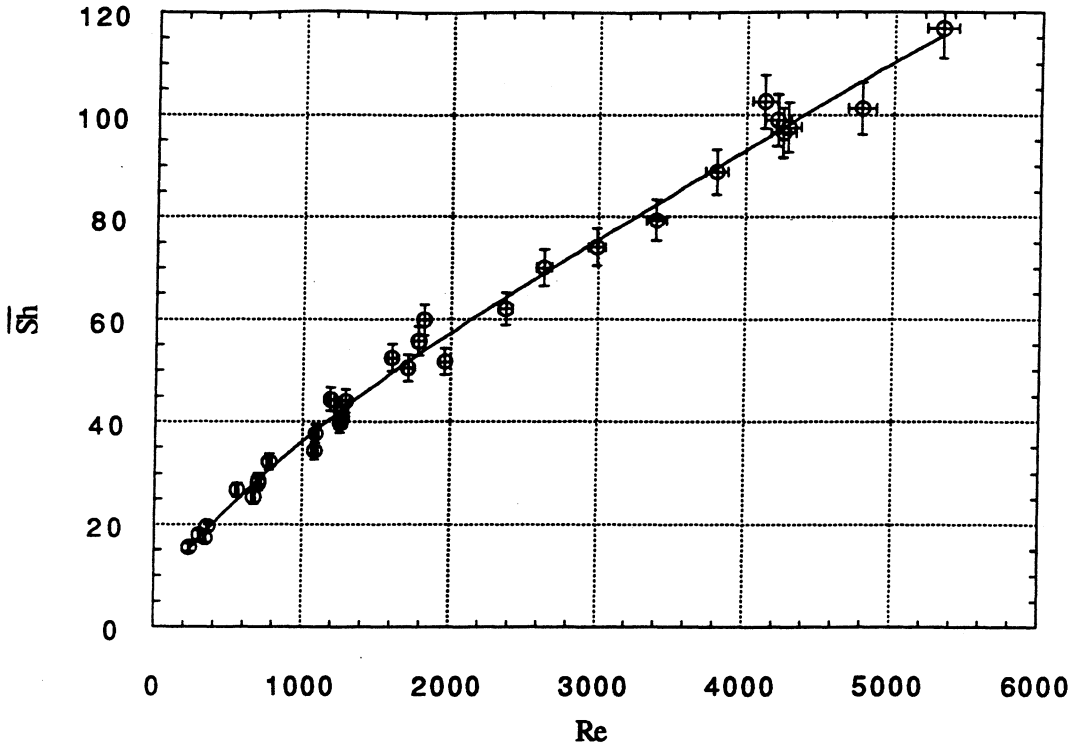

Fig. 4.1 - Average Sherwood numbers for Row 7 of the dense offset strip geometry

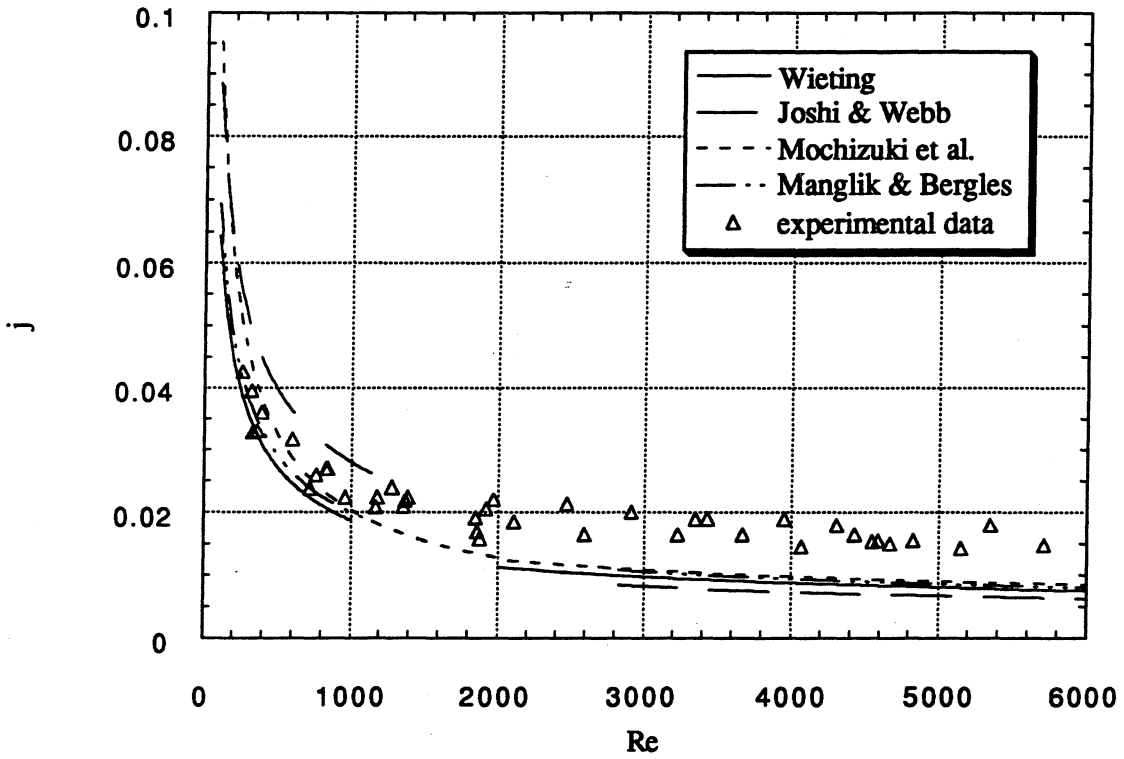

Fig. 4.2 - Modified Colburn j factors for Row 7 of the dense offset strip geometry. Correlations from the literature are for similar geometries

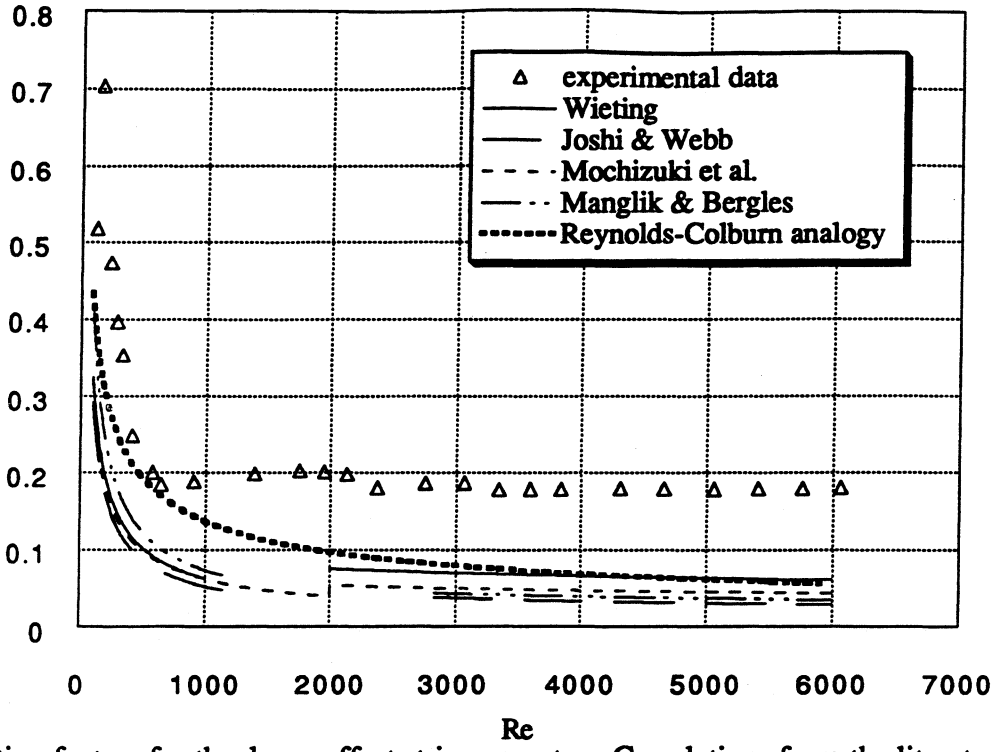

Fig. 4.3 - Friction factors for the dense offset strip geometry. Correlations from the literature are for similar geometries.

1000 of 4%. Despite these differences, it is clear that the data presented here follow the trends presented in the literature.

The relative contributions of boundary layer restarting and vortex shedding to heat transfer under different operating conditions can be identified using the theoretical and experimental results presented in Fig. 4.4. The theoretical calculations assumed a 20.32 cm long continuous plate and 2.54 cm long interrupted plates, similar to the experimental geometry. The difference between the two theoretical values is caused by boundary layer restarting. Heat transfer is high at the beginning of the fin where boundary layers are thin. As the boundary layers thicken, the heat transfer coefficient decreases. Breaking up the fin causes the boundary layers to restart; hence, the average heat transfer is higher, as shown in Fig. 1.2. Below a Reynolds number (based on plate length) of about 700, the experimental values are similar to but slightly higher than the theoretical interrupted plate solution. The discrepancy is expected since the theoretical solution is based on a single plate in the freestream, but the experimental values are for flow

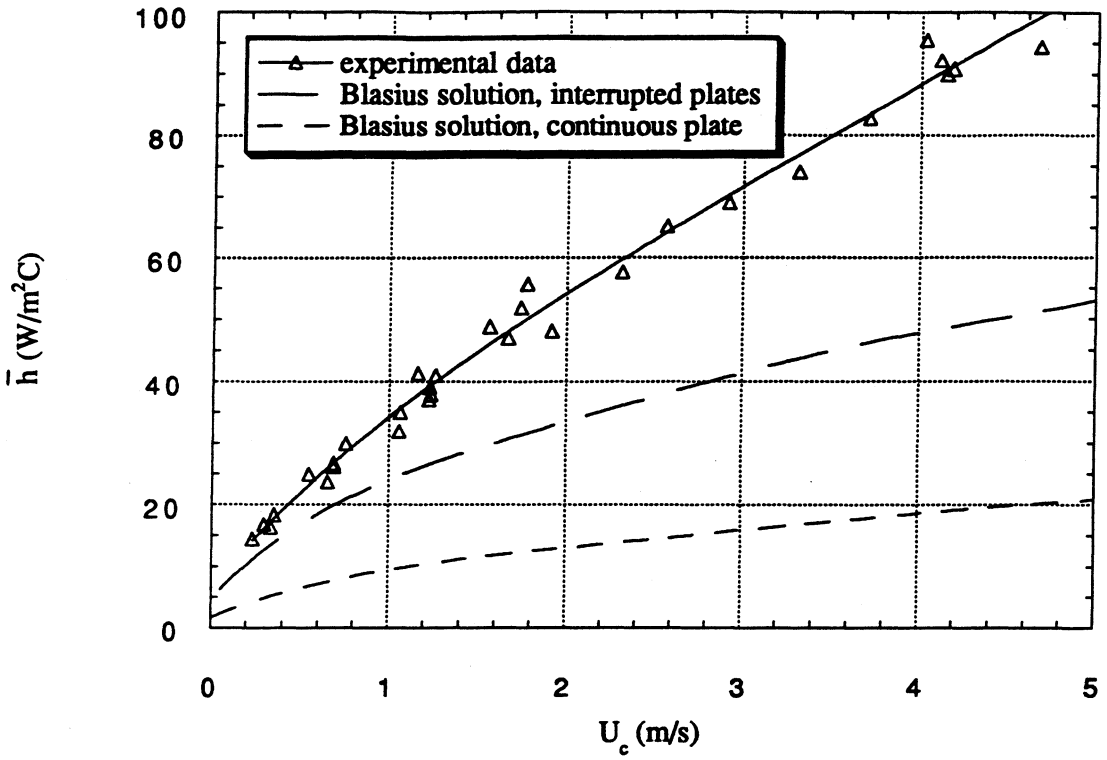

Fig. 4.4 - Experimental and theoretical average heat transfer coefficients; all experimental data taken in Row 7 of the dense offset strip array

through an array of plates. As the air passes through the array, the freestream velocity increases due to boundary layer growth. This acceleration results in thinner boundary layers and increased heat transfer over the single-plate result. At higher Reynolds numbers, the experimental values are significantly greater than the theoretical values because of vortex shedding. As hypothesized by Amon and Mikic [4], Mullisen and Loehrke [18], and others, heat transfer is augmented in this regime by vortex shedding which causes increased mixing. Vortices impinge on the downstream fins causing boundary layers to thin. The simple flat-plate predictions do not account for the heat transfer due to this vortex shedding.

Two experimental methods involving the analysis of mass transfer data were employed to determine whether vortex shedding was present for a particular operating condition. The first method, illustrated in Fig. 4.5, also reveals the row of the array at which vortex shedding began. In Fig. 4.5, Sherwood numbers for fins in successive rows of the array are plotted at various

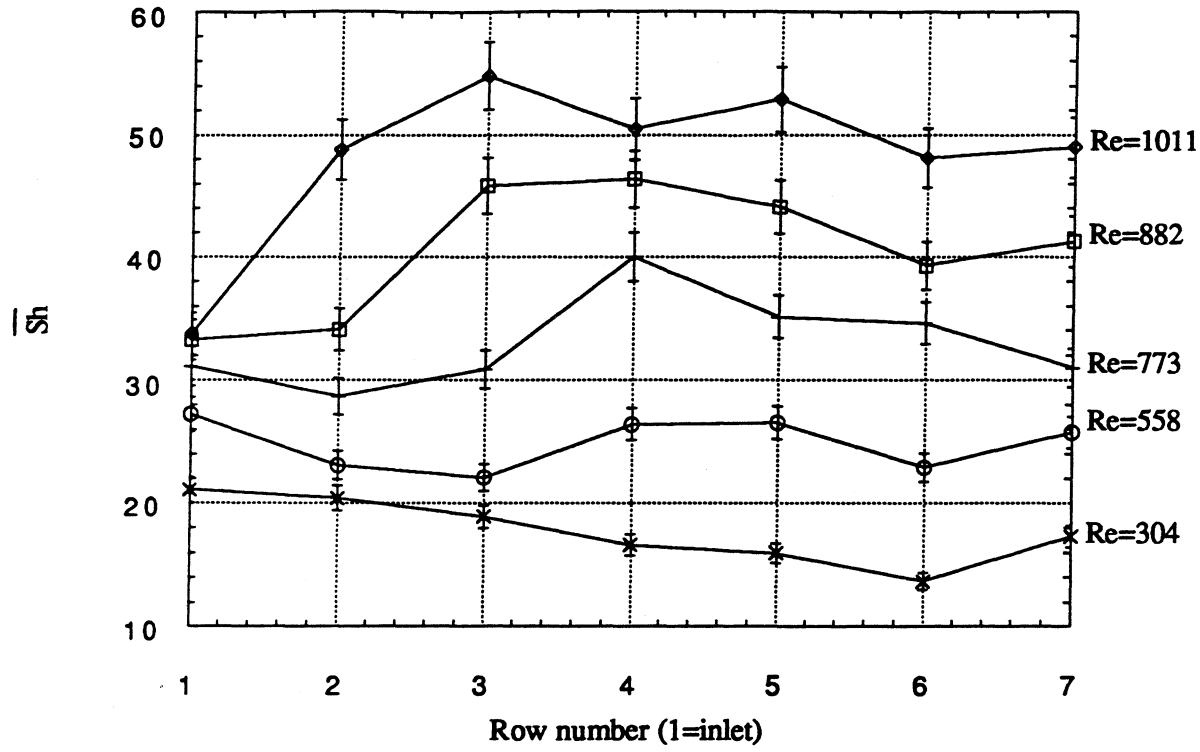

Fig. 4.5 - Average Sherwood numbers for succeeding rows in the dense offset strip array

Reynolds numbers. At low Reynolds numbers, where the flow is laminar and no shedding occurs, the Sherwood numbers decrease slightly or remain constant when proceeding downstream through the array. The decrease is believed to be caused by upstream boundary layers. Since the flow is not well mixed, these boundary layers are not fully destroyed between rows and therefore flow back across the downstream fins, effectively decreasing their heat transfer. As the Reynolds number increases, vortex shedding begins first in the downstream rows. Instabilities caused by upstream fins propagate downstream, causing the vortex shedding to begin first on the fins farthest downstream. Flow visualization, discussed in Section 4.1.3, reveals that as the Reynolds number is increased further, these instabilities increase in magnitude and frequency, and the onset of vortex shedding begins farther upstream in the array until every row is shedding. The location of the onset of vortex shedding in the array is revealed by a dramatic increase in Sherwood number from one row in the array to the next. Vortices increase mixing, which increases heat transfer. Vortices impinge on downstream fins, effectively

decreasing the thickness of the boundary layer by bringing cold fluid close to the fin and carrying warm fluid away. Therefore, when a row in the array first begins to shed vortices, the row downstream will experience an increase in heat transfer. Fig. 4.5 shows that at Re=304, the array is not shedding. By Re=773, or perhaps Re=558, the third and following rows are shedding vortices. By Re=882, the second row is also shedding, and by Re=1011, the entire array is shedding vortices. These results compare favorably with the flow visualization, which is discussed in the Section 4.1.3.

This method to determine the presence of vortex shedding was verified using a second method illustrated in Fig. 4.6. All data for this graph were taken in the seventh row of the array. The eighth (last) row contained dummy fins to mitigate any exit effects. The data entitled "developed flow" were taken with naphthalene coated fins present in the first seven rows. The flow for this situation was both thermally and hydrodynamically developed. The data entitled "developing flow" were taken with naphthalene coated fins present only in the seventh row.

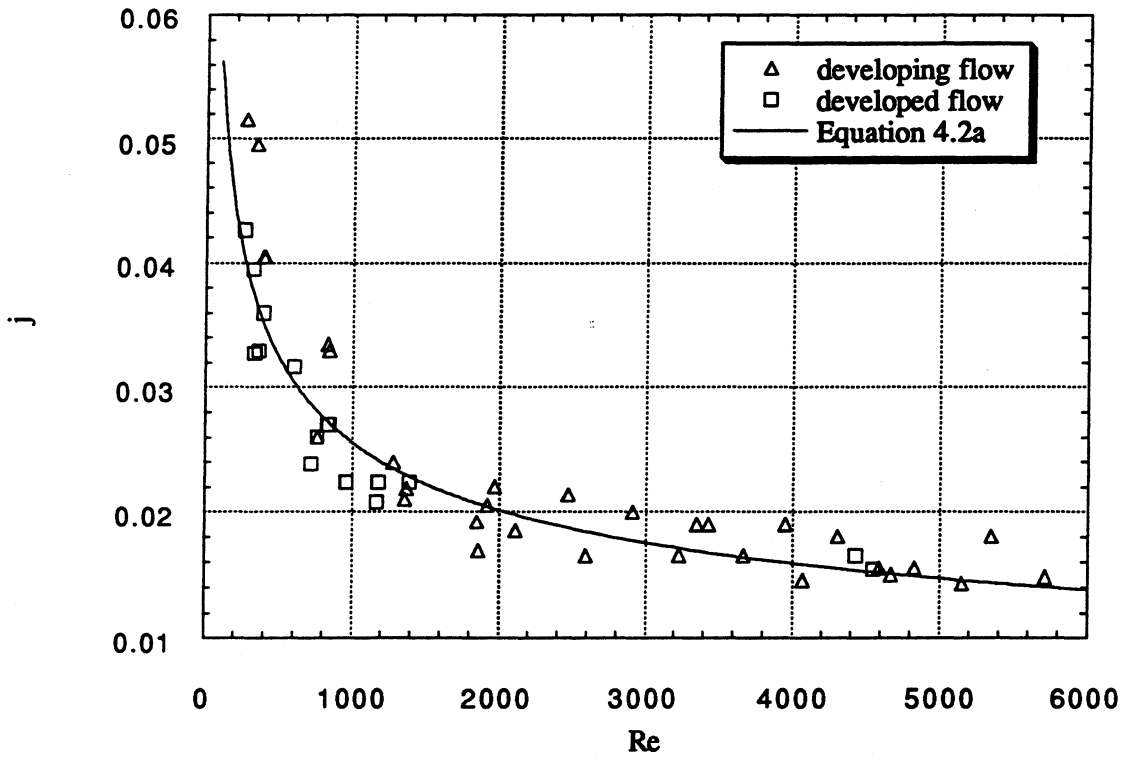

Fig. 4.6 - Colburn j factors for thermally developing and developed flow for the dense offset strip geometry

Dummy fins were placed upstream. Flow proceeding through the array was hydrodynamically but not thermally developed. In the transition and turbulent regimes where vortex shedding was present, the flow was well mixed, and boundary layers from upstream fins were destroyed before they impinged on the downstream fins. Therefore, the presence of naphthalene upstream in the array had little effect on the mass transfer from the fins in the seventh row for those cases with a Reynolds number over about 1000 and the developing flow data fell on top of the developed flow data. Without vortex shedding, the flow was not well mixed, and boundary layers from upstream fins impinged on downstream fins. Therefore, the presence of naphthalene upstream in the array caused mass transfer in the seventh row to be less for the developed flow case than for the developing flow case. Fig. 4.6 shows that as a result, the developing flow data points fall consistently above the developed flow data points at Reynolds numbers less than 1000. Because of the scatter in the data, Fig. 4.6 is not conclusive evidence of this phenomenon. However, it gives credence to the conclusions drawn from Fig. 4.5.

4.1.2 Local Mass Transfer Experiments

The results of the local mass transfer experiments for a low and high Reynolds number case are given in Fig. 4.7. The x^* coordinate on Fig. 4.7 proceeds from the upstream to the downstream edge of one fin. For each position in the x^* direction, 60 sublimation depths were determined along the length of the fin from top to bottom. Each data point is an average of these 60 points. The low Reynolds number case shows evidence of boundary layer growth. The Sherwood number is high at the leading edge and decreases to approximately half that value over the length of the fin. The high Reynolds number case shows evidence of flow separation at the leading edge of the fin and reattachment at $x^*=0.2$ before the boundary layer begins to grow. It must be noted that the average uncertainty in the local Sherwood numbers is 11% with an uncertainty of 24% in regions of low mass transfer and 7% in regions of high mass transfer.

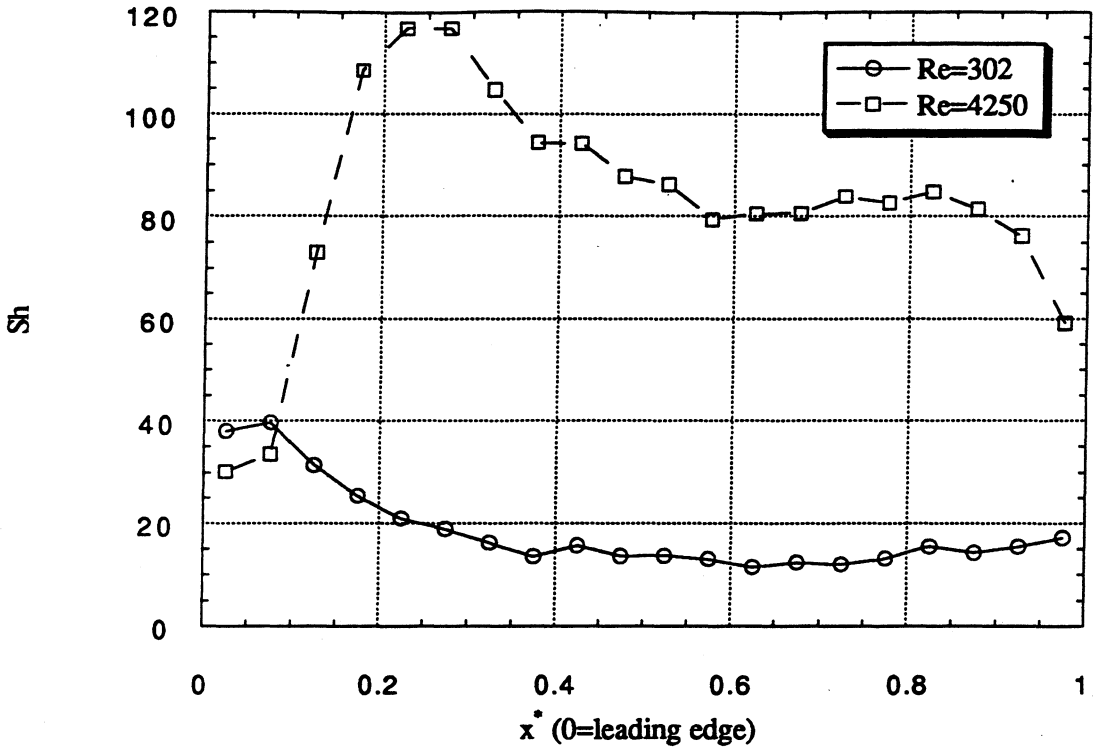

Fig. 4.7 - Local Sherwood numbers in the flow direction for fins in Row 7 of the dense offset strip geometry

4.1.3 Flow Visualization

Figures 4.8a-k are scans of photographs of flow visualization performed at Reynolds numbers ranging from 380 to 1060. The test section was similar to the one shown in Fig. 2.4, but only the middle rows of fins are shown in the scans. The photographs reveal the flow structure. Fig. 4.8a shows that the flow is steady and laminar at Re=380. An example of the steady recirculating eddies that form behind the fins is shown for Re=380 in Fig. 4.8b. At Re=460 (not shown) no vortex shedding is observed. However, as shown in Fig. 4.8c, by Re=550 a secondary structure appears to periodically form and convect downstream from the leading edge of the fourth and subsequent rows. Although periodic, these flow structures, presumed to be vortices, are small, and a distinct structure is difficult to discern form the flow visualization results. Fig. 4.8d shows that at Re=550 the vortices are stretched and appear nearly flat at the exit of the

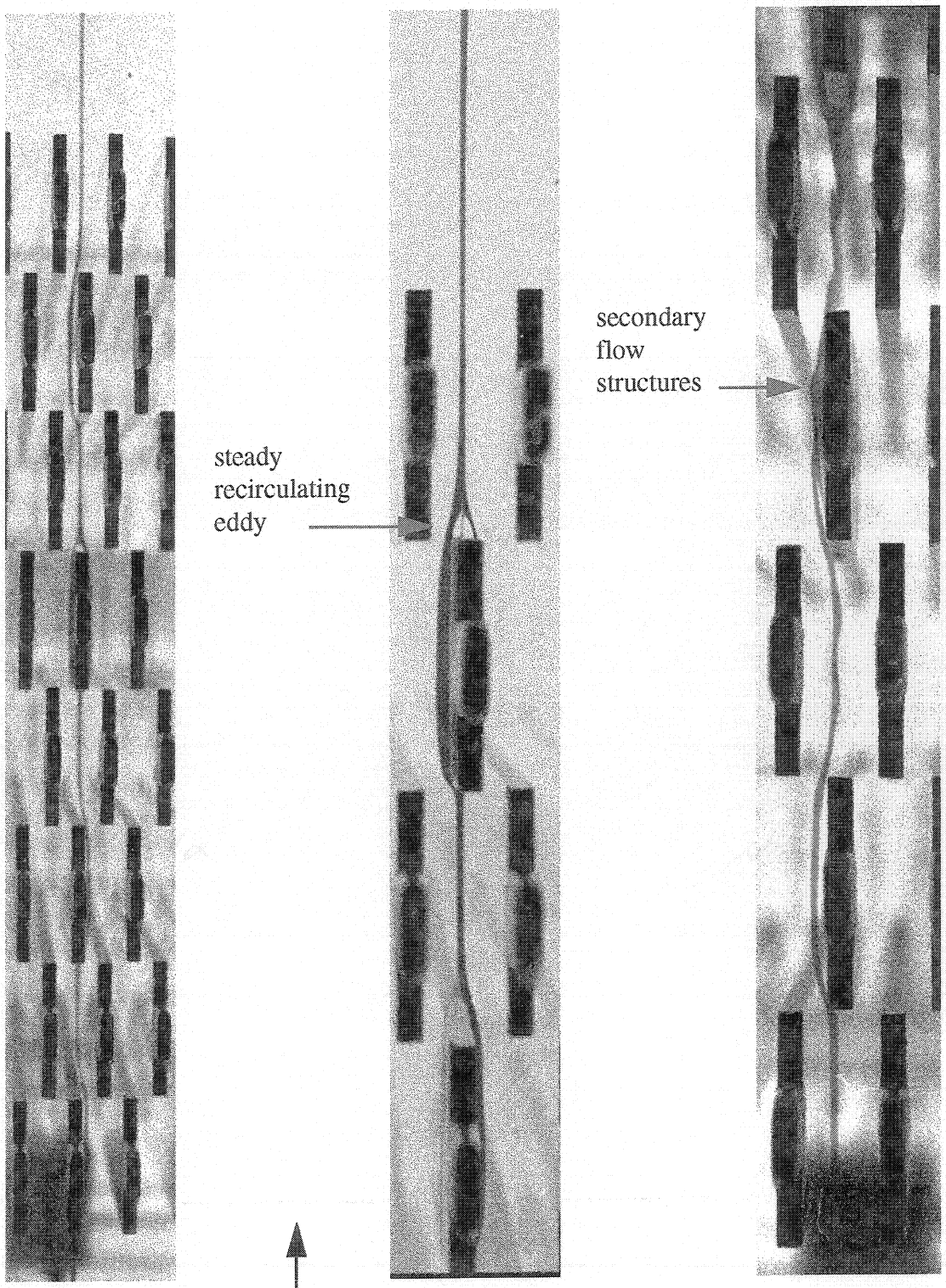

(Figure caption p. 43.)

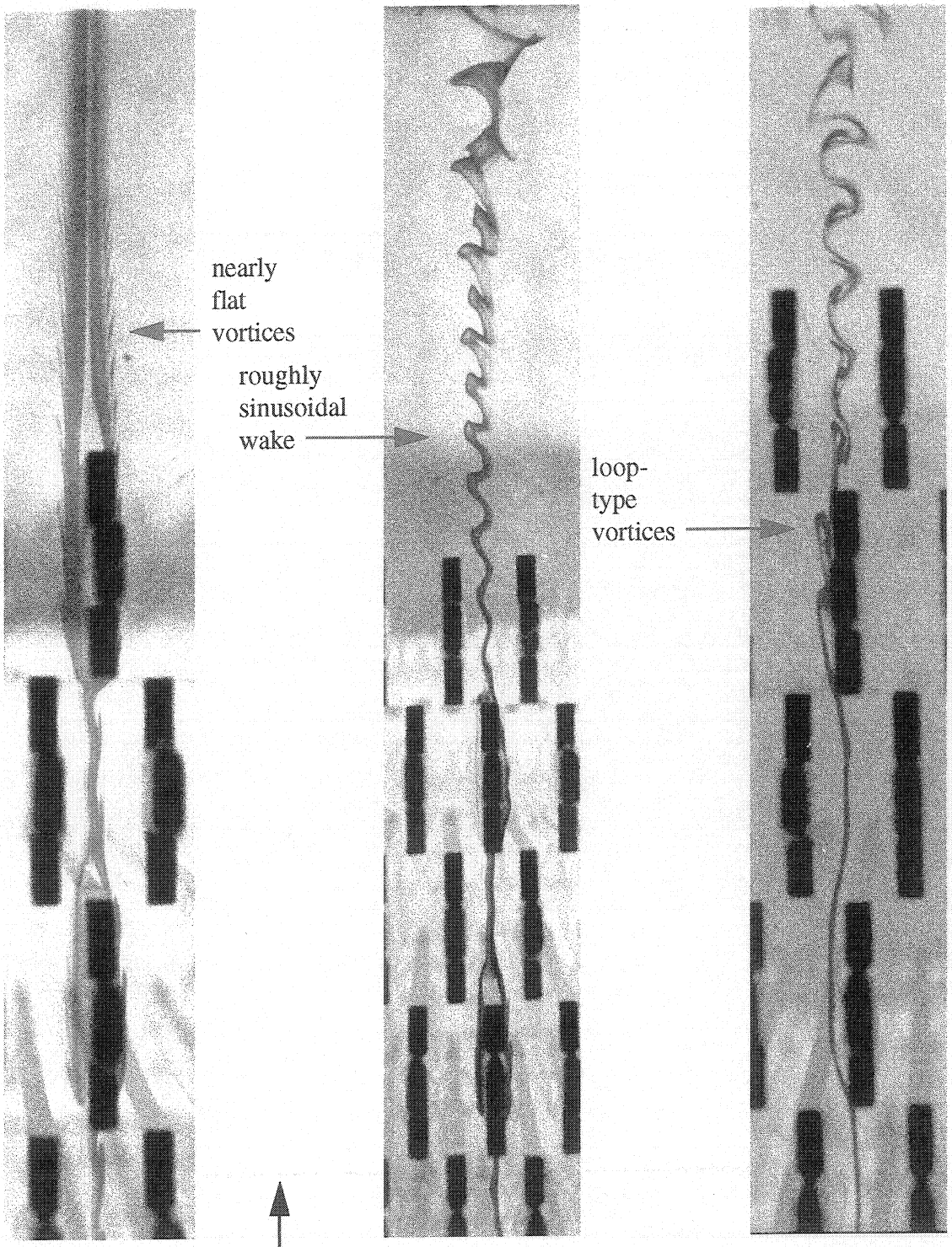

(d) (e) (f)

(Figure caption p. 43.)

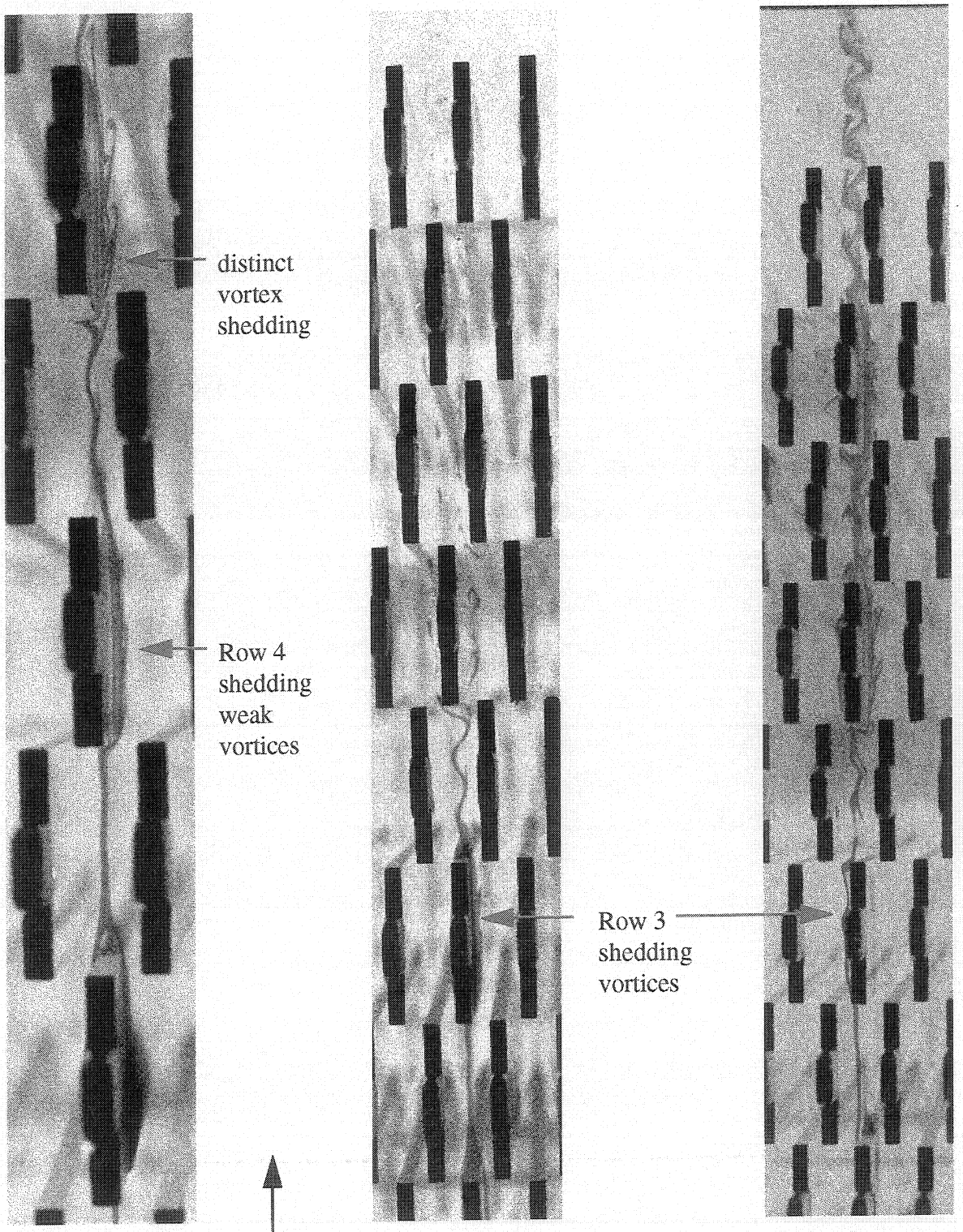

(Figure caption p. 43.)

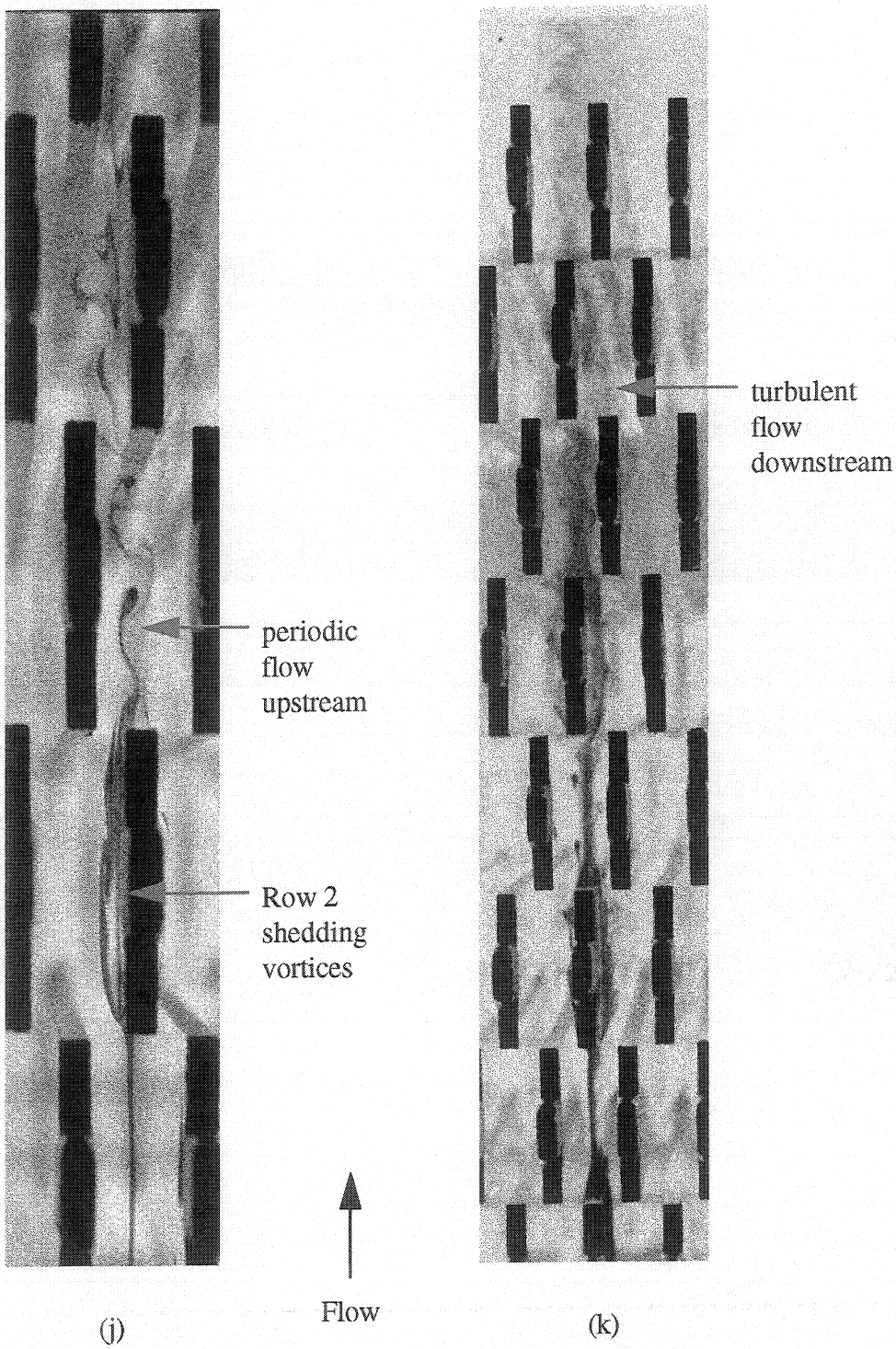

Fig. 4.8 - Water tunnel flow visualization (a) Re=380, Rows 1-8; (b) Re=380, Rows 5-8; (c) Re=550, Rows 1-5; (d) Re=550, Rows 5-8; (e) Re=630, Rows 4-8; (f) Re=720, Rows 4-8; (g) Re=720, Rows 2-6; (h) Re=800, Rows 1-8; (i) Re=850, Rows 1-8; (j) Re=1060, Rows 1-4; (k) Re=1060, Rows 1-8

array. By Re=630, shown in Fig. 4.8e, the wake has become roughly sinusoidal in appearance although the form of the secondary structures is still not distinct. Fig. 4.8f reveals that by Re=720 the wake has taken on a more distinct, discrete structure. It clearly resembles a von Kármán vortex street. Note the loop-type vortices present on the second to last row of the array. The beginning of the array with Re=720 is pictured in Fig. 4.8g. The fourth row appears to be shedding vortices, and by the fifth and sixth rows shedding is obvious. At Re=800, shown in Fig. 4.8h, the onset of vortex shedding has moved up to the third row. This figure clearly illustrates the enhanced mixing associated with vortex shedding. Fig. 4.8i pictures the entire array at Re=850. Here the distinct structures of the vortices and the wake are evident. The periodic nature of the shedding is clear. The vortices are evenly spaced, and over time, vortices at a given location have the same structure. Fig. 4.8j shows that by Re=1060 the second row of fins is shedding vortices. In Fig. 4.8k it can be seen that the flow becomes turbulent later in the array at Re=1060, and the flow is well mixed.

Several observations can be made based on the flow visualization. At low Reynolds numbers the flow is laminar. As the Reynolds number is increased, fins downstream in the array begin to shed vortices. Vortex shedding moves upstream in the array as the Reynolds number is increased. Once the entire array is shedding, further increases in the Reynolds number can cause the flow to become turbulent. In the vortex shedding regime, the flow is definitely periodic. The vortices have constant spacing and structure. At lower Reynolds numbers the vortices appear nearly flat while at higher Reynolds numbers they have a distinct loop-type structure. In the laminar regime, a steady recirculating eddy is present behind each fin. At higher Reynolds numbers, this eddy is destroyed by vortex shedding.

The Reynolds numbers at which vortex shedding was first observed for different rows in the array are shown in Fig. 4.9. These Reynolds numbers were calculated using both flow visualization and mass transfer experiments. For both methods, the exact Reynolds number at which vortex shedding began was not determined. For each test group, data were collected at specific Reynolds numbers. The data presented in the figure show the first Reynolds number for

a test group at which vortex shedding was observed. Two points are listed for the mass transfer experiments for row 4 since it was unclear if vortex shedding had indeed begun by Re=558. By Re=773 shedding was obvious according to this method. Mochizuki and Yagi [14] observed that at low Reynolds numbers, a small change in the Reynolds number can cause a large change in the location of vortex shedding in an array. Since data were taken only at specific Reynolds numbers, this phenomenon may be why the presence of vortex shedding in only the very last rows of the array was never observed.

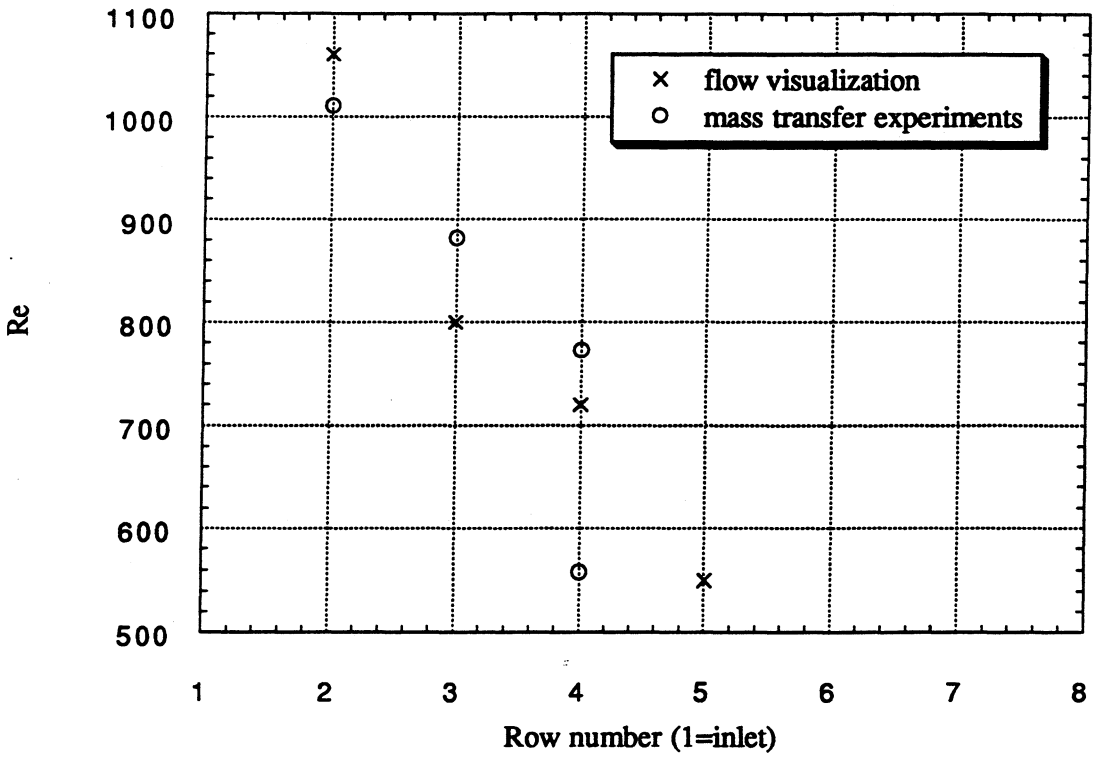

Fig. 4.9 - Reynolds number at which vortex shedding is evident for a given row in the array from the flow visualization and mass transfer experiments

The Strouhal number was calculated by measuring the distance between the vortices in the photographs. Fage and Johansen [37] used a hot-wire anemometer to report the speed of vortices relative to the speed of the fluid for a plate placed at angles of attack to the flow of 30° to 90°. Extrapolating these values down to 0° leads to a ratio of vortex velocity to fluid velocity of approximately 0.92. This value, along with U_C, was used to calculate the vortex shedding frequency and the Strouhal number. Accuracy is estimated to be +/-15%. These values are

plotted in Fig. 4.10 along with data from Xi *et al.* [21]. Their data were calculated for a geometry with t/L=0.128 and S/L=0.3 where S is one half of the fin pitch. In comparison, this experiment's geometry had t/L=0.125 and S/L=0.25. Differences between these two data sets are within the limits of the uncertainty. The Reynolds numbers in this plot are based on fin thickness.

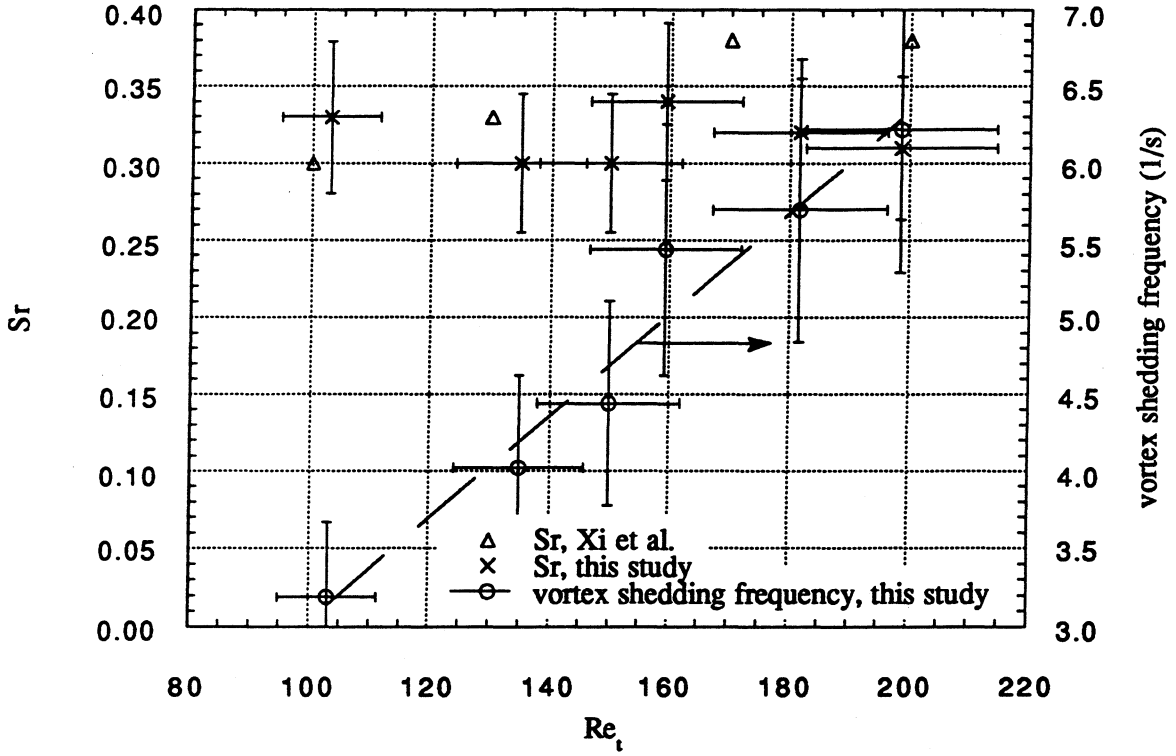

Fig. 4.10 - Estimated Strouhal number and vortex shedding frequency vs. Reynolds number based on flow visualization experiments and data from Xi *et al.* [21]

4.1.4 Effect of Turbulence Intensity on Mass Transfer

During collection of mass transfer data for the sparse offset strip geometry, an unexpected pattern arose. Data at low Reynolds numbers were taken using Orifice Plate 1, which has a bore diameter of 36.83 mm. At Re≈1200, Orifice Plate 2, with a bore diameter of 55.88 mm, was inserted. Fig. 4.11 illustrates that at Re≈1200, the Sherwood numbers measured when Orifice Plate 1 were used were almost 40% higher than those calculated when Orifice Plate 2 was used. At a given Reynolds number, the data should be the same regardless of which orifice plate is present. To explore the cause of this aberration, first the data reduction calculations were

checked. Second, the performance of the orifice plates was verified using both a pitot tube and a large bag. The time required to fill a large bag of known volume was measured. Both of these methods resulted in mass flow rates within 2% of those calculated using the orifice plates.

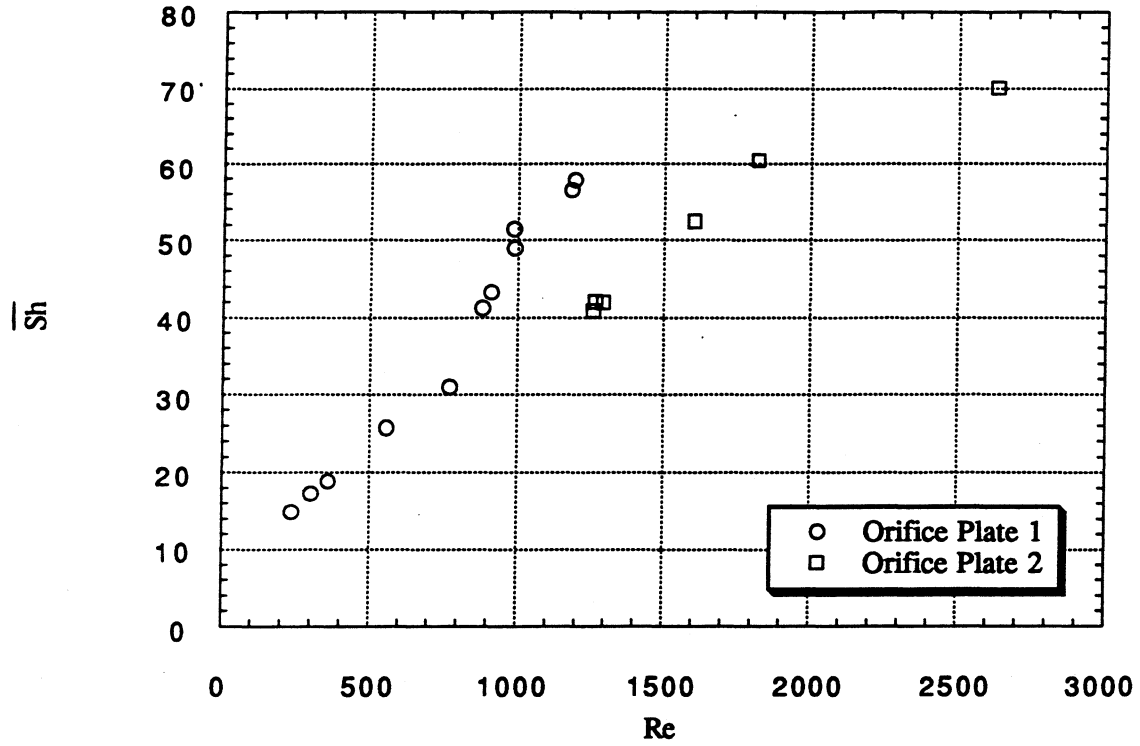

Fig. 4.11 - Data taken using two different orifice plates before flow straighteners were placed downstream of the test section

Finally, a flow conditioning section consisting of flow straighteners was placed downstream of the test section. When these flow straighteners were inserted, the data for Orifice Plate 1 fell into line with the data for Orifice Plate 2 (as shown in Fig. 4.1). An attempt to understand this behavior was undertaken by inserting a microphone into the test section and analyzing the frequency content of the flow under different conditions. However, due to the noise from the tunnel motor, it was not possible to determine the vortex shedding frequency or the effect of the fan on this frequency using this method. The reader is directed to Appendix E for a discussion of this investigation. A reason for this behavior has still not been determined. The vortex shedding frequency, calculated from the flow visualization experiments, was approximately 10 times less than the fan blade passing frequency. The blade passing frequency was found by aiming a strobe

at the fan blade and adjusting the frequency of the strobe until it appeared that the fan was standing still.

The aberrations in the data occurred when high turbulence intensities were present in the wind tunnel. Fig 2.3 shows that these high turbulence intensities were present at high motor frequencies -- and hence high Reynolds numbers -- when Orifice Plates 1 or 2 were used. The cause of these high intensities is not known. To take repeatable data, unaffected by these outside frequencies, data were recorded with flow straighteners placed downstream of the test section and using orifice plate and Reynolds number combinations that kept the turbulence intensity below 3% for this first geometry studied and below 2% for all subsequent geometries. When these precautions were taken, data for a given Reynolds number were independent of the orifice plate used.

4.2 Offset Strip Geometry, d_h = 36.9 mm

The experimental data for the sparse offset strip geometry are shown in Figs. 4.12, 4.13, 4.14, and 4.15. Fig. 4.12 includes mass transfer data for the dense and sparse offset strip geometries. As expected, at low Reynolds numbers data for the two geometries are similar. Kurosaki *et al.* [20] found that streamwise spacing has a much greater effect on heat transfer than does the fin pitch, and the streamwise spacing for these two geometries is the same. The data for the dense geometry fall slightly above those for the sparser geometry, perhaps because the flow accelerates more as it passes through the denser array. At higher Reynolds numbers, above approximately Re=800, the denser array performs significantly better. This improvement may be due to the fact that flow through the denser array makes the transition to periodic flow earlier. In addition, for the sparser array only one side of the fin is in close proximity to another fin. The other side is exposed essentially to a freestream. Vortex shedding would augment heat transfer less on this exposed side. The difference between the Sherwood numbers for the two geometries indicates a dependence on another geometrical factor in addition to hydraulic diameter. The correlations shown in Fig. 4.13 take fin height, pitch, length, and thickness into account in addition to

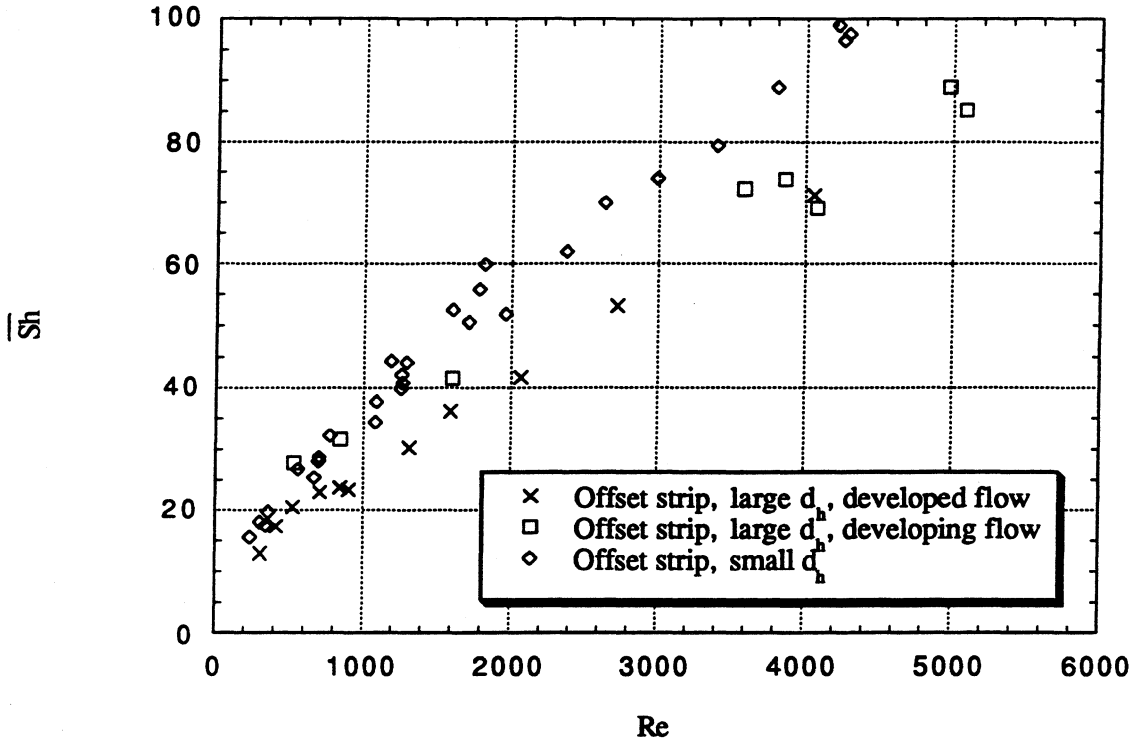

Fig. 4.12 - Average Sherwood numbers in Row 7 for developing and developed flow for the two offset strip geometries

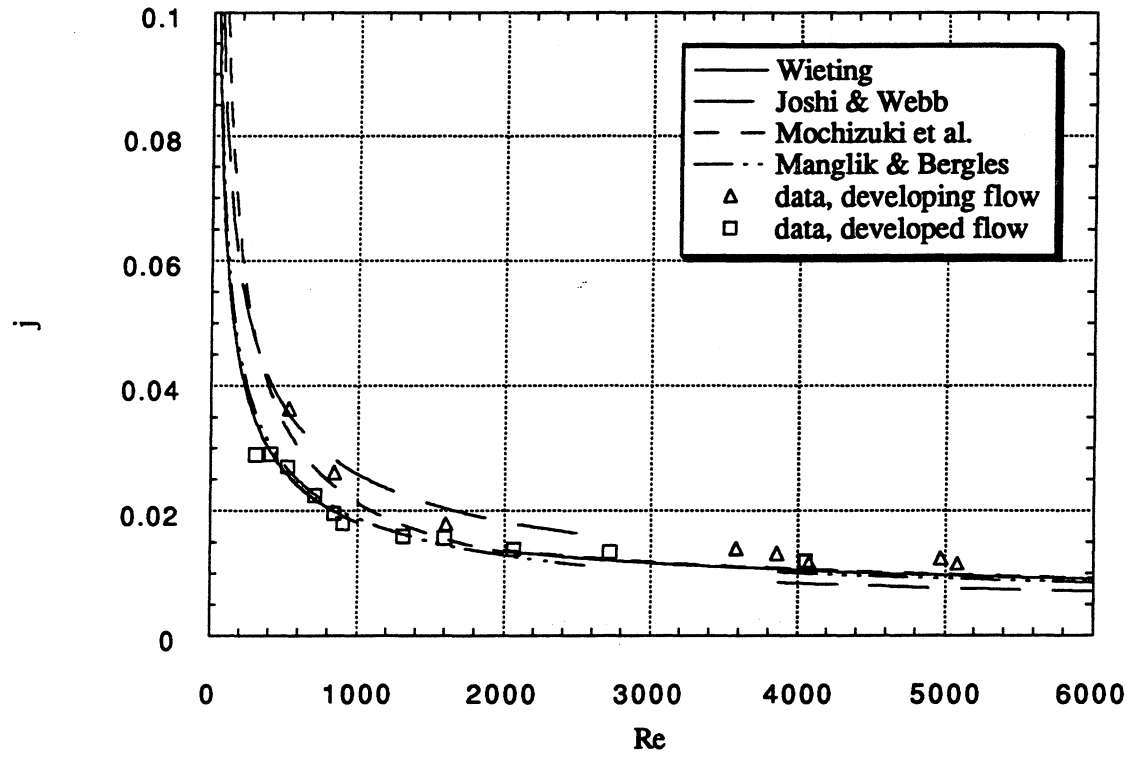

Fig. 4.13 - Colburn j factors for thermally developing and developed flow for the offset strip geometry with d_h=36.9 mm

hydraulic diameter.

An examination of Figs. 4.6 and 4.13 shows that at low Reynolds numbers, the differences between the Colburn j factors for developing and developed flow conditions are larger for sparse geometry than for the more dense geometry, and this effect continues to a higher Reynolds number. This effect may once again be due to the reduced mixing which takes place in the sparse geometry. The upstream boundary layers are likely to be more intact when they reach the downstream fins, causing lower heat transfer. These data show that the flow remains laminar above a Reynolds number of 1000, while for the more dense geometry all rows of the array were shedding by that Reynolds number.

Fig. 4.14, which is a plot of Sherwood numbers at given Reynolds numbers as a function of position in the array, corroborates these conclusions. It shows that there is no shedding effect at Re=2814. By Re=4169, all rows in the array may be shedding. However, this conclusion is based on the dramatic jump in Sherwood number from Row 1 to Row 2 and should be validated with additional data to ensure that the data point for Row 1 was not corrupted. This conclusion is in agreement with Xi and coworkers [21], who found that the flow becomes more unstable as the fin pitch decreases. By comparing Fig. 4.14 with Fig. 4.5, one can see that upstream louvers have a larger hand in decreasing the heat transfer from downstream louvers for the geometry with the larger hydraulic diameter.

The data for this geometry show better agreement with the correlations for offset strip fins than do the data for the more dense geometry. This agreement may be due to the larger fin pitch/length and pitch/width ratios which are closer to the geometrical parameters of the heat exchangers used to develop the correlations. The j factors taken under developed flow conditions fall closely in line with the correlations of Wieting and Manglik and Bergles while the data taken under developing flow conditions follow the correlation of Mochizuki. The experimental friction factors shown in Fig. 4.15 are underpredicted by three of the correlations once again, but they correspond closely with Wieting's correlation for the turbulent regime.

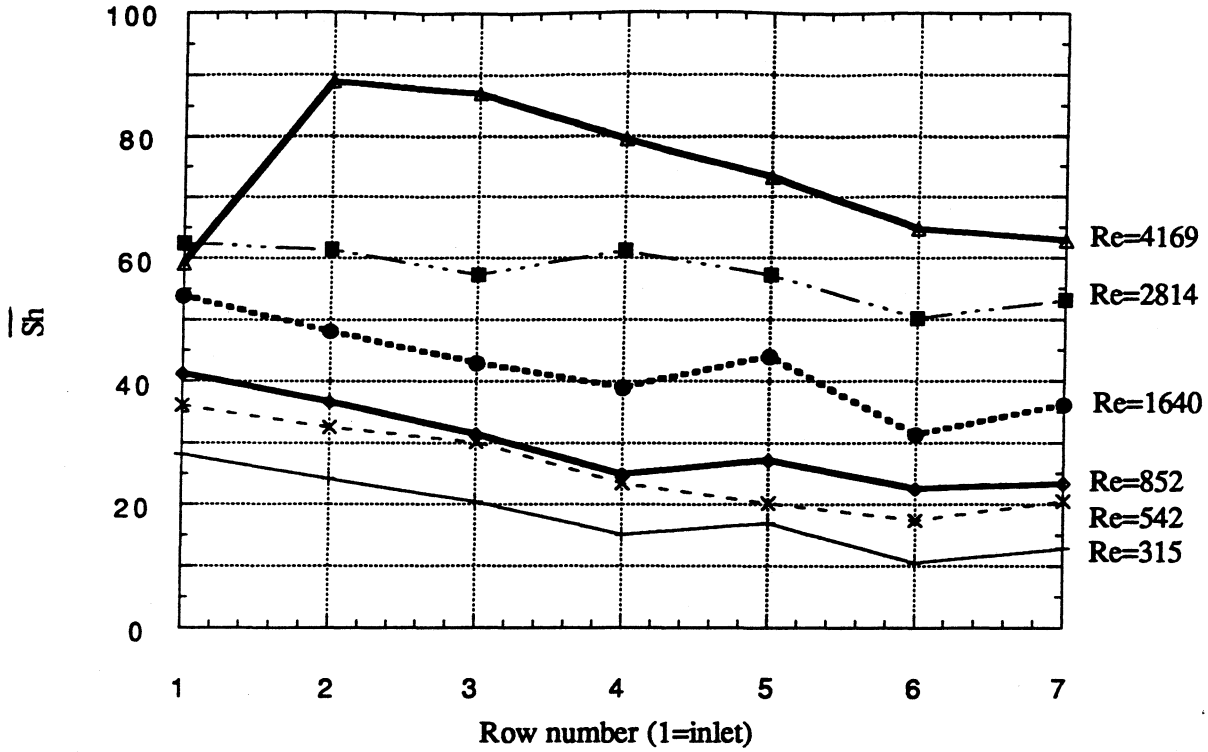

Fig. 4.14 - Average Sherwood numbers for succeeding rows in the array for the offset strip geometry with d_h=36.9 mm

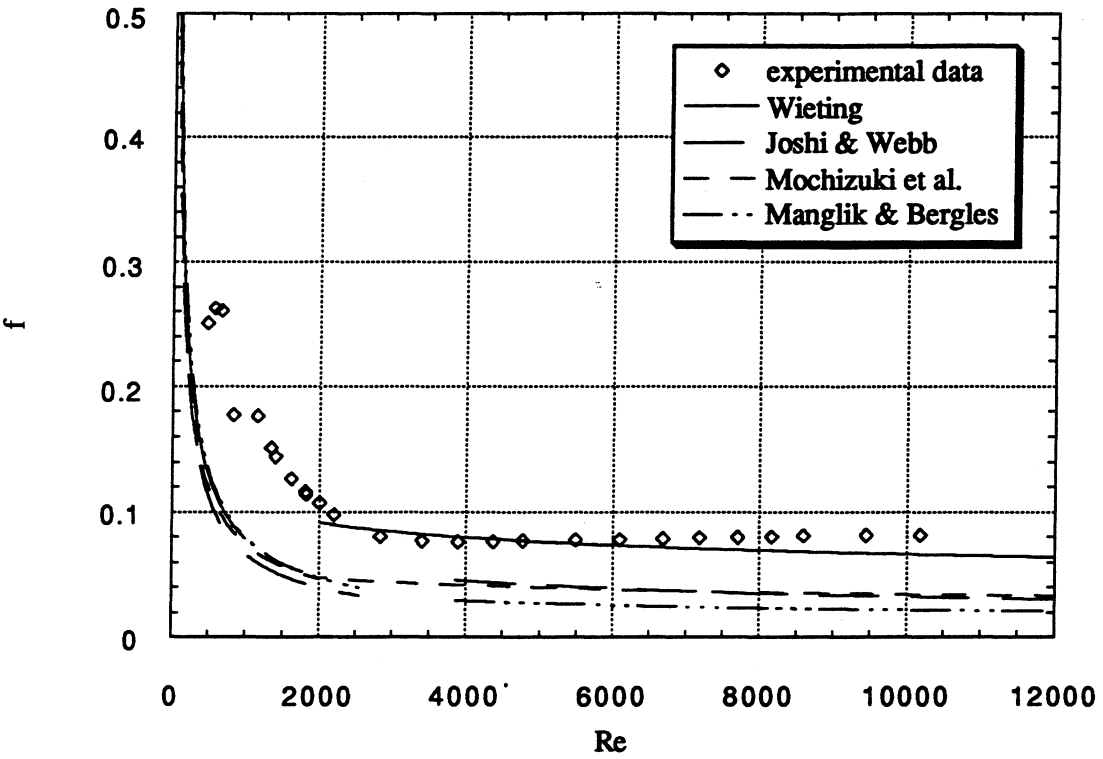

Fig. 4.15 - Friction factors for the offset strip geometry with d_h=36.9 mm. Correlations from the literature are for similar geometries.

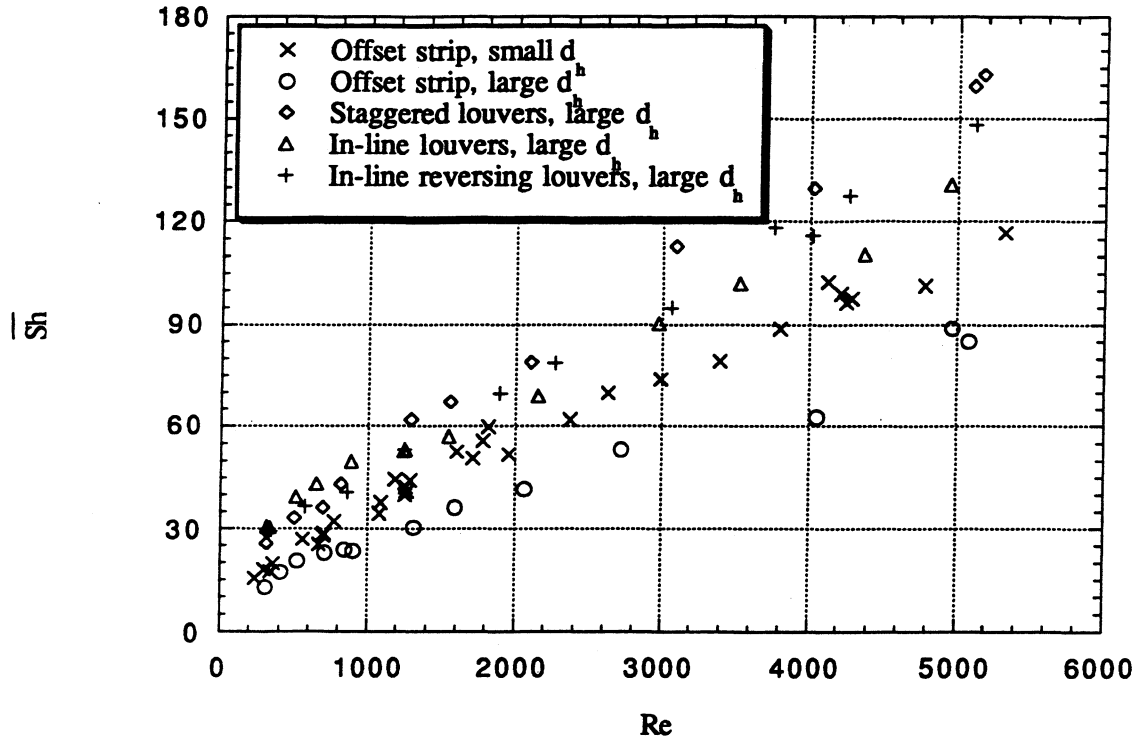

Fig. 4.16 - Average Sherwood numbers for the last row of array for all five geometries

4.3 Comparison of Offset Strip and Louvered-Fin Geometries

The experimental results for the five geometries studied are presented in Figs. 4.16-4.22. Fig. 4.16 shows that the louvered geometries resulted in consistently higher heat transfer than the offset strip geometries. This outcome is to be expected. A non-zero angle of incidence increases mixing, which in turn increases heat transfer. Among the three louvered geometries, the staggered geometry results in the highest heat transfer. For the in-line geometries, some of the flow may pass between the rows of fins like channel flow. When the rows of fins are staggered, this type of flow is prevented. The data shown in Fig. 4.16 were taken in the eighth row of the array. The Sherwood numbers for this row were similar for the two in-line louvered geometries. The average heat transfer for the eight rows of the in-line reversing array would probably be slightly less than for the in-line array. The angle of attack of the fourth row in the reversing array

is zero, so this row would cause less mixing and lower heat transfer. By the time the flow has reached the eighth row, though, this effect has been overcome, so the Sherwood numbers in the eighth row are similar for the two geometries.

Fig. 4.17 shows a comparison between the experimental data for the in-line louvered geometry and Zhang and Lang's correlation [27] for a similar geometry.

$$\overline{Sh} = 0.569\left(\frac{\theta\pi}{180}\right)^{0.543}\left(\frac{L}{p}\right)^{0.7} \mathrm{Re}_L^{0.7} \qquad [4.1]$$

$0.75 \le L/p \le 1.25$, $t/p = 1/20$, $10^\circ \le \theta \le 35^\circ$

For this experimental study, values of L/p=1.00 and $\theta=25^\circ$ were used. However, a larger value of t/p, 1/8, was used in this study. This Sherwood number was easily converted to the modified Colburn j factor shown in the plot. Although the correlation falls slightly below the experimental data, the correlation and the data follow the same trend. The difference may be due to several factors. First, thicker fins, such as those used in this study, may increase heat transfer [3]. Second, the current study used longer fins and more columns of fins which may have reduced end effects.

Local mass transfer data, shown in Fig. 4.18, were taken to examine the flow structures responsible for heat transfer enhancement. Since these results are time-averaged over the course of a test, it is difficult to discern the effects of vortex shedding in this plot. As discussed earlier, the low Reynolds number case for the dense offset strip geometry shows evidence of boundary layer growth, and the high Reynolds number case shows evidence of flow separation and reattachment before the boundary layer begins to grow. For the in-line louvered geometry, boundary layer growth is only visible on the second half of the fin. The high Sherwood numbers over the first half of the fin may be due to a combination of vortex shedding, mixing, and flow impinging on the louver. This plot reveals that short fins may be especially desirable when the fins have a non-zero angle of attack.

The friction factors shown in Fig. 4.19 corroborate the conclusions drawn from the Sherwood number data. The friction factors for the louvered geometries are higher than for the offset strip

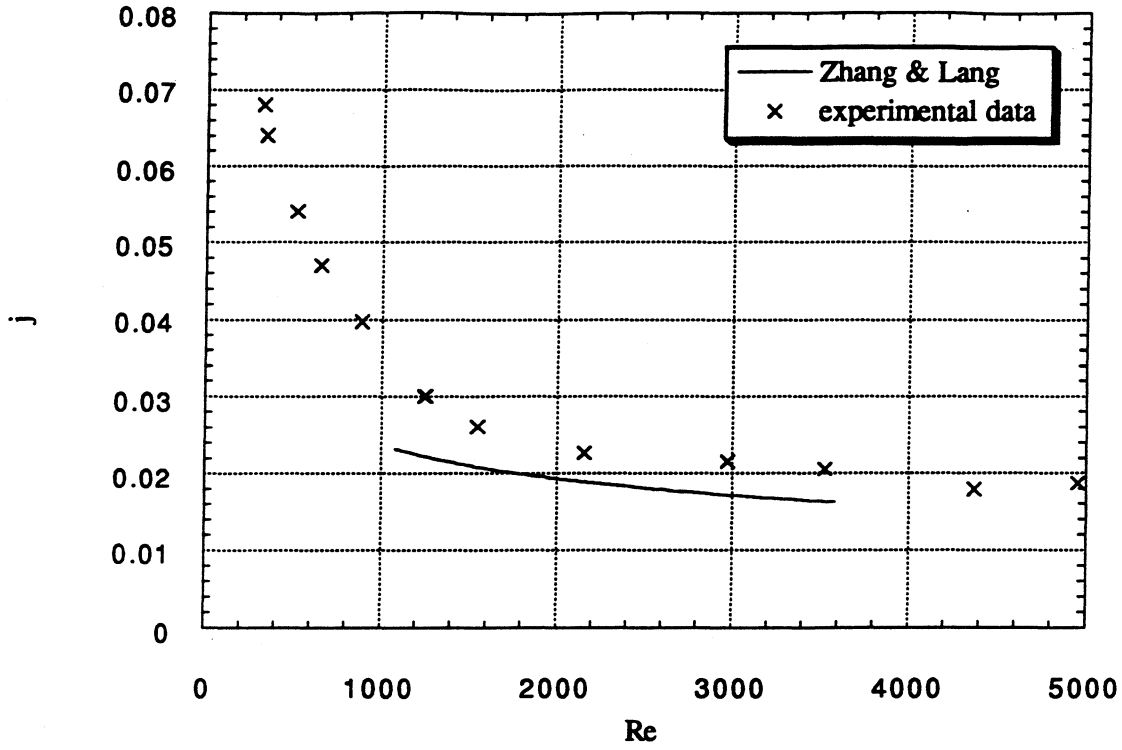

Fig. 4.17 - Modified Colburn j factors for the in-line louvered geometry

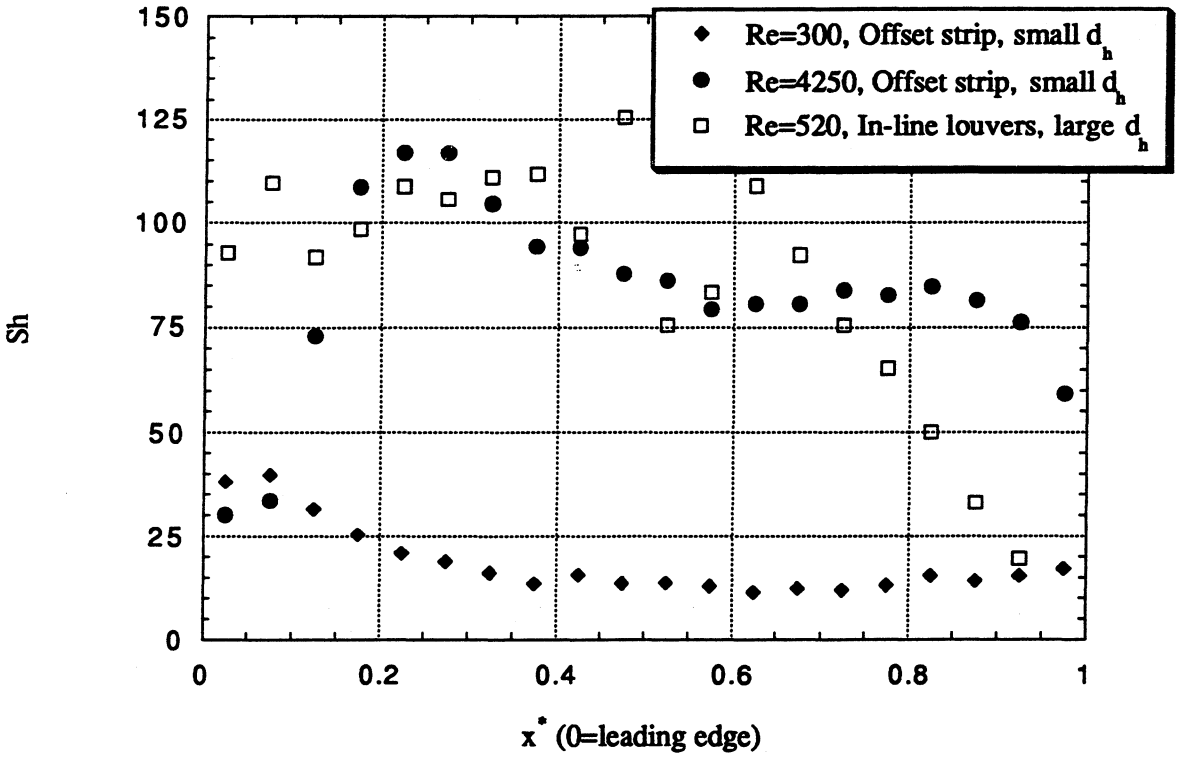

Fig. 4.18 - Local Sherwood numbers along the length of one fin, offset strip and louvered geometries

geometries. At very low Reynolds numbers, the friction factor behavior for the three louvered geometries is nearly identical. Any differences are within the uncertainty of the data since this uncertainty is large at low Reynolds numbers. For higher Reynolds numbers, the staggered louvered geometry results in the highest friction factors. Flow through the in-line reversing array experiences a 25% smaller pressure drop than flow through the in-line array. This smaller pressure drop is due to the fact that the angle of attack of the fins of the fourth row in the reversing array is zero, thus causing less form drag. Since only one row of fins is changed, a smaller difference between the friction factors of the two geometries was expected. However, this one row of fins can effect flow for several rows downstream.

The transition between flow regimes can be inferred from Fig. 4.20, a log plot of the friction factor data. It is clear that flow through each geometry experiences a similar type of transition. At lower Reynolds numbers, the data follow a negatively sloped line while at higher Reynolds numbers the data form a horizontal line. At high Reynolds numbers, the contribution of friction to the total pressure drop becomes small. Form drag causes the largest proportion of the pressure drop, so the friction factor becomes a constant. Joshi and Webb [19] reported similar trends.

The transition between the laminar and turbulent regimes is smooth. As noted by Joshi and Webb [19], the changes in slope of the data should correspond to changes in the flow regime. The first regime should correspond to the laminar regime and the second to the turbulent regime. Between these two regimes, where the slope of the data is changing, is the range of Reynolds numbers where periodic flow is present. A Reynolds number corresponding to the middle of this transitional regime was found by drawing lines tangent to the data in both the laminar and turbulent regimes and noting where they crossed. The periodic regime is assumed to center approximately around this point. Table 4.1 gives these values for the five geometries. As determined through the mass transfer experiments, transition occurs at a lower Reynolds number for dense offset strip array than for the sparse offset strip array. According to the mass transfer and flow visualization experiments, the flow is periodic through a range of approximately $500<Re<1000$ for the dense array. According to the friction factor data, the periodic regime

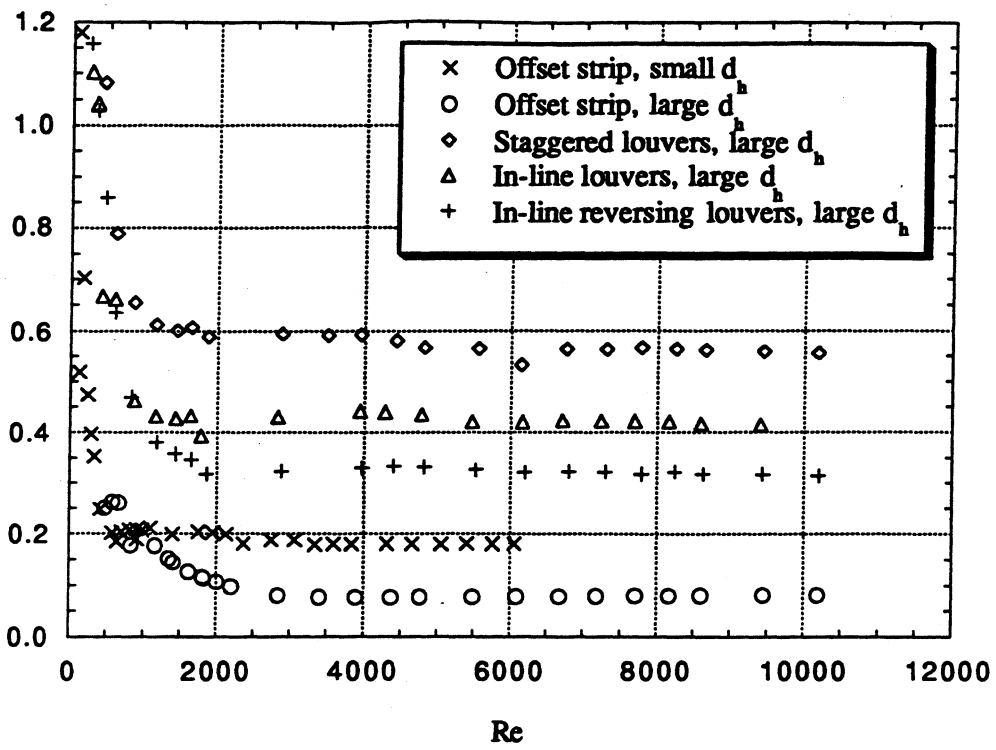

Fig. 4.19 - Friction factors for the five geometries studied

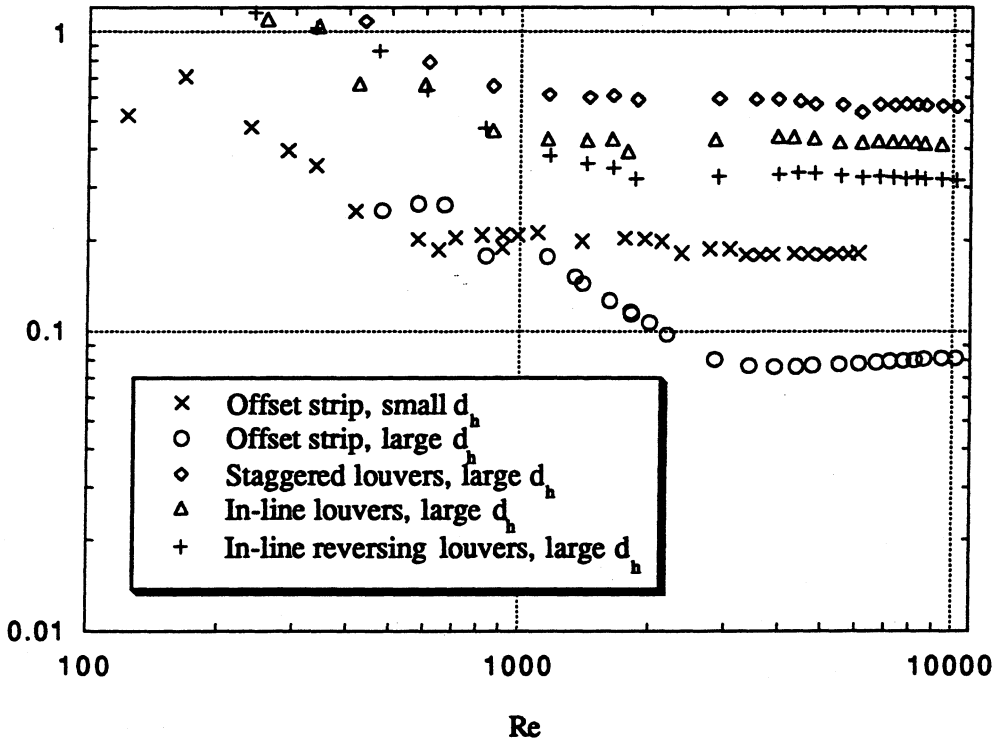

Fig. 4.20 - Log plot of friction factors for the five geometries studied

centers around a Reynolds number of 600 to 700. For the sparse array, it was hypothesized that transition occurred between a Reynolds number of 2800 and 4200. This conclusion is also supported by the friction factor data. In addition, Table 4.1 shows that the flow experiences transition earlier for the louvered geometries than for the sparse offset strip array which has the same hydraulic diameter. This trend is expected since the louvered geometries cause more mixing and more unstable flow which cause the flow to make the transition to turbulence at a lower Reynolds number than for the more stable offset strip geometry.

Table 4.1 - Reynolds numbers corresponding to the center of the periodic flow regime

Geometry	Reynolds Number of Mid-Point of Periodic Regime
Offset strip, small d_h	600-700
Offset strip, large d_h	3000
Staggered louvers, large d_h	800-900
In-line louvers, large d_h	800-1000
In-line reversing louvers, large d_h	1000-2000

Figs. 4.21 and 4.22 show two different ways to evaluate the five geometries. For each of these plots, the modified Colburn j factors are based on correlations of the data. The equations for the j factor shown below correlate 90% of the data within ±10%. Because of the high uncertainty in the correlations for friction factor at low Reynolds numbers, friction factor data points were used to generate Figs. 4.21 and 4.22 instead of the correlations.

Offset strip, small d_h:

$$j = 0.196\,\mathrm{Re}^{-0.230} \qquad [4.2a]$$

$$f = 37.9\,\mathrm{Re}^{-0.814} \qquad 85<\mathrm{Re}<415 \qquad [4.2b]$$

$$f = 0.199 - 3.63\cdot 10^{-6}\,\mathrm{Re} \qquad 550<\mathrm{Re}<6050 \qquad [4.2c]$$

Offset strip, large d_h:

$$j = 0.315\,\mathrm{Re}^{-0.407} \qquad [4.3a]$$

$$f = 20.1\,\mathrm{Re}^{-0.687} \qquad 450<\mathrm{Re}<2850 \qquad [4.3b]$$

$$f = 0.0730 + 8.46\cdot 10^{-7}\,\mathrm{Re} \qquad 3400<\mathrm{Re}<10150 \qquad [4.3c]$$

Staggered louvers, large d_h:	$j = 0.399\,\mathrm{Re}^{-0.351}$		[4.4a]
	$f = 412\,\mathrm{Re}^{-0.964}$	350<Re<850	[4.4b]
	$f = 0.607 - 5.99 \cdot 10^{-6}\,\mathrm{Re}$	1150<Re<10200	[4.4c]
In-line louvers, large d_h:	$j = 1.13\,\mathrm{Re}^{-0.496}$		[4.5a]
	$f = 62.7\,\mathrm{Re}^{-0.724}$	250<Re<850	[4.5b]
	$f = 0.429 - 9.30 \cdot 10^{-7}\,\mathrm{Re}$	1150<Re<9400	[4.5c]
In-line reversing louvers, large d_h:	$j = 0.504\,\mathrm{Re}^{-0.385}$		[4.6a]
	$f = 56.2\,\mathrm{Re}^{-0.697}$	250<Re<1450	[4.6b]
	$f = 0.331 - 1.30 \cdot 10^{-6}\,\mathrm{Re}$	1850<Re<10200	[4.6c]

Fig. 4.21 is a plot of j/f versus Reynolds number. This performance criterion is often used since higher values of j/f indicate that a smaller frontal area is required for a heat exchanger if heat transfer and pressure drop are fixed. Although Cowell pointed out that a comparison of $\sigma^2 j/f$ may be more accurate [38], j/f is employed here because of its widespread use. The dense offset strip geometry is included on the graph in order to show the behavior of j/f with changing Reynolds number; the data should not be compared with the data for the other four geometries since its hydraulic diameter is different. It must be noted that at Reynolds numbers above 1000, the average uncertainty in j/f is ±13%. Below a Reynolds number of 1000 those uncertainties are larger due to the large uncertainty in f at low Reynolds numbers. Despite those uncertainties, each geometry appears to have an optimum operating point. Similar trends were reported by Manglik and Bergles [22]. According to this analysis, the sparse offset strip geometry requires a smaller frontal area than the louvered geometries. The less dense geometries appear to be more efficient at the higher Reynolds numbers, while the more dense offset strip array is more efficient at lower Reynolds numbers.

Fig. 4.22 is a plot of j versus pumping power. This plot, which indicates the relative operating cost for the five geometries, shows the resulting heat transfer for each of the geometries when air is pumped through the array at a given pumping power. No optimum

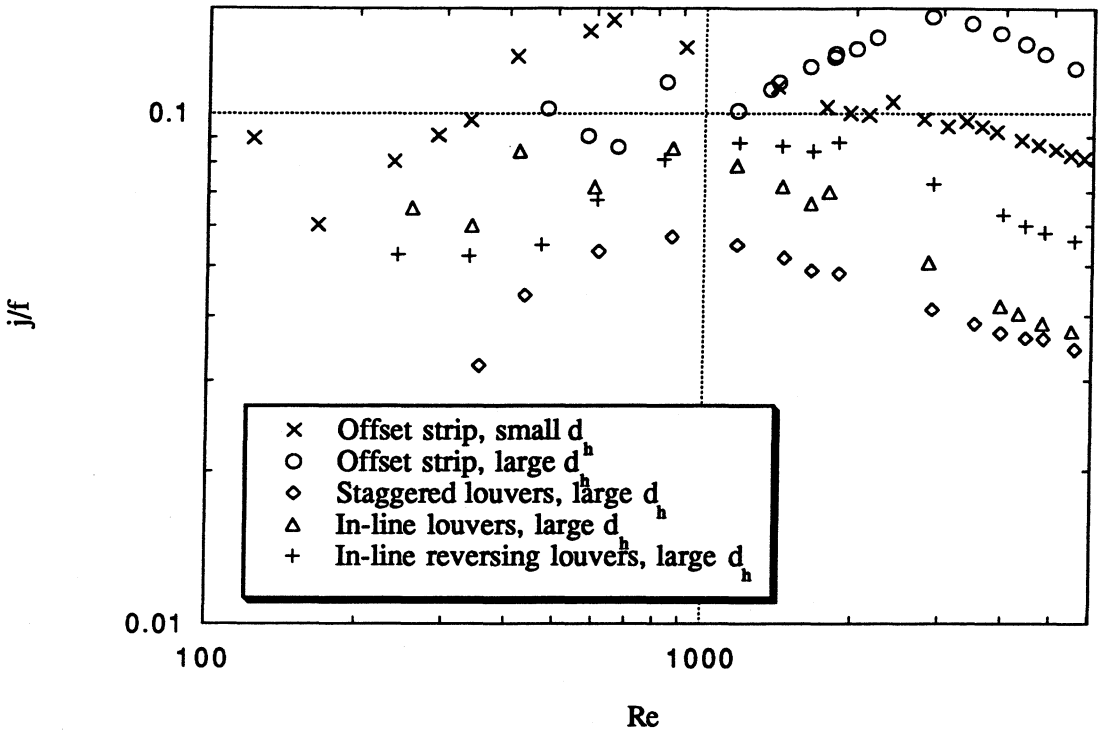

Fig. 4.21 - Log plot of London area-goodness factor, j/f, for the five geometries studied

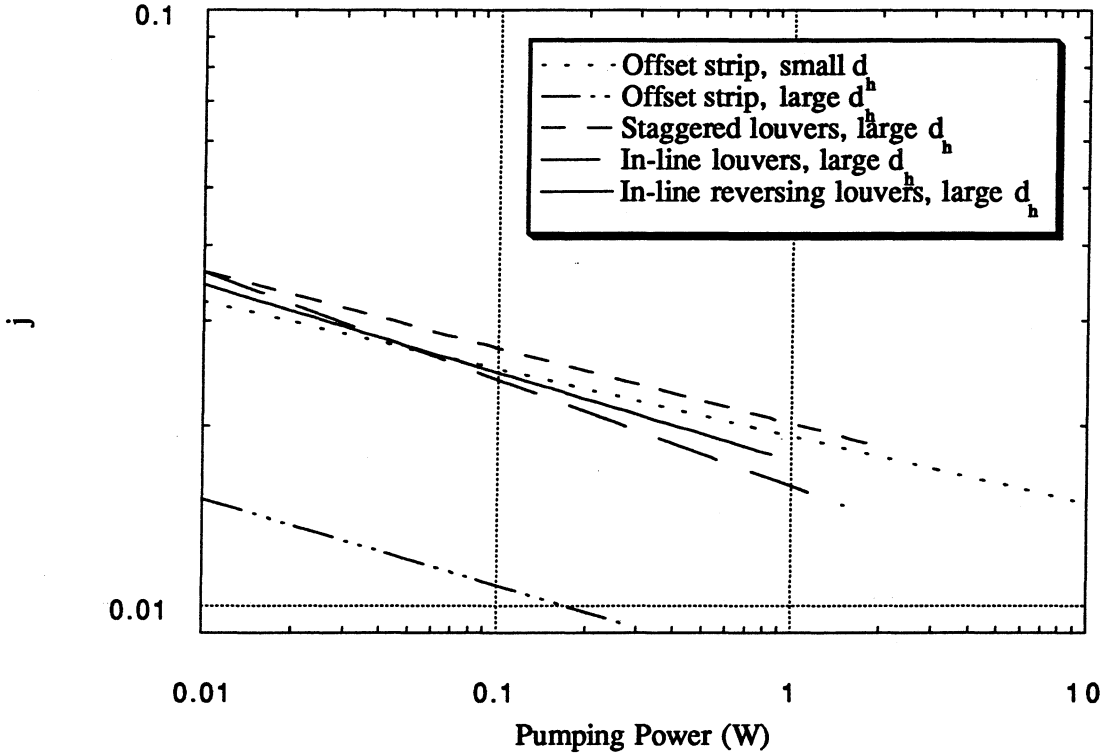

Fig. 4.22 - Log plot of modified Colburn j factor vs. pumping power

operating point is apparent in this plot. It is interesting to note that the sparse offset strip array appears to be the least efficient. The flow through that geometry is much more stable than the flow through any of the other geometries. The performances of each of the four less stable geometries are similar. This observation is significant. Despite the fact that the sparse offset strip and the louvered geometries have the same hydraulic diameter, it is the more dense offset strip array which has performance similar to the louvered geometries. It is apparent that for this situation, packing the offset strip fins more closely has a similar effect to giving the fins a non-zero angle of attack. The analysis of the local heat transfer coefficient of the fins revealed that local heat transfer behavior for offset strip and louvered fins are different, but at a given pumping power, the average heat transfer through louvered and offset strip arrays can be the same for certain geometries.

CHAPTER 5 - CONCLUSIONS AND FUTURE WORK

5.1 Conclusions

Through this project, a better understanding of the basic flow and heat transfer mechanisms has been developed. This understanding has been developed through the analysis of two offset strip and three louvered-fin geometries. The following conclusions may be drawn from the work presented here:

1) Vortex shedding occurs in both offset strip and louvered arrays. The presence of vortex shedding in the arrays studied was determined through four methods -- two involving the analysis of mass transfer data, one involving the analysis of friction factor data, and the last based on flow visualization. At low Reynolds numbers, the flow is steady and laminar. As the Reynolds number increases, fins downstream in the array begin to shed vortices. As the Reynolds increases further, vortex shedding moves upstream in the array until fins in the entire array are shedding. Further increases can cause the flow to become turbulent. The Reynolds number at which fins begin to shed vortices is dependent on the array geometry. A smaller transverse fin spacing and a non-zero fin angle of incidence both cause the flow to become unstable at lower Reynolds numbers.

2) Vortex shedding in the periodic flow regime increases heat transfer significantly. The contributions of boundary layer restarting and vortex shedding to heat transfer have been quantified under different operating conditions for the offset strip geometry. For example, for the dense offset strip array studied, boundary layer restarting caused the heat transfer to increase by 2.6 times over a continuous plate with no restarting. With a core air velocity of 1 m/s, vortex shedding increased the heat transfer coefficient an additional 30% over the interrupted plate solution without vortex shedding, and at 2 m/s it increased h 60%. Both boundary layer restarting and vortex shedding cause an additional pressure drop as well.

3) The local heat transfer behavior on a fin is different for offset strip and louvered fins. At low Reynolds numbers, fins with a zero degree angle of incidence show evidence of boundary layer growth. At higher Reynolds, the flow separates along the leading edge and reattaches before the boundary layer grows. For fins with a non-zero angle of attack, heat transfer is enhanced over the first section of the fin. This enhancement is probably due to a combination of vortex shedding, fluid mixing, and flow impinging on the fin. Heat transfer drops off farther downstream as the boundary layer begins to grow. Short louvered fins, therefore, may be advantageous.

4) Flow instability results in higher heat transfer and pressure drop. For a given fin spacing, louvered fins cause more mixing and hence more heat transfer and higher pressure drop than a parallel fin geometry. Flow through the offset strip array with parallel fins can provide similar results if the fin pitch is decreased, increasing flow instability. Note that decreasing the fin pitch will not always increase heat transfer. A point will be reached where decreasing the fin pitch will cause boundary layers from fins in the same row to interact and will cause the bulk temperature to increase to an extent that heat transfer will decrease. Based on the five geometries studied, it can be concluded that louvered-fin exchangers require a smaller volume for a given heat duty at a given Reynolds number than do offset strip exchangers. However, pumping power is significantly higher. Therefore, if the pumping power is unimportant and the exchanger size is to be minimized, louvered fins are suggested. However, if the overall heat exchanger efficiency is important, offset strip fins may be just as desirable if not more desirable than louvered fins.

5.2 Future Work

This experimental study has ignored many of the three-dimensional effects present in an actual heat exchanger. Throughout the following year, several of these three-dimensional aspects will be studied experimentally. Research on the effects of burrs, tubes, and chevron louvers on heat transfer and pressure drop will be conducted. In addition, flow visualization of

the louvered-fin geometry is underway in order to determine the actual flow mechanisms as work within the louvered-fin geometry. A numerical study, which this experimental work is verifying, is ongoing. The numerical code will be used to look for optimum heat exchanger geometries and will be used to develop concrete design guidelines. Finally, full-scale testing needs to be performed to compare these results to those in an actual heat exchanger which experiences such realities as frosting.

REFERENCES

[1] Admiraal, D.M. and Bullard, C.W., 1995, "Experimental Validation of Heat Exchanger Models for Refrigerator/Freezers," *ASHRAE Transactions,* Vol. 101, Part 1, pp. 34-43.

[2] Norris, R.H. and Spofford, W.A., 1942, "High-Performance Fins for Heat Transfer," *Transactions of ASME*, Vol. 64, pp. 489-496.

[3] Cur, N. and Sparrow, E.M., 1978, "Experiments on Heat Transfer and Pressure Drop for a Pair of Colinear, Interrupted Plates Aligned with the Flow," *Int. J. Heat Mass Transfer*, Vol. 21, pp. 1069-1079.

[4] Amon, C.H. and Mikic, B.B, 1989, "Spectral Element Simulations of Forced Convective Heat Transfer: Application to Supercritical Slotted Channel Flows," *National Heat Transfer Conference: Numerical Heat Transfer With Personal Computers and Supercomputing,* HTD-Vol. 110, pp. 175-183, ASME, New York.

[5] Amon, C.H., Majumdar, D., Herman, C.V., Mayinger, F., Mikic, B.B., and Sekulic, D.P., 1991, "Experimental and Numerical Investigation of Oscillatory Flow and Thermal Phenomena in Communicating Channels, " *Experimental/Numerical Heat Transfer in Combustion and Phase Change,* ASME HTD-Vol. 170, pp. 25-34.

[6] London, A.L. and Shah, R.K., 1968, "Offset Rectangular Plate-Fin Surfaces--Heat Transfer and Flow Friction Characteristics," *Journal of Engineering for Power, Trans. ASME,* Vol. 90, pp. 218-228.

[7] Wieting, A.R., 1975, "Empirical Correlations for Heat Transfer and Flow Friction Characteristics of Rectangular Offset-Fin Plate-Fin Heat Exchangers," *J. Heat Transfer,* Vol. 97, pp. 488-490.

[8] Sekulic, D.P., 1989, "Flow Through Communicating Channels Compact Heat Transfer Geometry," *International Communications on Heat and Mass Transfer*, Vol. 16, pp. 667-679.

[9] Manglik, R.M. and Bergles, A.E., 1990, "The Thermal-Hydraulic Design of the Rectangular Offset-Strip-Fin Compact Heat Exchanger," *Compact Heat Exchangers,* R.K. Shah, A.D. Kraus, and D. Metzger, ed., pp. 123-149, Hemisphere Publishing, New York.

[10] Sparrow, E.M., Baliga, B.R., and Patankar, S.V., 1977, "Heat Transfer and Fluid Flow Analysis of Interrupted-Wall Channels, with Application to Heat Exchangers," *J. Heat Transfer,* Vol. 99, pp. 4-11.

[11] Sparrow, E.M. and Liu, C.H., 1979, "Heat Transfer, Pressure Drop and Performance Relationships for In-Line, Staggered, and Continuous Plate Heat Exchangers," *Int. J. Heat Mass Transfer*, Vol. 22, pp. 1613-1624.

[12] Sparrow, E.M. and Hajiloo, A., 1980, "Measurements of Heat Transfer and Pressure Drop for an Array of Staggered Plates Aligned Parallel to an Air Flow," *J. Heat Transfer,* Vol. 102, pp. 426-432.

[13] Patankar, S.V. and Prakash, C., 1981, "An Analysis of the Effect of Plate Thickness on Laminar Flow and Heat Transfer in Interrupted-Plate Passages," *Int. J. Heat Mass Transfer*, Vol. 24, pp. 51-58.

[14] Mochizuki, S. and Yagi, Y., 1982, "Characteristics of Vortex Shedding in Plate Arrays," *Flow Visualization II*, W. Merzkirch, ed., pp. 99-103, Hemisphere Publishing, Washington, D.C.

[15] Mochizuki, S., Yagi, Y., and Yang, W., 1988, "Flow Pattern and Turbulence Intensity in Stacks of Interrupted Parallel-Plate Surfaces," *Exp. Thermal Fluid Sci.*, Vol. 1, pp. 51-57.

[16] Yang, W., 1983, "Forced Convective Heat Transfer in Interrupted Compact Surfaces," *Proceedings of the ASME/JSME Thermal Engineering Conference*, pp. 105-111, ASME, New York.

[17] Kays, W.M, and London, A.L., 1964, *Compact Heat Exchangers,* McGraw-Hill, New York.

[18] Mullisen, R.S. and Loehrke, R.I., 1986, "A Study of the Flow Mechanisms Responsible for Heat Transfer Enhancement in Interrupted-Plate Heat Exchangers," *J. Heat Transfer*, Vol. 108, pp. 377-385.

[19] Joshi, H.M. and Webb, R.L., 1987, "Heat Transfer and Friction in the Offset Strip-Fin Heat Exchanger," *Int. J. Heat Mass Transfer*, Vol. 30, pp. 69-83.

[20] Kurosaki, Y., Kashiwagi, T., Kobayashi, H., Uzuhashi, L., and Tang, S., 1988, "Experimental Study on Heat Transfer from Parallel Louvered Fins by Laser Holographic Interferometry," *Exp. Thermal Fluid Sci.*, Vol. 1, pp. 59-67.

[21] Xi, G., Futagami, S., Hagiwara, Y., and Suzuki, K., 1991, "Flow and Heat Transfer Characteristics of Offset-Fin Array in the Middle Reynolds Number Range," *ASME/JSME Thermal Engineering Proceedings*, Vol. 3, pp. 151-156, ASME, New York.

[22] Manglik, R.M. and Bergles, A.E., 1995, "Heat Transfer and Pressure Drop Correlations for the Rectangular Offset Strip Fin Compact Heat Exchanger," *Exp. Thermal Fluid Sci.*, Vol. 10, pp. 171-180.

[23] Davenport, C.J., 1983, "Correlations for Heat Transfer and Flow Friction Characteristics of Louvered Fin," *AIChE Symp. Ser. 225*, Vol. 79, pp. 19-27.

[24] Lee, Y.N., 1986, "Heat Transfer and Pressure Drop Characteristics of an Array of Plates Aligned at Angles to the Flow in a Rectangular Duct," *Int. J. Heat Mass Transfer*, Vol. 29, pp. 1553-1562.

[25] Aoki, H., Shinagawa, T., and Suga, K., 1989, "An Experimental Study of the Local Heat Transfer Characteristics in Automotive Louvered Fins," *Exp. Thermal Fluid Sci.*, Vol. 2, pp. 293-300.

[26] Suga, K. and Aoki, H., 1991, "Numerical Study on Heat Transfer and Pressure Drop on Multilouvered Fins," *ASME/JSME Thermal Engineering Proceedings*, Vol. 4, pp. 361-368, ASME, New York.

[27] Zhang, H. and Lang, X., 1989, "The Experimental Investigation of Oblique Angles and Interrupted Plate Lengths for Louvered Fins in Compact Heat Exchangers," *Exp. Thermal Fluid Sci.*, Vol. 2, pp. 100-106.

[28] Hiramatsu, M., Ishimaru, T., and Matsuzaki, K., 1990, "Research on Fins for Air Conditioning Heat Exchangers (1st Report, Numerical Analysis of Heat Transfer on Louvered Fins)," *JSME International Journal, Series II*, Vol. 33, No. 4, pp. 749-756.

[29] Webb, R.L. and Trauger, P., 1991, "Flow Structure in the Louvered Fin Heat Exchanger Geometry," *Exp. Thermal Fluid Sci.*, Vol. 4, pp. 205-217.

[30] Huang, H. and Tao, W., 1993, "An Experimental Study on Heat/Mass Transfer and Pressure Drop Characteristics for Arrays of Nonuniform Plate Length Positioned Obliquely to the Flow Direction," *J. Heat Transfer*, Vol. 115, pp. 568-575.

[31] Lue, S.S., Huang, H.Z., and Tao, W.Q, 1993, "Experimental Study on Heat Transfer and Pressure Drop Characteristics in the Developing Region for Arrays of Obliquely Positioned Plates of Nonuniform Length," *Exp. Thermal Fluid Sci.*, Vol. 7, pp. 30-38.

[32] Cowell, T.A., Heikal, M.R., and Achaichia, A., 1995, "Flow and Heat Transfer in Compact Louvered Fin Surfaces," *Exp. Thermal Fluid Sci.*, Vol. 10, pp. 192-199.

[33] "Measurement of Fluid Flow in Pipes Using Orifice, Nozzle, and Venturi," *ASME MFC-3M-1989*, The American Society of Mechanical Engineers, New York.

[34] Kearney, S., 1995, "Local and Average Heat Transfer and Pressure Drop Characteristics of Annularly Finned Tube Heat Exchangers," M.S. Thesis, University of Illinois at Urbana-Champaign, Urbana, Illinois.

[35] Jalkio, J.A., Kim, R.C., and Case, S.K., 1985, "Three Dimensional Inspection Using Multistripe Structured Light," *Optical Engineering*, Vol. 24, No. 6, pp. 966-974.

[36] Mochizuki, S., Yagi, Y., and Yang, W., 1987, "Transport Phenomena in Stacks of Interrupted Parallel-Plate Surfaces," *Experimental Heat Transfer*, Vol. 1, pp. 127-140.

[37] Fage, A. and Johansen, F.C., 1927, "On the Flow of Air behind an Inclined Flat Plate of Infinite Span," *Proc. Roy. Soc.*, Vol. 116, pp. 170-197.

[38] Cowell, T.A., 1990, "A General Method for the Comparison of Compact Heat Transfer Surfaces," *J. Heat Transfer*, Vol. 112, pp. 288-294.

[39] Bejan, A., 1995, *Convection Heat Transfer*, John Wiley & Sons, New York.

[40] Kays, W.M. and London, A.L., 1984, *Compact Heat Exchangers*, McGraw-Hill, New York.

[41] Mendes, P.R. Souza, 1991, "A Review of Mass Transfer Measurements Using the Naphthalene Sublimation Technique," *Exp. Thermal Fluid Sci.*, Vol. 4, pp. 510-523.

[42] Ambrose, D., Lawrenson, I.F., and Sprake, C.H.S., 1975, "The Vapor Pressure of Naphthalene," *Journal of Chemical Thermodynamics*, Vol. 7, pp. 1173-1175.

[43] Cho, K., Irvine, T.F., and Karni, J., 1992, "Measurement of the Diffusion Coefficient of Naphthalene into Air," *Int. J. Heat Mass Transfer*, Vol. 35, No. 4, pp. 957-966.

[44] Kudchadker, A.P., Kudchadker, S.A., and Wilhoit, R.C., 1978, "Naphthalene", American Petroleum Inst., Washington, D.C.

[45] Holman, J.P., 1990, *Heat Transfer*, McGraw-Hill, Inc., New York.

[46] Kline, S.J. and McClintock, F.A., 1953, "Describing Uncertainties in Single Sample Experiments," *Mechanical Engineering,* Vol. 75, pp. 3-8.

[47] Cochran, W.T., Cooley, J.W., Favin, D.L., Helms, H.D., Kaenel, R.A., Lang, W.W., Maling, G.C. Jr., Nelson, D.E., Rader, C.M., and Welch, P.D., 1967, "What Is the Fast Fourier Transform?" *Proceedings of the IEEE*, Vol. 55, No. 10, pp. 1664-1674.

APPENDIX A - THE HEAT AND MASS ANALOGY

The naphthalene sublimation method is based on the heat and mass analogy. This relationship permits heat transfer data to be determined from experimental measurements of mass transfer.

A.1 Derivation of Heat and Mass Analogy

Several assumptions must be valid to invoke the heat and mass analogy. Since the fluid involved is low velocity air, viscous dissipation can be assumed negligible. The solutal Grashof number, based on the height of the portion of a test fin coated with naphthalene, is approximately 15500 while the minimum Reynolds number based on the same length scale is about 1800. Since the Grashof number is much less than the square of the Reynolds number, buoyancy is negligible in comparison to inertial and pressure forces. Since temperature variations are small, thermophysical properties are approximately constant. Finally, the fluid is a dilute solution of species B in species A. With these assumptions, the equations for steady incompressible flow for the conservation of mass, linear momentum, energy, and species, respectively, can be written as shown below. The equations are written in tensor notation using Einstein's summation notation. In this notation, i and j represent either *1* or *2* where x_1 is the streamwise coordinate and x_2 is the normal coordinate. The flow is assumed two-dimensional in this analysis.

$$\frac{\partial u_i}{\partial x_i} = 0 \qquad \text{[A.1]}$$

$$u_j \frac{\partial u_i}{\partial x_j} = -\frac{1}{\rho}\frac{\partial P}{\partial x_i} + \nu \frac{\partial^2 u_i}{\partial x_j \partial x_j} \qquad \text{[A.2]}$$

$$u_j \frac{\partial T}{\partial x_j} = \alpha \frac{\partial^2 T}{\partial x_j \partial x_j} \qquad \text{[A.3]}$$

$$u_j \frac{\partial C_A}{\partial x_j} = D_{AB} \frac{\partial^2 C_A}{\partial x_j \partial x_j} \qquad \text{[A.4]}$$

The following boundary conditions apply:

$$\begin{aligned} &u_i(x_2 = 0) = 0 \\ &\lim_{x_2 \to \infty} u_i = U_{i,\infty} \\ &u_i(x_1 = 0) = U_{i,\infty} \end{aligned} \qquad \text{[A.5]}$$

$$\begin{aligned} &T(x_2 = 0) = T_w \\ &\lim_{x_2 \to \infty} T = T_\infty \\ &T(x_1 = 0) = T_\infty \end{aligned} \qquad \text{[A.6]}$$

$$\begin{aligned} &C_A(x_2 = 0) = C_{A,w} \\ &\lim_{x_2 \to \infty} C_A = C_{A,\infty} \\ &C_A(x_1 = 0) = C_{A,\infty} \end{aligned} \qquad \text{[A.7]}$$

Note the singularity at $x_1=x_2=0$. To simplify these equations and boundary conditions, the following dimensionless variables are used.

$$x_i^* = \frac{x_i}{L_{ref}}$$

$$u_i^* = \frac{u_i}{U_\infty}$$

$$P^* = \frac{P}{\rho U_\infty^{\,2}}$$

$$T^* = \frac{T - T_w}{T_\infty - T_w}$$

$$C_A{}^* = \frac{C_A - C_{A,w}}{C_{A,\infty} - C_{A,w}}$$

The resulting non-dimensional governing equations and boundary conditions are as follows:

$$\frac{\partial u_i^*}{\partial x_i^*} = 0 \qquad \text{[A.8]}$$

$$u_j^* \frac{\partial u_i^*}{\partial x_j^*} = -\frac{\partial P^*}{\partial x_i^*} + \frac{1}{\mathrm{Re}} \frac{\partial^2 u_i^*}{\partial x_j^* \partial x_j^*} \qquad [A.9]$$

$$u_j^* \frac{\partial T^*}{\partial x_j^*} = \frac{1}{\mathrm{Re\,Pr}} \frac{\partial^2 T^*}{\partial x_j^* \partial x_j^*} \qquad [A.10]$$

$$u_j^* \frac{\partial C_A^*}{\partial x_j^*} = \frac{1}{\mathrm{Re}\,Sc} \frac{\partial^2 C_A^*}{\partial x_j^* x_j^*} \qquad [A.11]$$

The resulting non-dimensional boundary conditions are

$$\begin{aligned} &u_i^*\left(x_2^* = 0\right) = 0 \\ &\lim_{x_2^* \to \infty} u_i^* = 1 \\ &u_i^*(x_1^* = 0) = 1 \end{aligned} \qquad [A.12]$$

$$\begin{aligned} &T^*\left(x_2^* = 0\right) = 0 \\ &\lim_{x_2^* \to \infty} T^* = 1 \\ &T^*(x_1^* = 0) = 1 \end{aligned} \qquad [A.13]$$

$$\begin{aligned} &C_A^*\left(x_2^* = 0\right) = 0 \\ &\lim_{x_2^* \to \infty} C_A^* = 1 \\ &C_A^*(x_1^* = 0) = 1 \end{aligned} \qquad [A.14]$$

For the heat and mass analogy to apply, the governing equations and all boundary conditions for the energy and species equations must have the same mathematical form. For this to be true, the normal component of velocity due to mass transfer from the fin must have a negligible impact on convection within the boundary layer. This assumption will be justified later.

The dimensionless equations and boundary conditions presented above satisfy these conditions. The continuity and momentum equations are decoupled from the energy and species equations, so the velocity components and the pressure gradient can be found with no information concerning temperature or species. Then these results can be substituted into the

energy and species equations. The energy and species equations are of the same form with the Prandtl and Schmidt numbers playing similar functions, as shown below.

$$T^* = f\left(x_i^*, \frac{dP^*}{dx_i^*}; Re, Pr \right) \qquad [A.15]$$

$$C_A{}^* = f\left(x_i^*, \frac{dP^*}{dx_i^*}; Re, Sc \right) \qquad [A.16]$$

The heat and mass transfer coefficients are defined below. They are based on temperature and species gradients between the wall (fin surface) and the free stream.

$$h = \frac{q''}{(T_w - T_\infty)} \qquad [A.17]$$

$$h_m = \frac{\dot{m}''}{(C_{A,w} - C_{A,\infty})} \qquad [A.18]$$

An energy balance at the fin surface is performed by setting the conductive heat flux equal to the convective heat flux. In the same way, the mass flux determined by Fick's law is equated to the convective mass transfer since non-Fickian mass transfer is negligible if the solution is dilute. From this energy balance, the following dimensionless parameters can be expressed:

$$Nu = \frac{hL_{ref}}{k} = \left. \frac{\partial T^*}{\partial x_2^*} \right|_{x_2^* = 0} = f(x_1^*; Re, Pr) \qquad [A.19]$$

$$Sh = \frac{h_m L_{ref}}{D_{AB}} = \left. \frac{\partial C_A{}^*}{\partial x_2^*} \right|_{x_2^* = 0} = f(x_1^*; Re, Sc) \qquad [A.20]$$

The Sherwood and Nusselt numbers are of similar form with Sc and Pr taking analogous roles. Since Sh and Nu are expected to be proportional to powers of Sc and Pr, [A.19] and [A.20] can be rewritten as

$$Nu = f(x_1^*; Re) Pr^n \qquad [A.21]$$

$$Sh = f(x_1^*; Re) Sc^n \qquad [A.22]$$

If equation [A.21] is divided by equation [A.22], the relationship between heat and mass transfer is obtained.

$$Nu = Sh\left(\frac{Pr}{Sc}\right)^{n} \qquad [A.23]$$

The form for average Sherwood and Nusselt numbers is the same.

$$\overline{Nu} = \overline{Sh}\left(\frac{Pr}{Sc}\right)^{n} \qquad [A.24]$$

A value for n of 1/3 is conventional. However, Sparrow and Hajiloo [12] suggested that a value of 0.4 for intermediate values of the Schmidt number is more accurate, and that value has been adopted for this study.

A.2 Justification of Zero Transverse Velocity Assumption

The heat and mass analogy is valid only if the transverse velocity due to mass transfer has a negligible impact on convection within the boundary layer. When mass transfer occurs there are two mechanisms contributing to the transverse velocity: viscous effects and mass transfer effects. Thus, if the mass-transfer contribution to the transverse velocity is negligible, the heat and mass analogy holds. The transverse velocity due to viscous effects, v_b, is represented by the well-known Blasius solution:

$$v_b = \frac{1}{2}\left(\frac{\nu U_\infty}{x}\right)^{1/2}(\eta f' - f) \qquad [A.25]$$

Within the boundary layer, η, f and f' are of order unity; therefore the transverse velocity due to viscous effects is given by

$$v_b \sim U_\infty (Re_x)^{-1/2} = Re^{1/2}\frac{\nu}{x} \qquad [A.26]$$

The transverse velocity due to mass transfer can be determined from the mass flux at the surface, which is given by the Blasius mass transfer solution:

$$Sh = 0.332 Re_x^{1/2} Sc^{1/3} = \frac{h_{m,x} x}{D_{AB}} \qquad 0.6<Sc<50 \qquad [A.27]$$

When this equation is combined with [A.18], the expression takes the form

$$\dot{m}'' = 0.332 \left(C_{A,w} - C_{A,\infty}\right) \frac{D_{AB}}{x} Re^{1/2} Sc^{1/3} \qquad [A.28]$$

For the heat and mass analogy to be valid, the following condition must be met:

$$\rho v_b >> \dot{m}'' \qquad [A.29]$$

Substituting the equations [A.26] and [A.28] into [A.29] yields the following inequality:

$$\frac{C_{A,w} - C_{A,\infty}}{\rho} << Sc^{2/3} \qquad [A.30]$$

For typical laboratory conditions, the left-hand side of [A.30] takes on a value of approximately $3.6(10^{-4})$, and the right-hand side is roughly 1.8. Therefore, use of the heat and mass analogy is justified. The reader is directed to [39] for further discussion of the zero transverse velocity assumption.

APPENDIX B - DATA REDUCTION EQUATIONS

The data in this experiment are reported in terms of six parameters -- Re, $\overline{Sh}$, j, f, PP, and Sh. This appendix includes a description of the correlations for thermophysical properties and equations used to reduce the data.

B.1 Reynolds Number

The Reynolds number, unless otherwise noted, is defined in terms of hydraulic diameter as shown.

$$Re = \frac{U_c d_h}{\nu} \qquad [B.1]$$

The hydraulic diameter d_h is defined following Kays and London [40] to be

$$d_h = 4\frac{A_c}{A} L_{core} \qquad [B.2]$$

Kays and London [40] also provided the following correlation for the kinematic viscosity of air:

$$\nu = \frac{1.805\times10^{-5} + 4.8\cdot10^{-8}(T-290)}{\rho_a} \qquad [B.3]$$

Here T is the temperature in Kelvin. The mass flow rate of air is determined by measuring the pressure drop across an ASME standard orifice plate. The air velocity is then determined from the mass flow rate. The mass flow rate is calculated via the following formula:

$$\dot{m} = \frac{\pi}{4} D^2 C \varepsilon \sqrt{\frac{2\Delta P \rho_a}{1-\beta^4}} \qquad [B.4]$$

where ΔP is the pressure drop across orifice plate. The discharge coefficient is a function of the diameter ratio β and the Reynolds number based on pipe diameter and is calculated per the ASME standard [33] using the following formula:

$$C = 0.5959 + 0.0312\beta^{2.1} - 0.184\beta^8 + 0.039\frac{\beta^4}{(1-\beta)} - 0.01584\beta^3 + 91.71\beta^{2.5}\,Re^{-0.75} \qquad [B.5]$$

Once the air mass flow rate is known, mass conservation can be used to find the velocity at the minimum free-flow area, U_C.

$$U_c = \frac{\dot{m}}{\rho_a A_c} \qquad [B.6]$$

For the flow visualization experiments, a water tunnel was used instead of a wind tunnel. For the water tunnel, U_C was determined by injecting ink into the water and timing the transit time over a known distance.

B.2 Mass Averaged Sherwood Number

The mass averaged Sherwood number is defined as

$$\overline{Sh} = \frac{d_h \overline{h_m}}{D_{na}} \qquad [B.7]$$

where

$$\bar{h}_m = \frac{\Delta m}{A_f \rho_{n,v} \Delta t} \qquad [B.8]$$

Here Δm is the total mass change and Δt the exposure time. To determine the density of saturated naphthalene vapor, the ideal gas law is used.

$$\rho_{n,v} = \frac{P_n M_n}{R_u T} \qquad [B.9]$$

The temperature, T, is the naphthalene vapor temperature at the surface of the fin, which is assumed to be the same as the air temperature. According to the analysis of Mendes [41], the phase change causes the fin surface temperature to decrease less than 0.02 °C below the air temperature. This temperature difference was neglected since it is within the uncertainty of the air temperature measurement. The correlation of Ambrose, Lawrenson, and Sprake [42], shown below, is used to determine the vapor pressure of naphthalene.

$$T \log_{10} P_n = \frac{a_o}{2} + \sum_{s=1}^{3} a_s E_s(x) \qquad [B.10]$$

Here $E_S(x)$ is the Chebyshev polynomial in x of degree s, where x is defined by

$$x = \left\{ \frac{2T - (T_{max} - T_{min})}{(T_{max} - T_{min})} \right\} \qquad [B.11]$$

In this equation, T_{max} = 344 K, and T_{min} = 230 K. The constants in the vapor pressure correlation are a_0 = 301.6247, a_1 = 791.4937, a_2 = -8.2536, a_3 = 0.4043. The mass diffusivity of naphthalene in air is found using the correlation developed by Cho, Irvine, and Karni [43].

$$D_{na} = 8.17708 \cdot 10^{-11} T^{1.983} \left(\frac{P_o}{P_{corr}} \right) \qquad [B.12]$$

P_O is standard atmospheric pressure, and P_{corr} is the barometric pressure corrected for temperature and the local acceleration due to gravity. These correction factors, which are shown below, are provided by the manufacturer of the barometer.

$$P_{corr} = P + P_{tcf} + P_{gcf} \qquad [B.13]$$

$$P_{tcf} = P \left[\frac{1 - 1.84 \cdot 10^{-5} (T - 273.15)}{1 + 1.818 \cdot 10^{-4} (T - 273.15)} - 1 \right] \qquad [B.14]$$

$$P_{gcf} = -4.1684 \cdot 10^{-4} \left(P + P_{tcf} \right) \qquad [B.15]$$

B.3 Modified Colburn j Factor

Heat and mass transfer are often given in terms of the Colburn j factor. The mass transfer Colburn j factor is

$$j = \frac{\overline{Sh}}{\mathrm{Re}\, Sc^n} \qquad [B.16]$$

Although a value for n of 1/3 is conventional, Sparrow and Hajiloo [12] suggest a value of 0.4 for intermediate values of the Schmidt number, as is the case here (Sc ≈ 2.35). This modified Colburn j factor is adopted for this study. The Schmidt number is determined using the

correlation of Cho, Irvine, and Karni [43], shown below. The temperature in this case is the fin surface temperature.

$$Sc = 8.0743T^{-0.2165} \qquad \text{[B.17]}$$

Since heat and mass transfer are analogous, the mass transfer Colburn j factor and the heat transfer Colburn j factor, $j = \overline{Nu} / \mathrm{Re}\,\mathrm{Pr}^{n}$, are equal.

B.4 Friction Factor

Pressure drop data are represented using the Fanning friction factor, which is defined here as

$$f = \frac{2\Delta P}{\rho U_c^2}\left(\frac{d_h}{4L_{core}}\right) \qquad \text{[B.18]}$$

where ΔP is the pressure drop across the core.

B.5 Pumping Power

The pressure drop data are alternately represented using pumping power, defined as

$$PP = U_c A_c \Delta P \qquad \text{[B.19]}$$

B.6 Local Sherwood Number

The local Sherwood number for a given position on a fin is

$$Sh = \frac{h_m d_h}{D_{na}} \qquad \text{[B.20]}$$

The local mass transfer coefficient is determined via [B.21]

$$h_m = \frac{\rho_{n,s}\delta_{sb}}{\rho_{n,v}\Delta t} \qquad \text{[B.21]}$$

The density of solid naphthalene is given by Kudchadker, Kudchadker, and Wilhoit [44] to be $\rho_{n,S} = 1162.0\ \mathrm{kg/m^3}$ [44].

APPENDIX C - CALIBRATION PROCEDURE

C.1 RTD Calibration

Both RTDs used in this experiment were carefully calibrated to ensure that the errors in the Reynolds number and naphthalene vapor pressure were small. The instruments were re-calibrated approximately every three months to ensure that the temperature readings remained accurate. The calibration was performed using a NesLab isothermal bath and NIST traceable calibrated, ASTM certified, mercury-in-glass thermometers with 0.01 °C divisions. Since these thermometers were total immersion thermometers, the temperature readings were corrected to account for the section of the thermometer that was exposed to the air.

The RTDs were calibrated in one degree intervals over a range of 17 to 25 °C. In order to correct for the exposed portion of the thermometer, a type-T thermocouple was attached to the thermometer at the midpoint of the exposed section. The temperature of the stem was acquired using an Omega handheld thermocouple reader. The RTDs were connected to a Strawberry Tree T55-020 terminal panel for RTD inputs which was connected to an ACM2-12-16 Strawberry Tree 12-bit data acquisition board. With a range of -5 to +50 mV, the board's full scale resolution was 12 μV with an absolute accuracy of 0.08% of the range.

For each step, the temperature bath was allowed approximately 30 minutes to come to equilibrium. To ensure that the bath had reached equilibrium, the voltage readings were averaged over two minutes and compared to make sure they matched the instantaneous reading within 2 μV. The voltage reading, thermometer reading, and thermocouple reading were recorded for each RTD for each step. To account for conduction along the stem of the thermometer, the following stem correction factor was computed and added to the thermometer temperature:

$$SCF = 0.00016(T - ST)N \qquad [C.1]$$

Here T is the bath temperature in degrees Celsius, ST is the average stem temperature, and N is the number of degrees on the thermometer which are exposed to the ambient.

The calibration curves are shown in Figures C.1 and C.2. Both curves proved to be very linear. The least-squared linear fits had simple coefficients of correlation of r^2=0.99998 and r^2=0.99997, respectively. This calibration resulted in a temperature measurement uncertainty of approximately ± 0.1°C (0.18 °F). An uncertainty analysis is presented in Appendix D.

C.2 Pressure Transmitter Calibration

A Modus Instruments model T10 differential pressure transmitter with a range of 0-24.9 Pa (0-0.1 in water) was used to measure the pressure drop across the core. The transmitter was calibrated using the Dwyer Microtector. There proved to be a quadratic relationship between the output voltage and the pressure drop, as shown in Fig. C.3. The maximum deviation between the curve and the measured values is 0.37 Pa (0.0015 in water).

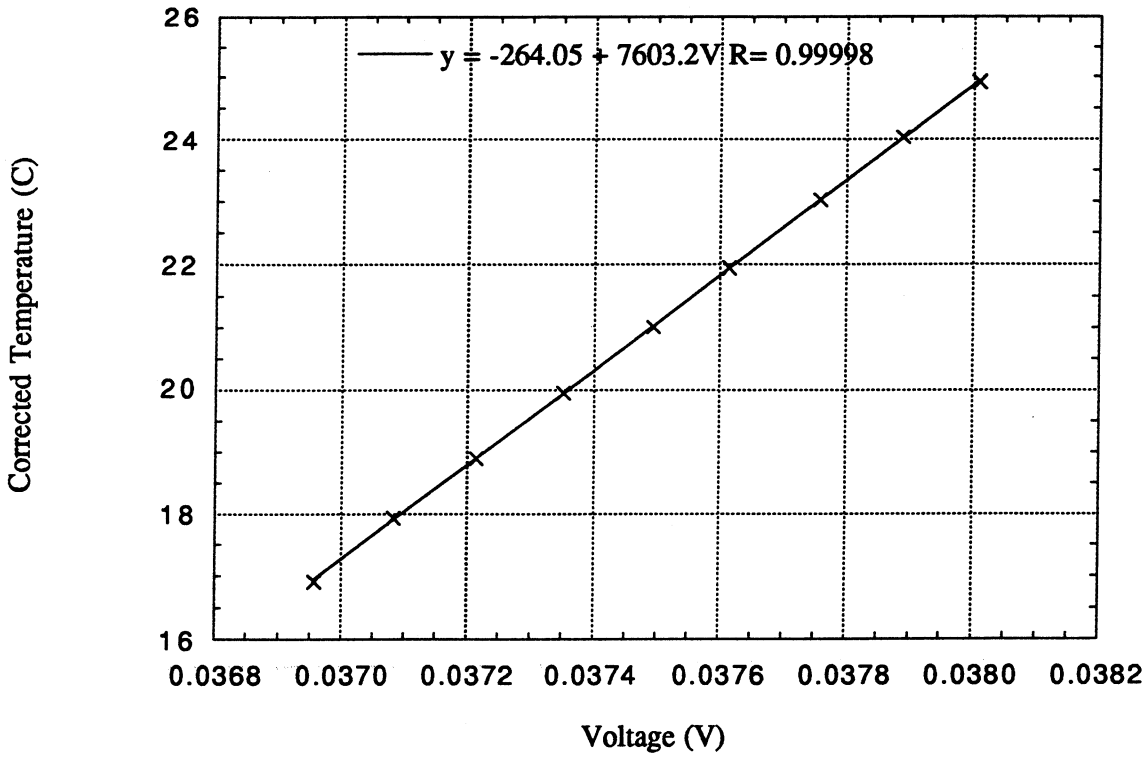

Fig. C.1 - Calibration curve for upstream RTD

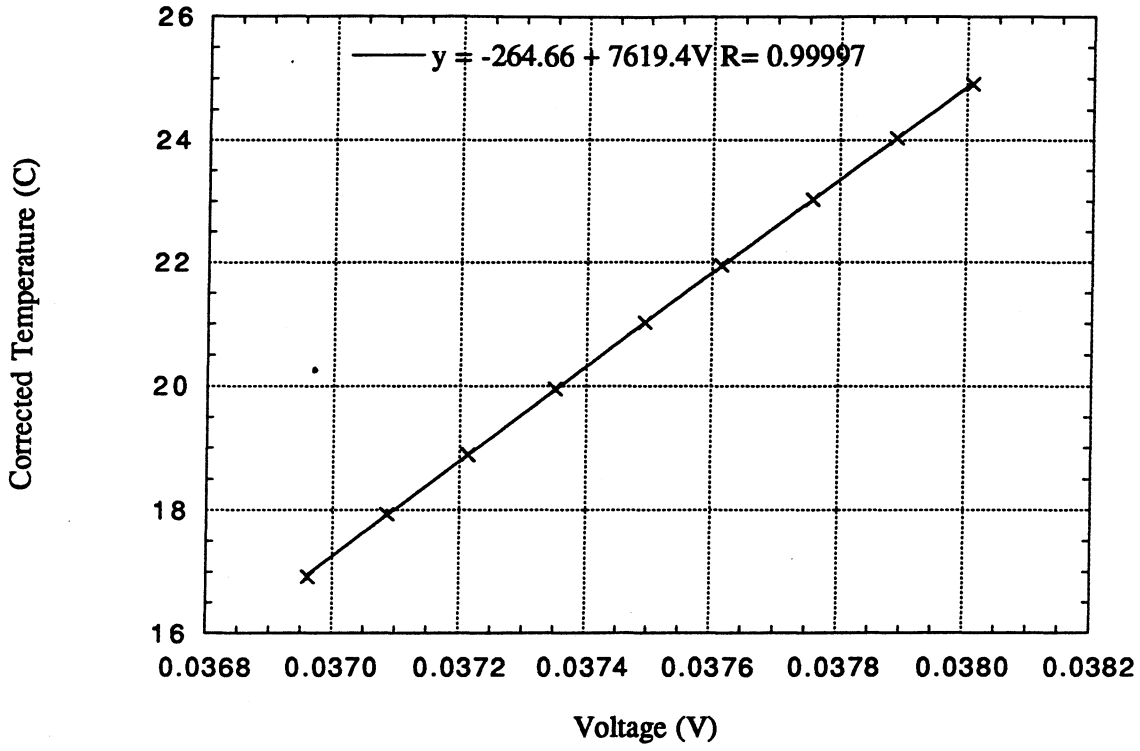

Fig. C.2 - Calibration curve for downstream RTD

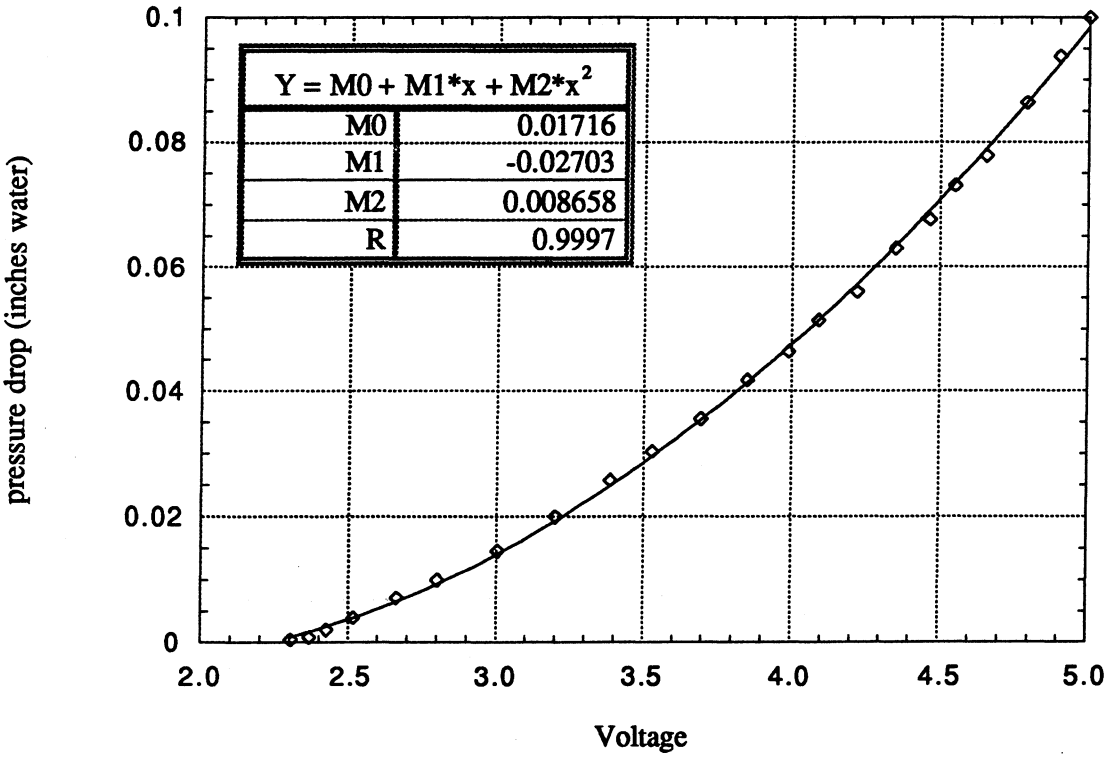

Fig. C.3 - Calibration curve for differential pressure transmitter

APPENDIX D - UNCERTAINTY ANALYSIS

D.1 Errors in Experimental Data

All of the results presented are based on eight laboratory measurements and thermophysical properties. The measurements included test section temperatures, pressure drop across the core and orifice plate, test fin mass change, barometric pressure, relative humidity, exposure time, and naphthalene sublimation depths. To determine the uncertainties in the results, the propagation of the measurement uncertainties through the data reduction scheme must be performed

Both bias (fixed) and precision (random) errors were included in the temperature measurement error. The bias error included errors due to the finite resolution of the A/D card, the use of a curve fit to the RTD calibration data, the reading of the calibration thermometers, and conduction and radiation errors. The precision error included contributions due to fluctuations in the electronics of the data acquisition system. The errors due to the A/D card resolution and the use of a curve fit were determined by plotting the difference between the corrected calibration temperatures and the temperatures calculated using the curve fits, as shown in Fig. D.1.

The contribution to bias error due to conduction was determined by modeling the RTD as a straight pin fin. The conduction error in this case is the difference between the air temperature and the fin tip temperature. An adiabatic tip, an isothermal base, steady state conditions, and 1-D conduction were assumed. The average heat transfer coefficient was determined from the following correlation for flow over a cylinder given by Whitaker in Holman [45]:

$$Nu = \frac{\bar{h}d}{k} = (0.4\,\mathrm{Re}^{0.5} + 0.06\,\mathrm{Re}^{2/3})\,\mathrm{Pr}^{0.4}\left(\frac{\mu_\infty}{\mu_w}\right)^{0.25} \qquad [D.1]$$

Using a worst case scenario with a Reynolds number based on RTD diameter of 83, the conduction error was calculated to be very nearly zero and was therefore neglected. Similarly,

since the laboratory temperature was within 0.5 °C (0.9 °F) of the RTD temperature, the radiation error was also assumed negligible.

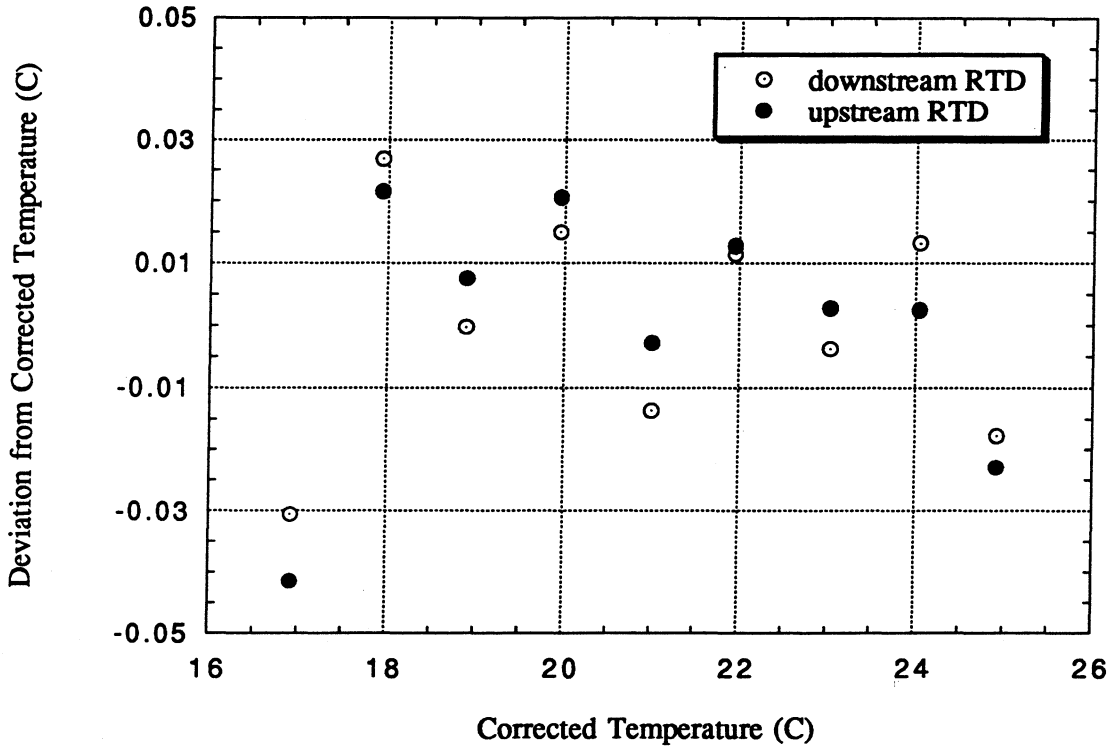

Fig. D.1 - Deviation of RTD curve fit from corrected ASTM calibration thermometer readings

The magnitude of the random error was defined using a 95% confidence interval for the temperature readings at a given temperature. This value was determined by setting the isothermal bath at the most common RTD temperature. Thirty-five temperature points were taken at this temperature, and the average and standard deviation were calculated using the following formulas:

$$\overline{T} = \frac{1}{N}\sum_{i=1}^{N} T_i \qquad [D.2]$$

$$S_T = \left[\frac{1}{N-1}\sum_{i=1}^{N}\left(T_i - \overline{T}\right)^2\right]^{\frac{1}{2}} \qquad [D.3]$$

For this case, the 95% confidence interval is given by two sample standard deviations. The random error calculated using this analysis was 0.02°C (0.036 °F). The RMS of the bias and precision error led to a combined error of ±0.055 ° C (±0.1 °F). In order to incorporate a margin of safety to allow for a small amount of electronic fluctuations over time, a value of ±0.1° C (±0.18 °F) was used in calculating the accuracy of the data.

Using a similar analysis, the uncertainty of the pressure drop calculated using the pressure transmitter was determined. This uncertainty was computed to be 0.37 Pa (±0.0015 in water).

Except for the micromanometer, which served as a calibration standard, each of the other instruments was calibrated at the factory. Errors were determined by either the manufacturer's published accuracy or one half the smallest scale division. For the micromanometer, this value was ±0.25 Pa (±0.001 in water), while for the barometer it was ±13 Pa (±0.054 in water). The error of the precision balance was +/-0.00005 g, and the accuracy of the relative humidity meter was ±2%. The manufacturer's published accuracy for laser profilometer was 4 μm (1.6×10^{-4} in). However, repeated scans of a metal block led to an estimated error in δ_{sb} of ±6 μm ($\pm 2.4 \times 10^{-4}$ in).

D.2 Error Propagation and Uncertainty

The uncertainties of the reduced data were determined by propagating these errors using the method of Kline and McClintock [46]. The reduced data were presented in the form of Re, $\overline{Sh}$, j, f, and Sh.

The uncertainty in Reynolds number is given by the following formula:

$$\frac{W_{Re}}{Re} = \left[\left(\frac{W_{U_c}}{U_c} \right)^2 + \left(\frac{W_{d_h}}{d_h} \right)^2 + \left(\frac{W_\nu}{\nu} \right)^2 \right]^{1/2} \qquad [D.4]$$

The uncertainty in U_C was determined by propagating errors through the continuity equation, as shown by [D.5].

$$\frac{W_{U_c}}{U_c} = \left[\left(\frac{W_{\dot{m}}}{\dot{m}} \right)^2 + \left(\frac{W_{\rho_a}}{\rho_a} \right)^2 + \left(\frac{W_{A_c}}{A_c} \right)^2 \right]^{1/2} \qquad [D.5]$$

The uncertainty in mass flow rate was determined through the use of the following formula:

$$W_{\dot{m}} = \left[\left(W_D \cdot \frac{\partial \dot{m}}{\partial D} \right)^2 + \left(W_C \cdot \frac{\partial \dot{m}}{\partial C} \right)^2 + \left(W_\varepsilon \cdot \frac{\partial \dot{m}}{\partial \varepsilon} \right)^2 + \left(W_\beta \cdot \frac{\partial \dot{m}}{\partial \beta} \right)^2 + \left(W_{\Delta P} \cdot \frac{\partial \dot{m}}{\partial \Delta P} \right)^2 + \left(W_\rho \cdot \frac{\partial \dot{m}}{\partial \rho} \right)^2 \right]^{1/2} \qquad [D.6]$$

The ASME standard [40] gives the uncertainty for the discharge coefficient, C, as a function of Reynolds number and orifice plate geometry. For these experiments, the uncertainty ranged from 0.6% to 1.35%. For the uncertainty analysis, 1.35% was used. The uncertainty in ß was approximately 1.4% and in D was 0.7%. The uncertainty in ΔP, 0.5%, was determined from the smallest division of the manometer. Since ρ was corrected for temperature changes, the error in ρ was taken to be 0.5%. The expansion coefficient, ε, was 1 within 0.1%. Propagating these errors through the three equations gave an error in Re of 2%.

The uncertainty in $\overline{Sh}$ was calculated using the following formula:

$$\frac{W_{\overline{Sh}}}{\overline{Sh}} = \left[\left(\frac{W_{\Delta m}}{\Delta m} \right)^2 + \left(\frac{W_T}{T} \right)^2 + \left(\frac{W_{P_{wv}}}{P_{wv}} \right)^2 + \left(\frac{W_{D_{wa}}}{D_{wa}} \right)^2 + \left(\frac{W_{\Delta t}}{\Delta t} \right)^2 \right]^{1/2} \qquad [D.7]$$

The uncertainty in one mass measurement is ±1/2 of the smallest scale division (0.00005 g). This value was doubled to account for the possible presence of dust or other small errors. The error in temperature, as discussed above, was 0.1°C (0.18 °F), and the error in Δt was assumed to be 1 s. The published uncertainties in the naphthalene vapor pressure and mass diffusivity are both approximately 3%. The uncertainties in the both the vapor pressure and mass diffusivity due the uncertainty in the temperature were negligible compared to the uncertainties in the correlations themselves. These values result in an uncertainty in $\overline{Sh}$ of 5%.

The uncertainty in the Colburn j factor was determined using the following:

$$\frac{W_j}{j} = \left[\left(\frac{W_{Sh}}{Sh} \right)^2 + \left(\frac{W_{Re}}{Re} \right)^2 + \left(\frac{0.4 W_{Sc}}{Sc} \right)^2 \right]^{1/2} \qquad [D.8]$$

The Schmidt number was assumed to have approximately the same uncertainty as the diffusion coefficient data in [x] from which it was calculated, which was ±3%. The resulting uncertainty in j was 5.5%.

The formula to determine the uncertainty in the friction factor is as follows:

$$\frac{W_f}{f}=\left[\left(\frac{W_\rho}{\rho}\right)^2+\left(\frac{W_{\Delta P}}{\Delta P}\right)^2+\left(\frac{2W_{U_c}}{U_c}\right)^2\right]^{1/2} \qquad [D.9]$$

The uncertainties of the air density and U_C were 0.5% and 2% respectively. The uncertainty in ΔP decreased as the Reynolds number increased because the uncertainty of the pressure transmitter calibration was 0.37 Pa (+/-0.0015 in water). Therefore, the uncertainties in ΔP for flow through the dense offset strip geometry ranged from approximately 50% at very low Reynolds numbers to 0.2% at high Reynolds numbers. Above a Reynolds number of 1000, the average uncertainty in ΔP was 1%, leading to an average uncertainty in f of 4%. Flow through the less dense geometries incurred smaller pressure drops with correspondingly larger uncertainties. For example, the uncertainties in ΔP for flow through the in-line louvered geometry ranged from 100% at very low Reynolds numbers to 0.4 %. Above a Reynolds number of 1000, the average uncertainty in ΔP was 6%, leading to an average uncertainty in f of 7%.

If the density of solid naphthalene is assumed to be a constant, the expression for the uncertainty in the local Sherwood number is as follows:

$$\left(\frac{W_{Sh}}{Sh}\right)=\left[\left(\frac{W_{\delta_{sb}}}{\delta_{sb}}\right)^2+\left(\frac{W_T}{T}\right)^2+\left(\frac{W_{P_{nv}}}{P_{nv}}\right)^2+\left(\frac{W_{D_{na}}}{D_{na}}\right)^2\right]^{1/2} \qquad [D.10]$$

The uncertainty in sublimation depth depended on the magnitude of the sublimation depth. During a typical run, sublimation depths ranged from 25 μm up to 120 μm (0.001" to 0.005") with an average of approximately 60 μm (0.002 in). These values yielded an average uncertainty in Sherwood number of 11% with an uncertainty of 24% in regions of low mass transfer and 7% in regions of high mass transfer.

APPENDIX E - TEST SECTION FREQUENCY ANALYSIS

In an attempt to determine the cause of the anomalies discussed in Section 4.1.4, power spectra of the frequencies present in the test section under different conditions were determined through the use of Fast Fourier Transforms (FFTs). The equipment used to perform this analysis is discussed in Chapter 2. In this appendix, FFTs are discussed briefly before the results of the investigation are presented.

E.1 Description of Fast Fourier Transforms

Discrete Fourier Transforms (DFTs) have historically been used to analyze continuous waveforms via computer. The data are sampled to provide a time series of discrete points. The DFT of this discretely sampled waveform is similar to a Fourier transform of the continuous waveform. The DFT is used to analyze power spectra. The equation for the DFT is [47]

$$A_r = \sum_{k=0}^{N-1} (X_k) W^{rk} \qquad r = 0, ..., N - 1 \qquad [E.1]$$

where

$$W = \exp(-2\pi j/N) \qquad [E.2]$$

In this equation A_r is the rth coefficient of the DFT, X_k is the kth sample of the series, j is the imaginary number, and N is the number of samples. Its inverse is

$$X_l = (1/N) \sum_{r=0}^{N-1} A_r W^{-rl} \qquad l = 0, 1, ..., N - 1 \qquad [E.3]$$

The FFT is an algorithm that computes a DFT using less computational time and incurring smaller round-off errors. Larger and larger weighted sums of samples are combined to produce the coefficients shown in [E.1]. The different groups of DFTs which result are then combined, resulting in a DFT of the entire sample. For a complete derivation and discussion of the FFT, the reader is directed to [47].

E.2 Results of FFT analysis

Power spectra inside the test section for ten different operating conditions are shown in Figs. E.1-E.10. In the figure captions, "Orifice Plate 1" is the orifice plate with the smallest bore diameter (36.83 mm) while "Orifice Plate 2" is the plate with the 55.88 mm bore. The larger the bore diameter, the larger the Reynolds number for a given wind tunnel motor frequency. Fig. E.1 is the power spectrum of the background noise with the wind tunnel turned off. Figs. E.2-E.4 show that as the tunnel motor frequency increases, the peaks of the power spectra increase in magnitude and move to slightly higher frequencies. Figs. E.4 and E.5 show that the presence of flow straighteners downstream of the test section has little effect on the power spectra in spite of the fact that they have a profound effect on heat transfer, as discussed in Chapter 4. Figs. E.4, E.6, and E.7 show that the frequencies present in the test section are caused primarily by the tunnel motor frequency. When two different orifice plates are in line, the same motor frequency results in different flow velocities and hence different Reynolds numbers. However, the power spectra are the same. Also, similar Reynolds numbers produced using two different plates (and therefore requiring different motor frequencies) result in different power spectra. When Orifice Plate 2 is in place, both the required tunnel frequency and the power of the frequencies present in the tunnel are lower than when Orifice Plate 1 is present. The fan blade-passing frequency appears to have a small effect on the frequencies present in the tunnel. For the situations under which Figs. E.4 and E.8 were acquired, the fan blade passing frequency was 88 Hz. A small spike is visible in both of those graphs at that frequency. Fig. E.8 shows that when the orifice plate is removed, the peak present on the other graphs at about 10 Hz decreases in magnitude. Otherwise the spectra are not affected. Figs. E.9 and E.10 reveal that the both the fins and the contraction have no noticeable effect on the power spectra in the test section. In conclusion, the vortex shedding frequency is not evident in these plots. The vortex shedding frequency is overwhelmed by the effects of the tunnel motor frequency and therefore is not discernible using this method.

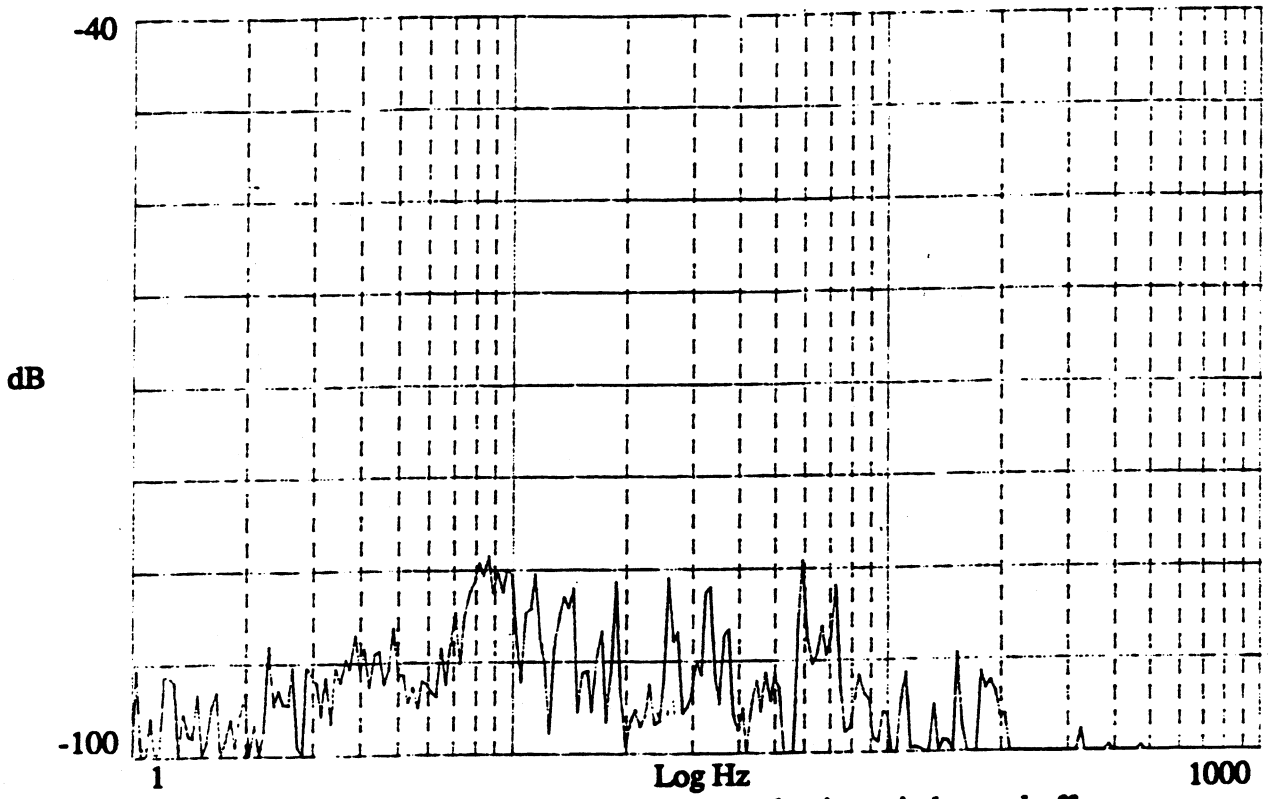

Fig. E.1 - Power spectrum of background noise; wind tunnel off

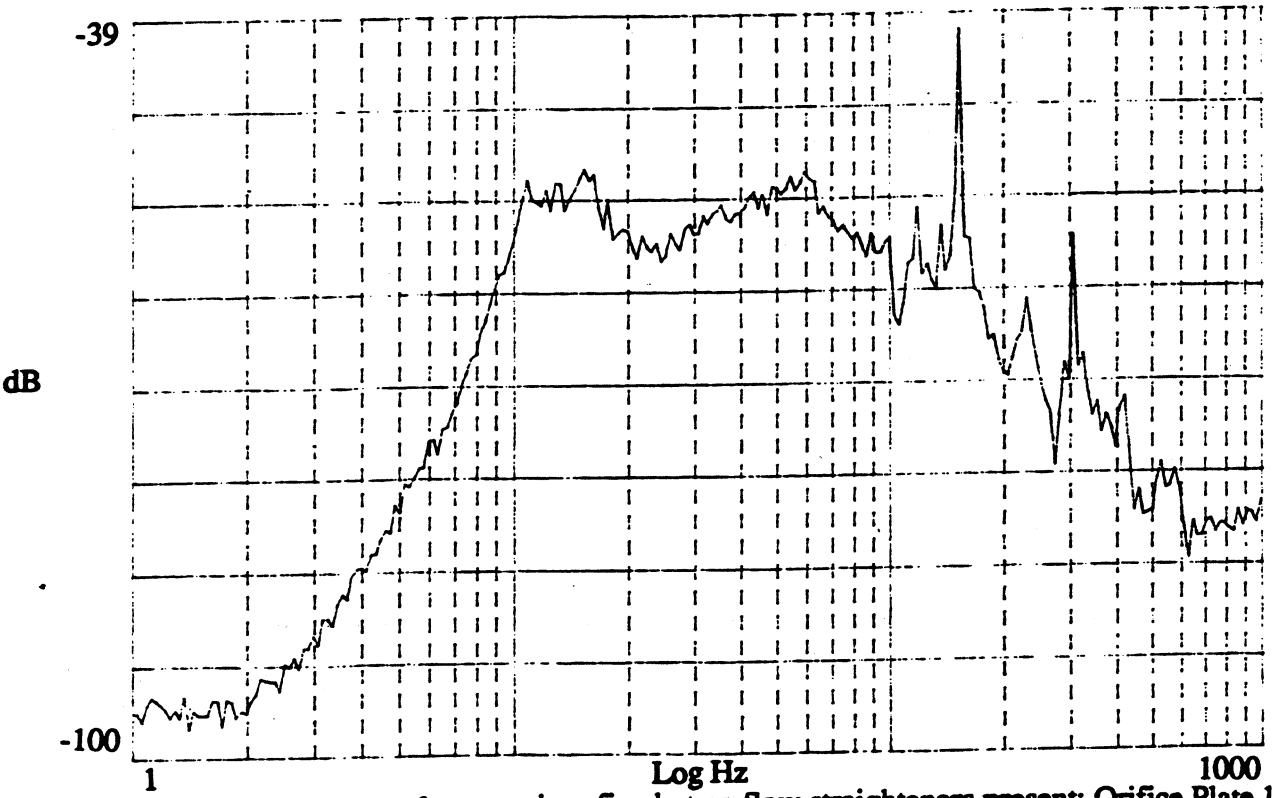

Fig. E.2 - Power spectrum of test section; fins but no flow straighteners present; Orifice Plate 1 in line; tunnel motor frequency = 32 Hz

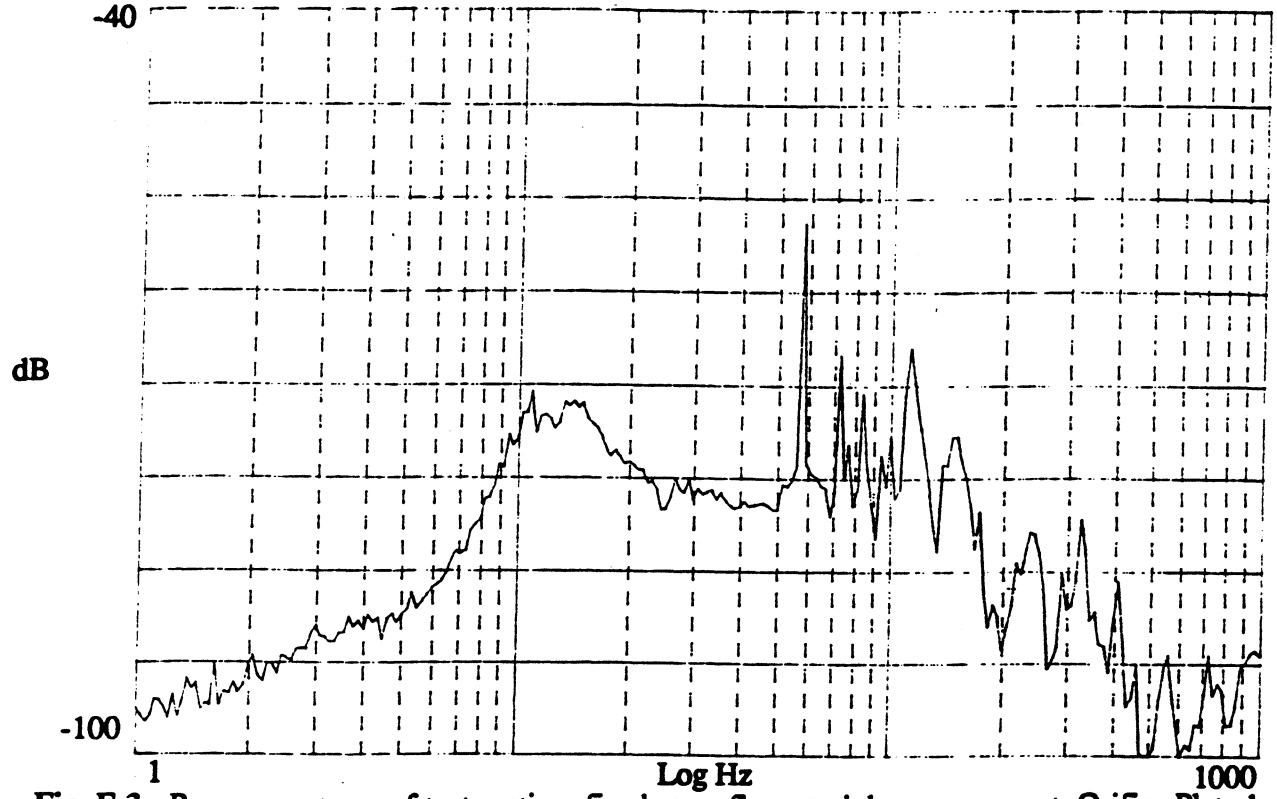

Fig. E.3 - Power spectrum of test section; fins but no flow straighteners present; Orifice Plate 1 in line; tunnel motor frequency = 12 Hz; Re ≈ 540

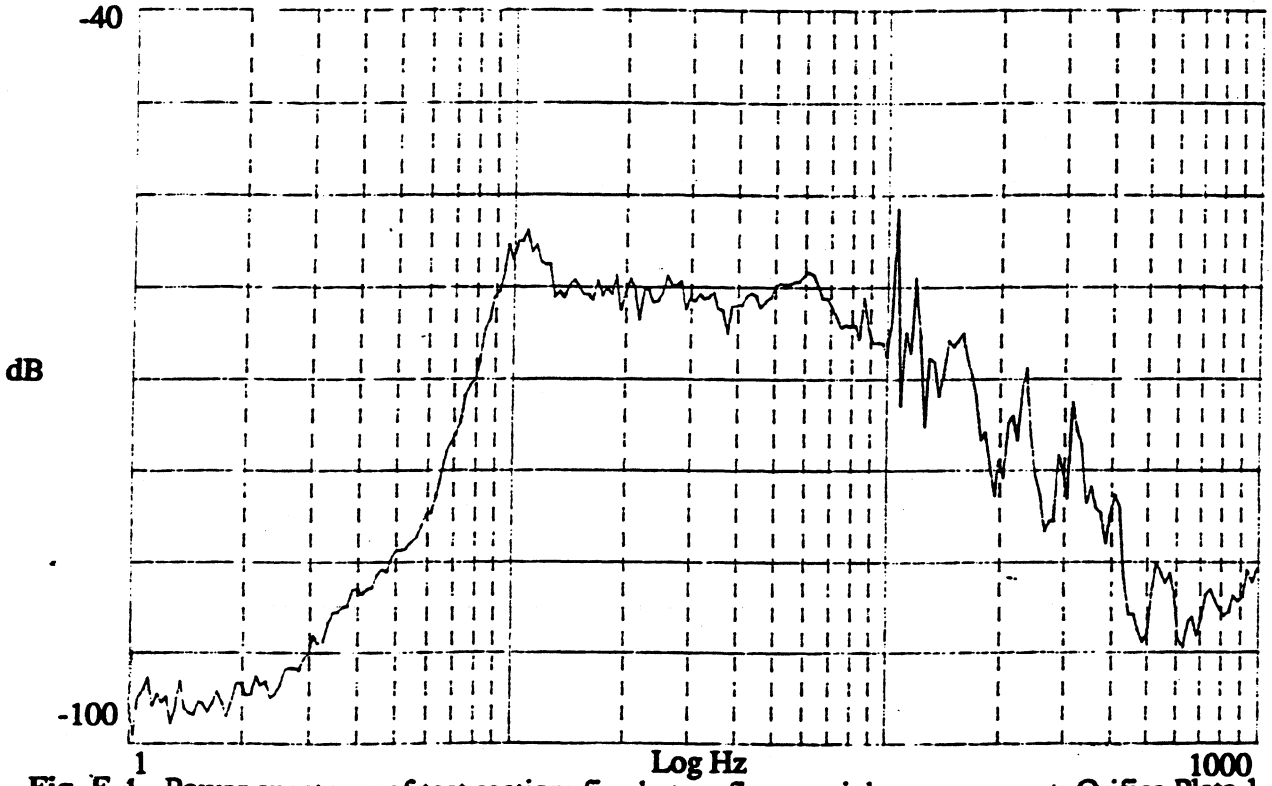

Fig. E.4 - Power spectrum of test section; fins but no flow straighteners present; Orifice Plate 1 in line; tunnel motor frequency = 22 Hz; Re ≈ 1000

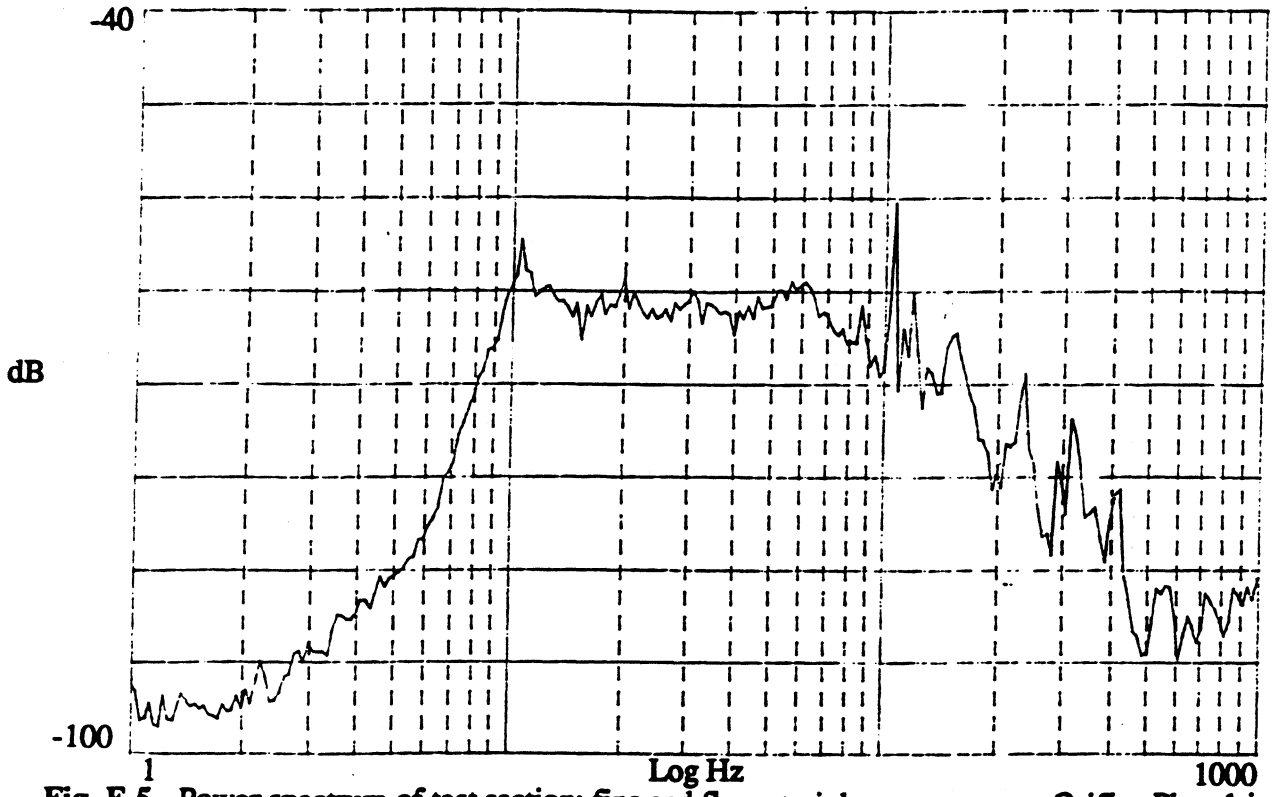

Fig. E.5 - Power spectrum of test section; fins and flow straighteners present; Orifice Plate 1 in line; tunnel motor frequency = 22 Hz; Re ≈ 1000

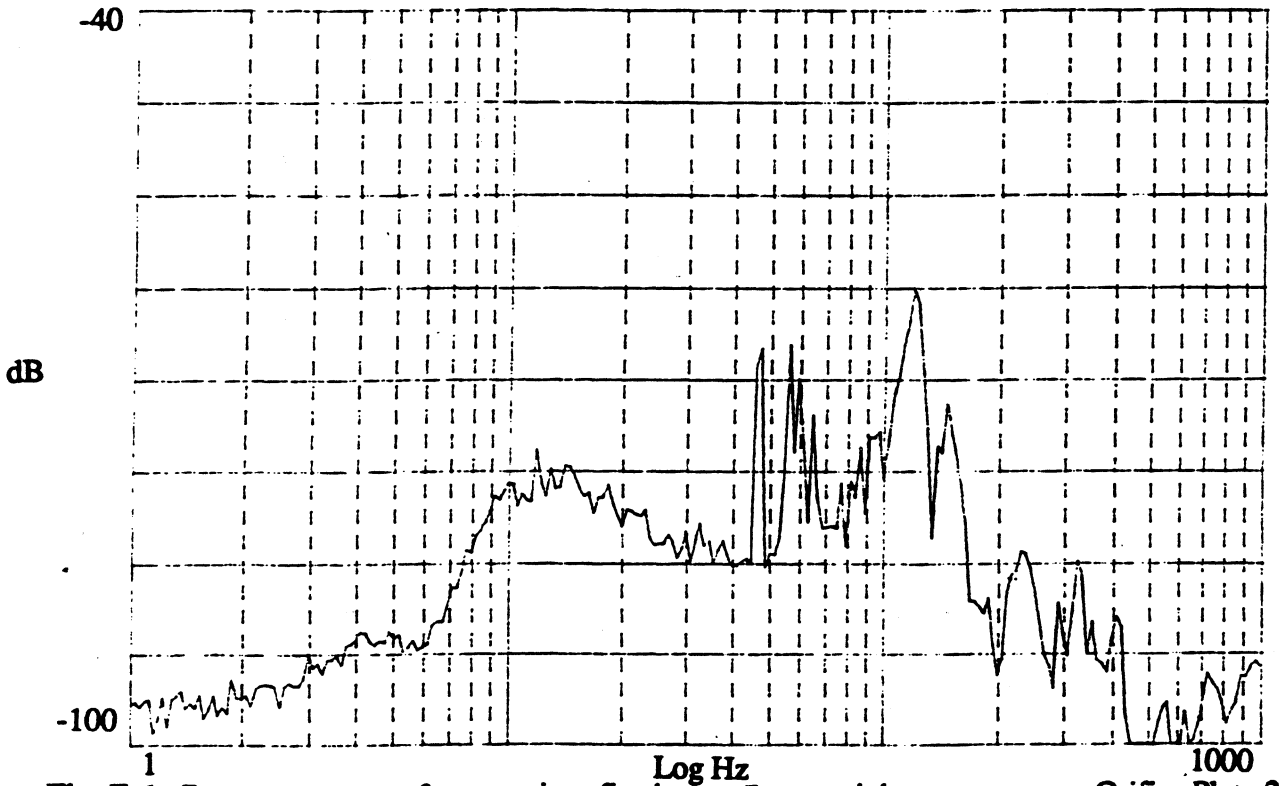

Fig. E.6 - Power spectrum of test section; fins but no flow straighteners present; Orifice Plate 2 in line; tunnel motor frequency = 9.8 Hz; Re ≈ 1400

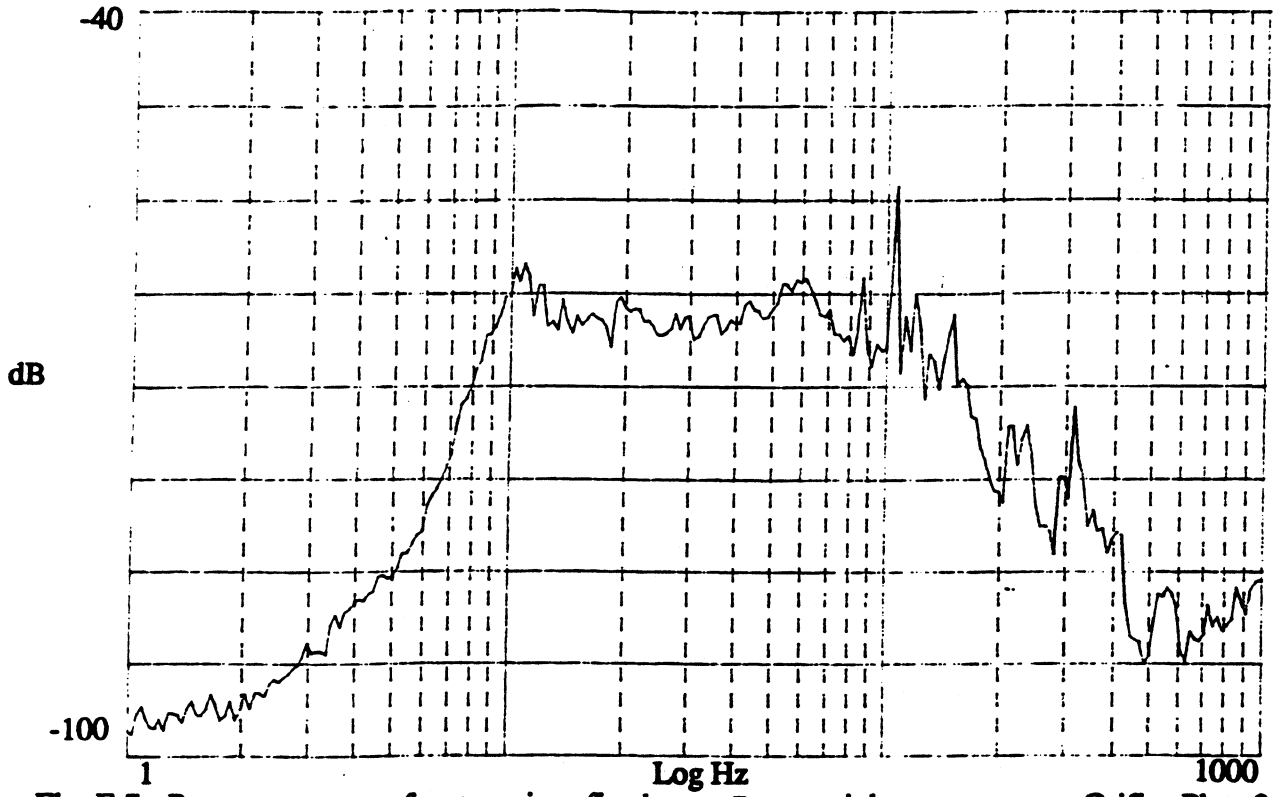

Fig. E.7 - Power spectrum of test section; fins but no flow straighteners present; Orifice Plate 2 in line; tunnel motor frequency = 22 Hz; Re = 2200

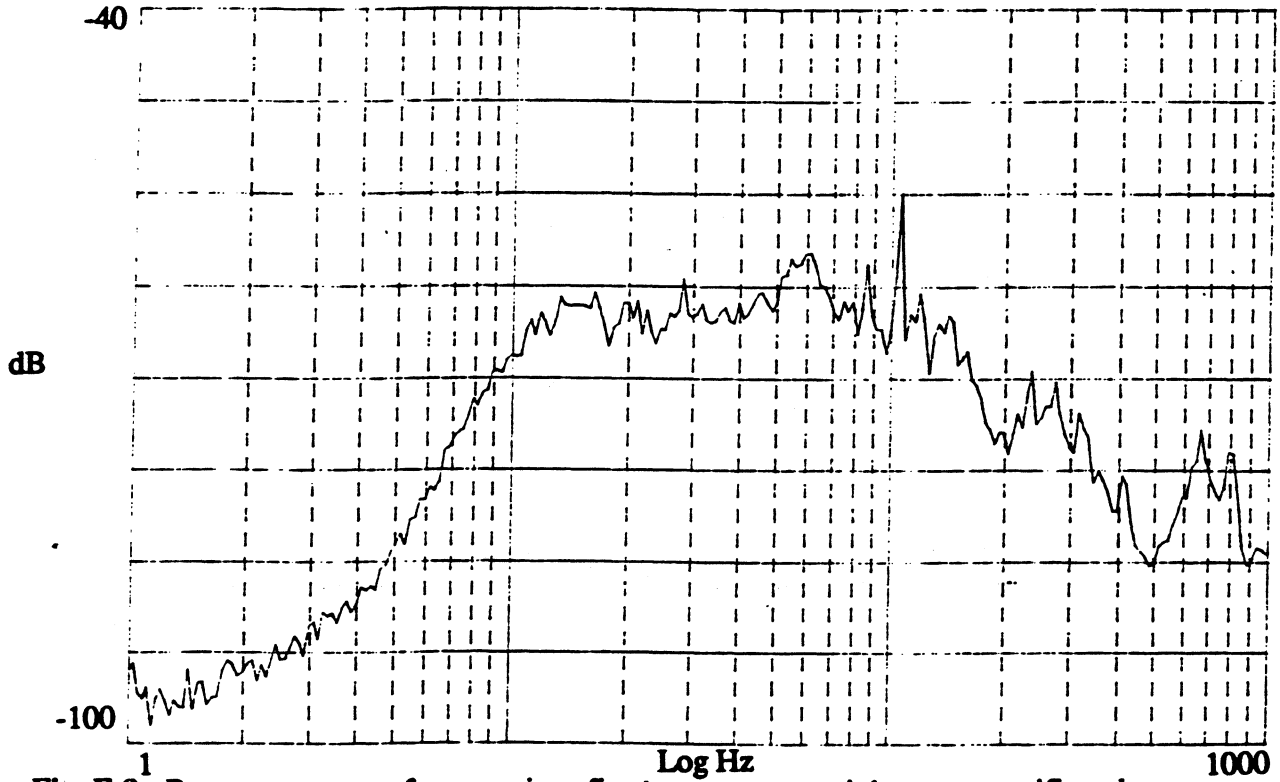

Fig. E.8 - Power spectrum of test section; fins but no flow straighteners or orifice plate present; tunnel motor frequency = 22 Hz; Re = 7100

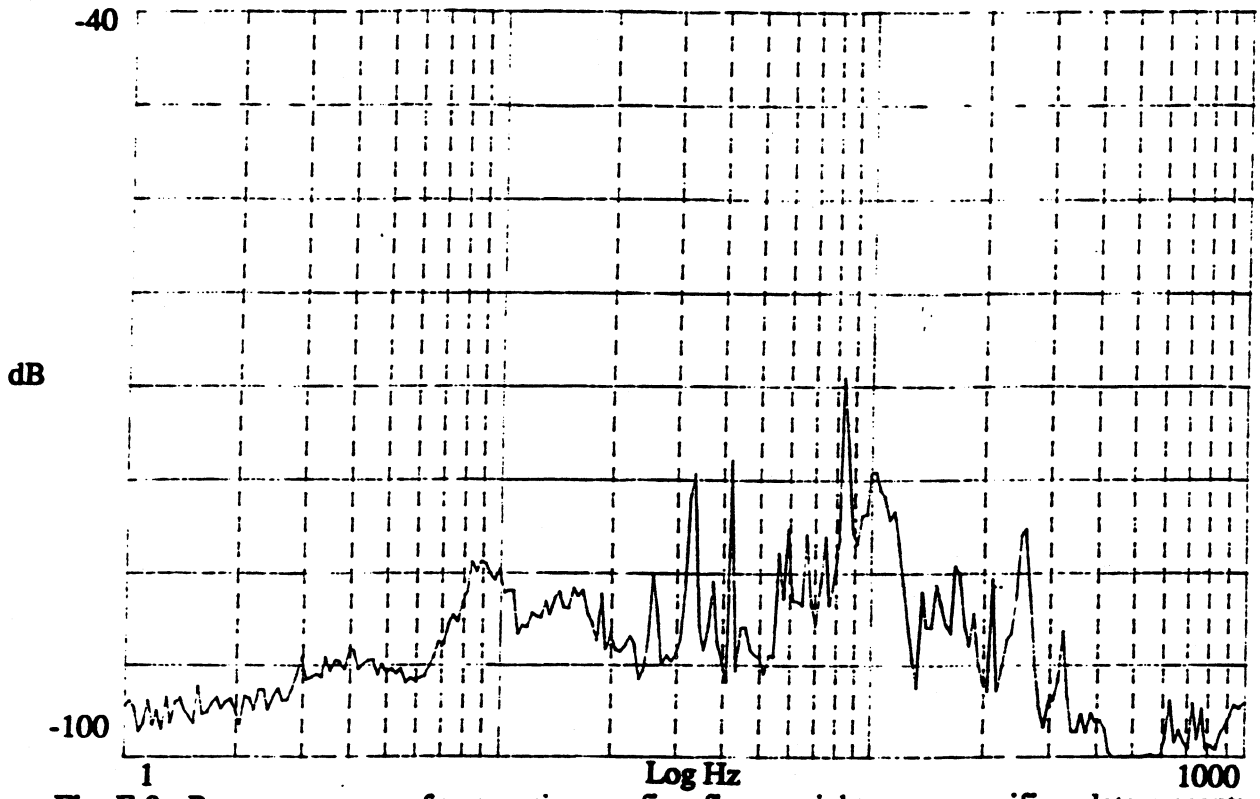

Fig. E.9 - Power spectrum of test section; no fins, flow straighteners, or orifice plate present; tunnel motor frequency = 7.1 Hz; Re ≈ 1400

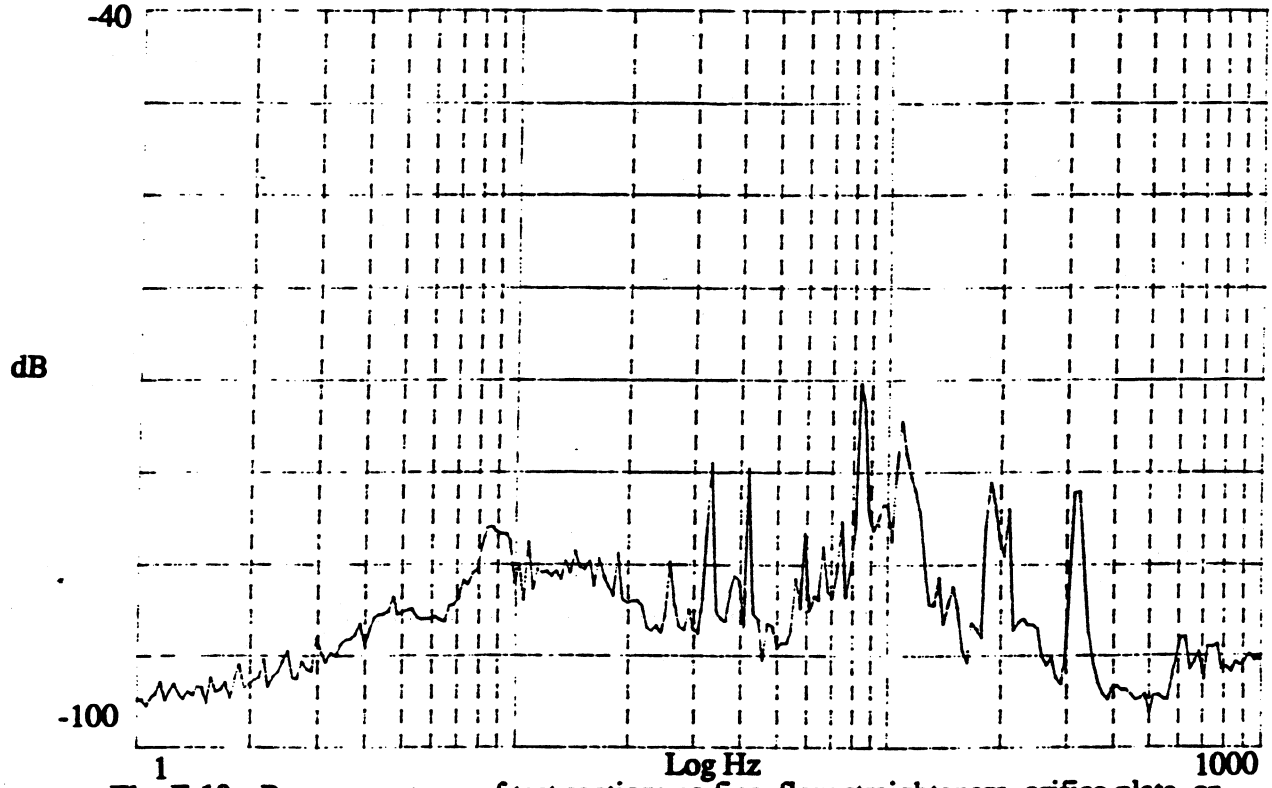

Fig. E.10 - Power spectrum of test section; no fins, flow straighteners, orifice plate, or contraction present; tunnel motor frequency = 7.1 Hz; Re ≈ 1000